Okinawa Institute of Science and Technology
Graduate University

Thesis submitted for the degree

Doctor of Philosophy

Flow Instabilities and Vortex Dynamics in Intersecting Flows

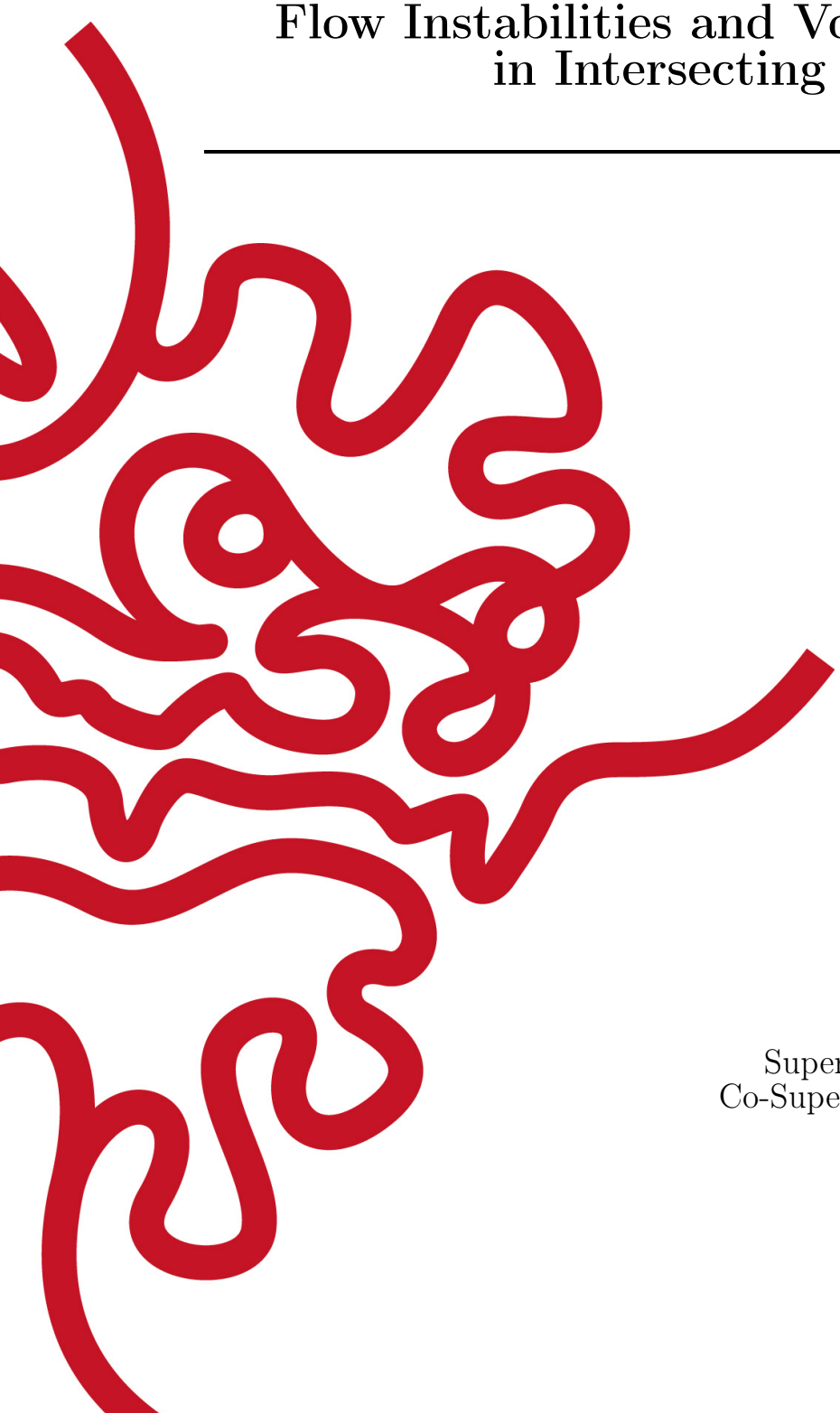

by

Noa Burshtein

Supervisor: **Prof. Amy Q. Shen**
Co-Supervisor: **Dr. Simon Haward**

April, 2020

Declaration of Original and Sole Authorship

I, Noa Burshtein, declare that this thesis entitled *Flow Instabilities and Vortex Dynamics at Intersecting Flows* and the data presented in it are original and my own work.

I confirm that:

- No part of this work has previously been submitted for a degree at this or any other university.
- References to the work of others have been clearly acknowledged. Quotations from the work of others have been clearly indicated, and attributed to them.
- In cases where others have contributed to part of this work, such contribution has been clearly acknowledged and distinguished from my own work.
- None of this work has been previously published elsewhere, with the exception of the following:

  1. Noa Burshtein, Amy Q. Shen, Simon J. Haward, "Controlled symmetry breaking and vortex dynamics in intersecting flows", Physics of Fluids, 31, 034104, 2019 [1].
  2. Noa Burshtein*, San To Chan*, Kazumi Toda-Peters, Amy Q. Shen, Simon J. Haward, "3D-printed glass microfluidics for fluid dynamics and rheology", Current Opinion in Colloid & Interface Science, v. 43, p. 1-14, 2018. *Equal contribution [2].
  3. N. Burshtein, K. Zografos, A.Q. Shen, R.J. Poole, S.J. Haward, "Inertio-elastic flow instability at a stagnation point", Physical Review X, 7 (4), 041039, 2017 [3].
  4. K. Zografos, N. Burshtein, A.Q. Shen, S.J. Haward, R.J. Poole, "Elastic modifications of an inertial instability in a 3D cross-slot", Journal of Non-Newtonian Fluid Mechanics, v. 262, p. 12-24, 2018 [4].

Date: April, 2020
Signature: Noa Burshtein.

Abstract

Flow Instabilities and Vortex Dynamics in Intersecting Flows

Flow instabilities frequently arise in the proximity of stagnation points, often resulting in the formation of vortices. Predicting vortex formation and dynamics is important for numerous applications including engineering of bridges, airplanes and pipelines. However, vortices are intermittent in nature and it is a challenge to control and study their dynamics. Here we induce vortex formation in 4-way intersections, in which the onset of flow instability is highly sensitive to small changes of the experimental parameters (i.e., channel depth:width ratio α, fluid properties and the Reynolds number, Re). Microfluidic cross-slot geometries, with a novel configuration, are fabricated by selective laser-induced etching in fused silica glass, enabling quantitative flow velocimetry measurements at the cross-section of the intersecting region. By precisely controlling Re, the breaking of symmetry between 4-cells of Dean vortices is initiated at a critical value $10 < \mathrm{Re}_c < 110$, and two co-rotating Dean vortices are induced to merge into a single steady vortex. Subsequent reduction in Re induces a vortex splitting process and the regaining of symmetry. Increasing α results in faster merging dynamics and for $\alpha > 0.55$ the transition becomes hysteretic. By adjusting α and imposing $\mathrm{Re} \gg \mathrm{Re}_c$, we can control the nature of periodic fluctuations which are governed by the central vortex core structure and the presence of side vortices in the surrounding flow field. Additionally, we find that a slight increase of the elasticity of the fluid, by introducing small quantities of flexible polymers, destabilizes the flow, resulting in symmetry breaking at reduced Re_c. We also find that the polymer torque acts counter to the vorticity, reducing the vortex intensity. Our experiments show that by tuning α, Re and elasticity we gain precise control over the intensity, core structure, dynamics and periodic fluctuations of the vortical flow field at the intersection. These experiments capture fundamental processes that govern flow transitions and provide important insights into the mechanisms of symmetry breaking, vortex dynamics and of turbulent drag reduction by polymers. Our findings contribute to the improvement of flow control and advancement of applicable technologies in which vortex suppression is required (i.e., stabilization of structures), or when vortex induced motion is desired (i.e., energy harvesting, mixing enhancement) and are transferable to systems with similar flow behavior (i.e., Taylor-Couette apparatus, T-channels, flows around cylinders and at the wake of airplane wings).

Acknowledgment

I wish to express my sincere appreciation to my supervisors Professor Amy Shen and Dr. Simon Haward who kindly supported me in a highly professional manner, for their valuable insights on this work, elaborated discussions and attention to fine details.

I wish to show my gratitude to our collaborators, Professor Rob Poole and Dr. Kostantinos Zografos from the university of Liverpool, who conducted the numerical simulations for parts of this thesis.

I wish to thank Professor Anke Lindner who welcomed me in her lab in Paris for the past year.

I would like to express my gratitude to Kazi who helped me with fabrication and design of the microfluidic channels and with various other problems which he always had creative solutions for. I am also grateful for the support of Yuno who always kindly helped with all the administrative matters.

I would like to thank the thesis committee members, Professor Mahesh Bandi and Professor Pinaki Chakraborti for their insightful comments and to the thesis examiners Professor Gregory Falkovich and Professor Anderson Shum for their valuable time spent on reading and evaluating this thesis.

I owe many thanks to the Micro/bio/nanofluidics unit members who've been a great company, Shivani, Ainash, Doojin, Atsushi, Francesco, Mandi, Paul, Kang, Cameron, Riccardo, Santo, Nikhil, Viviane and Mariana. I also owe my appreciation to members of the PMMH lab in Paris, Francesca, Sebastian, Tau, Antonios, Lucie, Jean, Lucas and Martyna.

I am grateful for the financial support given by OIST and research fellowship by Japan Society for the Promotion of Science and to the Graduate school team for all their help.

I would like to thank my family and friends, especially to my parents and sisters who are very far but somehow their encouragements always felt very close. Most of all I would like to thank Orestes and Elaia who held my hand every day and gave me the strength to push through.

Abbreviations

3D	three dimensional
CaBER	capillary break-up extensional rheometer
CAD	computer aided design
CW	clockwise
CCW	counter clockwise
CMOS	complementary metal-oxide-semiconductor
Da	dalton
DI	de-ionized
DSD	differential spinning disk
EIT	elasto-inertial turbulence
FENE-MCR	finitely extensible non-linear elastic - modified Chilcott-Rallison model
FFT	fast Fourier transform
fps	frames per second
GNF	generalized Newtonian fluid
kDa	kilo Dalton
MDa	mega Dalton
MDR	maximum drag reduction
μ-PIV	micro particle imaging velocimetry
NA	numerical aperture
OSCER	optimized shape cross-slot extensional rheometer
PDMS	poly-(dimethylsiloxane)
PAA	polyacrylamide
PEG	polyethyleneglycol
PEO	polyethyleneoxide
PIV	particle imaging velocimetry
PPM	parts per million
PSD	power spectral density
PTFE	polytetrafluoroethylene
rpm	rounds per minute
SI	supplementary information
SLE	selective laser-induced etching
SRM	slow retraction method
WD	working distance

Dedicated to my family

Contents

List of Figures

List of Tables

Chapter 1

Introduction

Fantastic vortices and where to find them

Vortices are common flow structures that are characterized by a swirling motion around an axis. The study of vortex formation and dynamics has been an active research topic in the field of fluid dynamics. In the following section, the high prevalence and importance of vortices in diverse environments and across length scales is presented to motivate this thesis.

First, we introduce the Reynolds number (Re) which is a non-dimensional quantity that captures the relative importance of inertial and viscous forces in the flow:

$$Re = \frac{\rho U w}{\eta}, \tag{1.1}$$

where U is the average flow velocity, w is the characteristic length scale, ρ is the density and η is the dynamic viscosity of the fluid.

In geophysical flows, with large characteristic length scales ($w > 10^3$ m) and high Re, vortices occur frequently, particularly in the atmosphere where they strongly influence the weather. For example, the polar vortex, which swirls in the upper levels of the atmosphere above the poles, is subjected to temperature changes that may lead to a vortex splitting process. The newly formed vortices migrate towards north America and Europe, which results in extreme weather events in those regions [10–12]. Other atmospheric vortices form in the tropics and can induce violent storms such as tornadoes and hurricanes (Fig. 1.1 a) [13].

Vortices of smaller length scales ($w < 1$ m), are also common in nature and often serve as a contributing factor in the mechanism of flying and swimming animals [14, 15]. Additionally, vortices have a role in long range transport of seeds. The effective flight mechanism of the dandelion seed, for example, relies on a special structure of the seed that stabilizes a vortex that forms above it as it is being carried by the wind (Fig. 1.1 b) [6, 16].

Vortex flows and their dynamics are important in many industrial and engineering applications. In particular, the formation of trailing vortices in the wake of airplanes are of special interest since their formation may lead to unpredictable turbulent flow which will result in redirection of air traffic (Fig. 1.1 c) [17, 18]. Additionally, vortex dynamics is of special importance in engineering of marine and terrestrial structures.

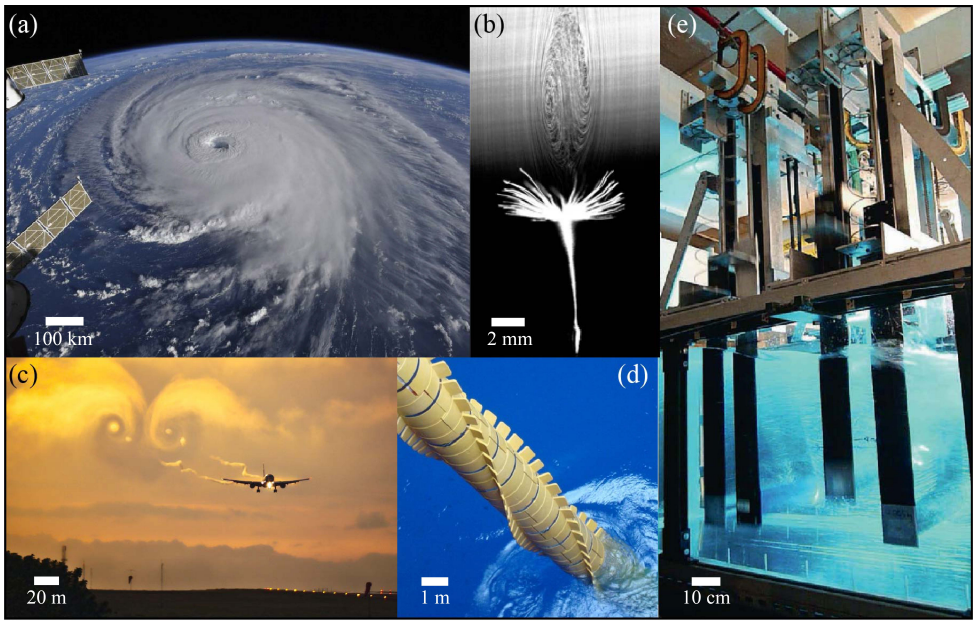

Figure 1.1: Vortices in different scales and environments: (a) Hurricane Florence as seen from the international space station [5]; (b) A vortex flow field in the proximity of the dandelion seed, supporting its flight mechanism [6]; (c) Trailing vortices in the wake of an airplane [7]; (d) A pipe with protection against destructive vortex induced motion [8]; (e) Demonstration of energy harvesting by vortex induced motion [9].

When fluid flows are interrupted by an obstacle, swirling flow patterns may emerge above a critical Re downstream of the obstacle [19]. The resulting motion feedsback on the obstacle and may be destructive for structures such as bridges, pipes, buildings and underwater cables (Fig. 1.1 d) [19, 20]. Nevertheless, these swirling flows may develop time periodic patterns, which are recently being acknowledged for their potential as a source for renewable energy from fluid flows (Fig. 1.1 e) [9, 21].

In low Re flows, pipes and channels with small length scales ($w < 10^{-3}$ m), vortices can still play a significant role in the fluid dynamics, particularly at flows around obstacles, bends and at intersections [1–3, 22–31].

Vortices are also generated in inviscid environments such as superfluids and electromagnetic fields. The dynamics of these vortices resembles two dimensional ideal flows [32–34], and they are often analyzed with classical fluid dynamics tools [35, 36].

Vortices arise in the development of many flow instabilities and they can be considered to be the building block of turbulent flows, as they form more defined (coherent) structures which contain most of the kinetic energy in the flow [37, 38]. Vortex dynamics (i.e., merging and splitting) greatly influence the energy cascade of turbulent flows [39–41].

In turbulent flows, the friction factor rises abruptly when compared to laminar flows at similar Re. Introducing elasticity to a fluid by adding long-chain polymers result in drag reduction of turbulent flows [42]. Turbulent drag reduction occurs when polymer concentration is very low, at the order of ~ 10 parts-per-million by weight, this small addition of polymers can reduce friction drag by up to 80% [43].

Vortices are naturally unstable and hence it is a challenge to predict their formation, intensity and dynamics. A deeper understanding of the fundamental aspects of the nature of vortical flows is of high importance in the prediction of natural flows, for improvement of industrial flows and engineering applications, and for renewable energy sources.

Research questions

Vortex formation and vortex dynamics will be explored using a novel configuration of microfluidic flow intersections. By controlling different parameters in the experiments (i.e., flow rates, elasticity and characteristic length scale) it will be shown how symmetry breaking flow instabilities, vortex properties and even vortex dynamics can be tuned. Although microfluidics is not a common tool for the study of inertial flows, it will be demonstrated that microfluidics allows exceptional control over the flow field and enables the study of flow phenomena that otherwise is not attainable. The major questions that will be addressed are:

1. How can we precisely control vortex formation, properties and dynamics by using microfluidics?
2. What are the effects of spatial confinement on a vortex?
3. How does the nature of a flow instability affect vortex dynamics?
4. Can microfluidics be a useful tool to study vortex dynamics and unsteady flows with general applicability?
5. How does changing fluid elasticity affect vortex formation and properties?

In the following introductory section, a comprehensive background and literature review that are needed to answer these questions will be presented.

1.1 Flow instabilities and vortex formation

Flow instabilities can lead to formation of vortices, which may develop to turbulent flows under certain conditions. Inertial flow instabilities are initiated once critical conditions are met, resulting in symmetry breaking of the flow field. These conditions depend on a combination of parameters that are captured by Re (Eq. 1.1).

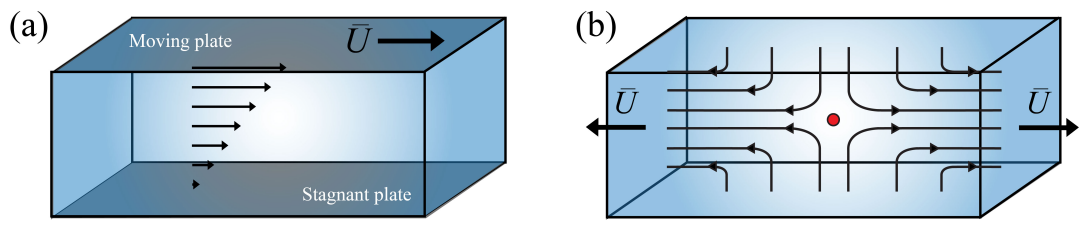

Figure 1.2: Shear flow and planar elongation flow. (a) Couette flow between two parallel plates, the upper plate is moving at velocity U and the bottom one is fixed. (b) Planar elongation flow, the fluid is being subjected to outflow in two opposing directions, which leads to formation of a stagnation point (in red).

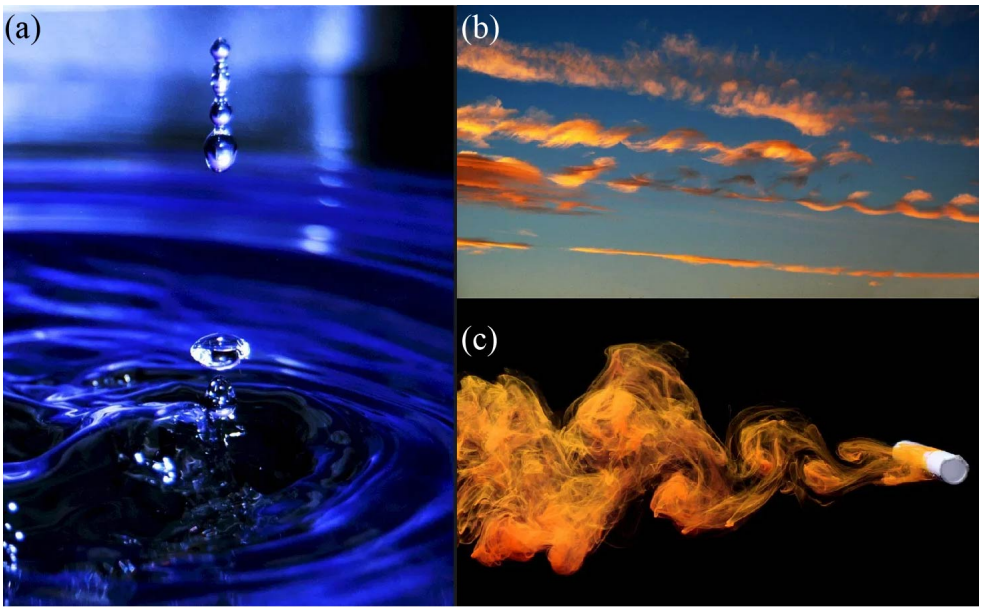

Figure 1.3: Common flow instabilities: (a) Rayleigh-Plateau instability. (b) Kelvin-Helmholtz instability. (c) von Kármán vortex street [45].

Another important factor that influences the development of flow instabilities is the flow field itself. A commonly occurring flow is the Couette flow (simple shear flow field), in which a fluid is being sheared by an external force. For example, a fluid confined between two parallel plates is being sheared by the relative movement between the two plates. The velocity of fluid particles which are adjacent to the moving plate will be the same as the moving plate velocity (e.g. no slip boundary condition). A gradient in the velocity profile is seen as the fluid velocity gradually decreases until full arrest at the bottom plate where the velocity $\bar{U} = 0$ (Fig. 1.2 a). Another common flow type in which flow instabilities frequently emerge is the planar elongation flow (Fig. 1.2 b) in which the fluid accelerates away from a stagnation point, leading to streamwise velocity gradients [44]. A few examples where this flow type appears are intersections (Y-, T-, X-) and flows around obstacles.

Several well known flow instabilities appear in shear flows, where they are initiated at the interface between two fluids that move at different velocities or have different viscosities, such as the Rayleigh-Plateau (Fig. 1.3 a), the Rayleigh-Taylor and the Kelvin-Helmholtz instabilities (Fig. 1.3 b). Flow instabilities such as von Kármán vortex street, develop at planar elongation flows which involve stagnation points that are formed around physical obstacles (Fig. 1.3 c) [46].

Additionally, there are flow instabilities that involve curving streamlines, such as the Taylor-Couette flow instability which is described in the following subsection.

1.1.1 The Taylor-Couette flow instability

The Taylor-Couette flow cell is a benchmark configuration in the study of transition to turbulent flows. A Taylor-Couette cell consists of two concentric cylinders of identical height (l) and different radii $r_1 < r_2$ with fluid filling the gap ($r_0 = r_2 - r_1$) between

them. Rotation of the inner cylinder induces angular velocity, v_ω and fluid motion that is subjected to centrifugal forces (Figure 1.4 a) [47]. The centrifugal forces are greater on the fluid particles that are close to the inner cylinder than near the walls of the outer cylinder. As a result, faster moving fluid particles near the center are forced to move toward the outer surface. Upon a critical angular velocity, $v_{\omega,c1}$, a flow instability emerges, resulting in the formation of a stack of counter-rotating vortex pairs, also known as "Dean vortices" [48]. In the Taylor-Couette cell, these vortices are named "Taylor vortices" and they commonly appear in curving flows (Figure 1.4 a) [47].

When the aspect ratio ($\alpha = l/r_0$) of a Taylor-Couette cell is kept small ($\alpha \simeq 1$) only one pair of counter rotating vortices can form (Figure 1.4 b). Increasing the angular velocity of the inner cylinder above second critical angular velocity, $v_{\omega,c2}$, results in a secondary flow instability where the symmetry between the vortex pair breaks, as one vortex intensifies at the expense of the other (Figure 1.4 c). An increase in α will result in a change from a smooth to abrupt transition [49, 50]. This secondary transition is well described by the Landau model of phase transition near tricritical points (which will be discussed in Chapter 3).

At flow intersections there is a unique combination of curving streamlines and a free stagnation point, which leads to destabilization of the flow field at relatively low Re. In sections 1.1.2-1.1.4 experimental evidence of inertial flow instabilities at intersecting flows will be presented, focusing on the cross-slot geometry (length scales in the order of $10^{-4} < w < 10^{-3}$ m) and covering the literature on this topic to date.

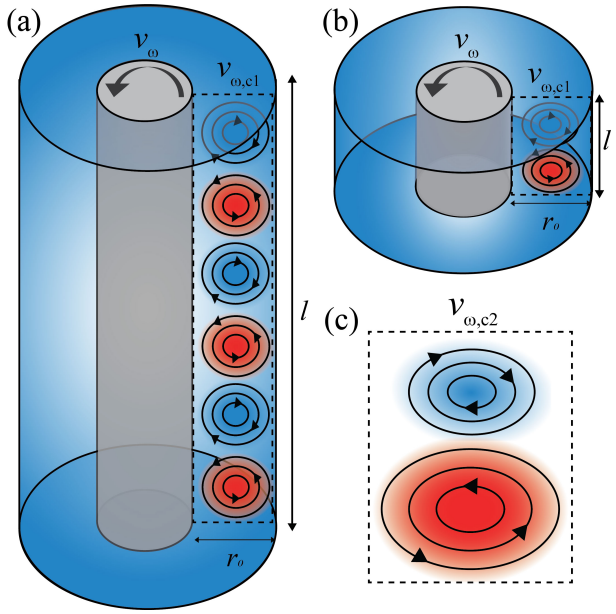

Figure 1.4: Perspective view of Taylor-Couette flow cell. Counter rotating vortices form along the gap between the two cylinders at $v_{\omega,c1}$. (a) High aspect ratio Taylor-Couette flow cell with a stack of vortices; (b) Low aspect ratio Taylor-Couette cell with a single pair of counter rotating vortices; (c) Above a critical flow rate $v_{\omega,c2}$, the symmetry between the vortices breaks as one vortex grows on the expense of the other.

1.1.2 Flow instabilities at intersections

"..in hydrodynamic turbulence... the fate of vortices extending in the direction of motion is of great importance." (Burgers, 1948) [51].

As mentioned above, planar elongation flow fields (Fig. 1.2) which involve a stagnation point flow, will become unstable at a critical Re (Re_c). These instabilities will develop into streamwise vortices that extend in the direction of the flow, such as the Burgers vortex, which is a common feature of turbulent flows [51].

A particularly strong planar elongation flow field can be formed by simultaneously stretching the flow in two opposing directions. There are two known ways to form planar elongation flow field which is symmetrical in the directions of the inflow and the outflow, one is the 4-roll mill apparatus and the other is the cross-slot geometry.

The 4-roll mill apparatus, which consists of 4-rollers submerged in four corners of a cuboid fluid tank (Fig. 1.5 a), was one of the first flow configurations in which scientists recognized a stagnation point flow instability at a flow intersection. The 4-roll mill apparatus was already used by Taylor in 1934 to form extensional flows and study drops and emulsions that were trapped at the stagnation point [53].

In a different, more recent study (Lagnado et al., 1990), a viscous mixture of water and glycerol was used, the 4-rollers were then rotated simultaneously, to induce extensional flow (Fig. 1.5 a & b). Re was gradually increased by increasing the rotation rate of the rollers, and upon a critical value of $Re_c \simeq 40$ a three-dimensional flow structure appeared. A side view of the tank revealed that the flow took a shape of a streamwise spiral vortex, with counter rotating vortices formed above and below it (Fig. 1.5 b & c) [52].

Similar streamwise vortices that developed around stagnation point flows were mathematically predicted in colliding flow streams at intersecting flows [54]. Additionally, these vortices were found to form a periodic array of counter rotating vortices located at the plane of symmetry in a stagnation-point flow [55].

Similar to the findings from the 4-roll mill apparatus, a 3D flow structure, evidence of a stack of counter rotating vortices, appeared above Re_c in cross-slot channels with

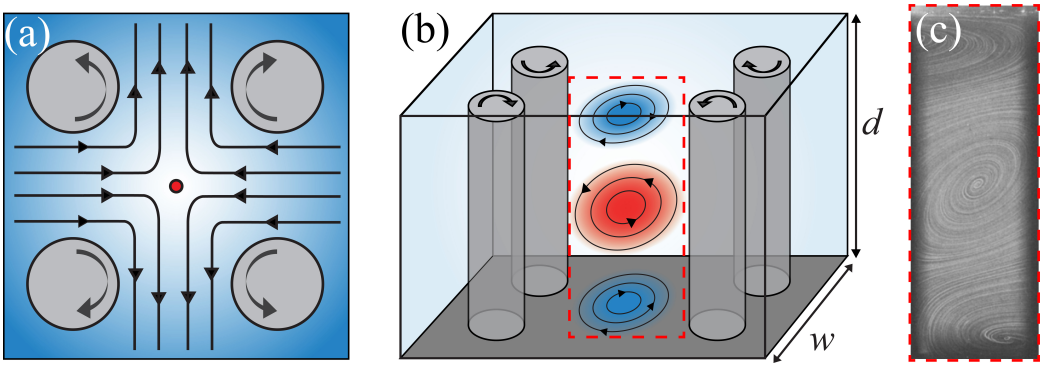

Figure 1.5: The 4-roll mill apparatus, (a) top and (b) perspective view of the 4-roll mill; (c) a picture of the plane highlighted in red dashed line (in b) showing experimental evidence of the vortex in the 4-roll mill at Re = 54 [52]. w and d are the width and depth of the geometries, the stagnation point is indicated in red in (a).

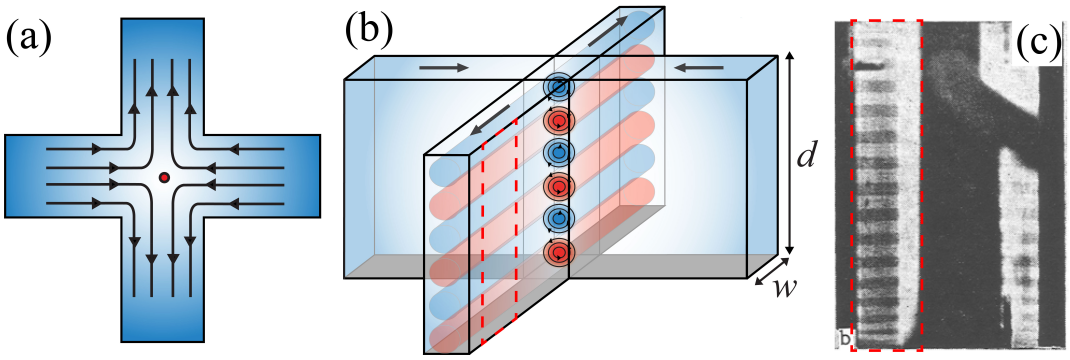

Figure 1.6: Deep cross-slot channel, (a) top and (b) perspective view of the cross-slot geometry; (c) a picture of the plane highlighted in red dashed line (in b) showing the stack of vortices in the cross-slot at Re = 64 [56]. w and d are the width and depth of the geometries, the stagnation point is indicated in red in (a).

high aspect ratios ($\alpha = d/w$, where w is the width and d is the depth of the channel) of $\alpha = 262$ and of $\alpha = 32$ (Fig. 1.6 a & b). From a side view of the geometry, the instability displayed as a striped structure of streamwise vortices stacked through the depth of the flow cell (Fig. 1.6 b & c) [56]. The cross-slot channels used in these experiments can be considered as microfluidic channels as their characteristic length scales were $w = 0.4$ mm (for $\alpha = 262$) and $w = 0.8$ mm (for $\alpha = 32$).

1.1.3 Inertial flow in microfluidic intersections

The common conception in the field of microfluidics is that fluid inertia is negligible and that the flow is governed by Stokes flow regime (Re $\rightarrow$ 0). However, in microfluidics it is possible to access intermediate inertial flow regimes at moderate Re numbers in the range of $1 <$ Re < 100 (inertial microfluidics) [57]. In these intermediate flows, both inertia and viscosity of the fluid are finite, and non-linear secondary flows arise. The interest in inertial microfluidics has been growing in the past few years due to diverse practical applications [58]. Non-linear microfluidics is commonly used for various purposes such as heat transfer [59], particle arrangement and manipulation (using curved channels [60], straight channels [61], obstacles [57] and intersections [62]) and for mixing enhancement (at intersections [63, 64], staggered herringbone structure [65], sudden expansions [66] and many other active and passive mixing techniques [67]). Additionally, inertial microfluidics is used to study vortex breakdown phenomena that is applicable for particle trapping, either in T-channels with straight inlets [23, 29] and with offset inlets [31, 68].

Flow intersections, and particularly T-shaped and cross-slot geometries, have additional widespread practical purposes. For example, these geometries are used in lab-on-a-chip devices [66], micro-reactors [69], flow cytometers [70] flow focusing [71] and droplet generation [72]. The use of these devices is contributing to advancement in biotech research [73] and in environmental measurement techniques [74, 75].

The central stagnation point that is formed at intersetions, is particularly important for elongation flow studies of complex fluids, rheological measurements and stretching of DNA, polymers and wormlike micellar solutions in the T-shaped [76] and in the cross-

slot devices [44, 77–79]. The cross-slot device has been instrumental to advance the understanding of polymer dynamics in strong flows [80–84] and as a consequence has become widely considered as a benchmark flow for study of complex fluids. Recently, the cross slot geometry was also employed to study electro-elastic instabilities [85] and elastic turbulence [86].

As demonstrated above, microfluidics and more specifically, microfluidic intersections, may exhibit inertial and non-linear properties. Particularly, the cross-slot geometry that is common in various applications is of high interest. In the next subsection the inertial flow instability in the cross-slot geometry will be further described.

1.1.4 Flow instability at the cross-slot intersection

In this thesis, a symmetric configuration of the cross-slot channel with a crossing angle of 90° will be considered. The fluid is always inserted from two opposing inlets and exits from two opposing outlets (Fig. 1.7 a). The crossing angle of a cross-slot geometry strongly affects the critical Re needed for the flow instability to emerge. The smallest Re_c for the onset of the instability was found to be for intersections with an angle of 90°, which makes it the optimal angle for achieving inertial instabilities [87]. The cross-slot geometry is often used to study extensional flow fields which appear in the horizontal plane ($x-y$ or $z=0$) as seen in Fig. 1.7 b. Close to the stagnation point of the cross-slot geometry, the flow field approximates to pure planar elongation [88, 89]. The inertial flow instability in the cross-slot is a three-dimensional (3D) instability. The detailed spiral structure of the Dean vortices and the streamwise vortex can be visualized at the vertical plane ($y-z$ or $x=0$) around the stagnation point where $x=y=z=0$ (Figure 1.7 c). This plane is not easily attainable for direct visualization due to the high water column of the outlet channel.

Recently, laser scanning confocal microscopy was used for visualization of the flow structure in the inner $y-z$ plane at the cross-slot indirectly. The flow was visualized by using water from one inlet and water pre-mixed with fluorescent dye from the other inlet (Figure 1.8) [90], similar to a previous study [63, 64]. In these experiments, scans

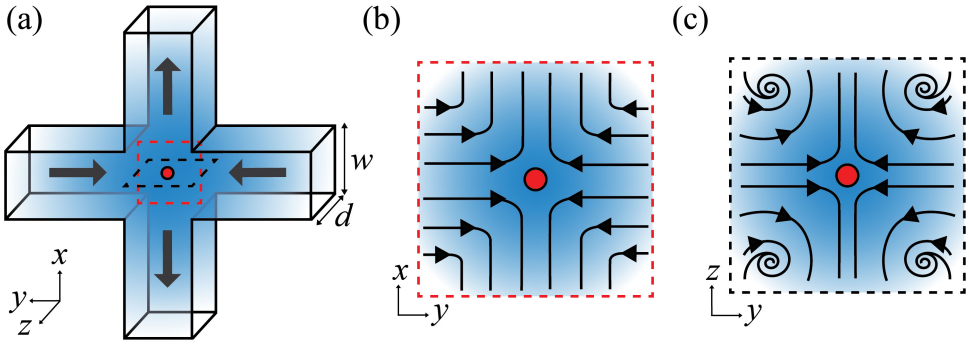

Figure 1.7: The cross-slot geometry (a) A 3D cross-slot geometry, inflow and outflow are indicated with arrows. A stagnation point is formed at the center of the geometry, marked in red. (b) The flow field in the $x-y$ plane exhibiting extensional flow. (c) Flow field of the $y-z$ plane of the geometry, the plane in which the spiral structure of streamwise vortices can be seen.

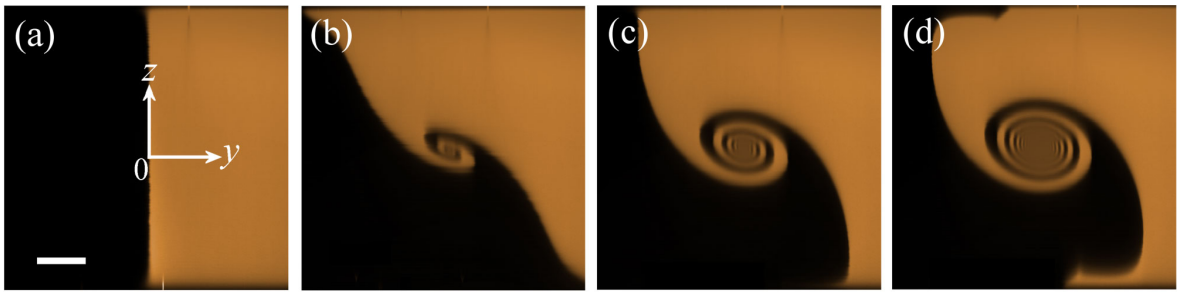

Figure 1.8: Dye advection patterns of a spiral vortex flow instability across the $y-z$ plane of a cross-slot geometry with $\alpha = 1$. Flow visualization is done by adding fluorescent dye to the right inlet. (a) Re = 5.2; (b) Re = 42.8; (c) Re = 60.6; and (d) Re = 91.0. Scale bar in (a) is 200 μm [27].

of the $x-y$ plane were taken along z direction. These z-stack image reconstruction revealed that the spiral vortex structure developed in the mid-plane, at the stagnation point. Pixel intensity analysis was used to study the growth of the spiral vortex for increasing Re, for four different aspect ratios $\alpha = 0.49$, 1.0, 1.85 and 3.87 of the cross-slot. It was found that the transition and growth of the spiral vortex could be characterized by the mixing between pure and dyed fluid streams.

Supported by numerical simulations that were conducted for a few additional aspect ratios, it was also found that the critical Re (Re_c) in which symmetry breaking flow instabilities arise, was strongly dependent on the aspect ratio of the channel: low aspect ratio cross-slot device required higher Re_c (i.e., for $\alpha = 0.49$, $\mathrm{Re}_c = 100$) and high aspect ratio cross-slot device required lower Re_c (i.e., for $\alpha = 1.85$, $\mathrm{Re}_c = 23$). The vortex size grew with increasing Re, enabling larger interfacial areas between the fluid streams and thus enhanced the diffusive mixing downstream.

In the following subsection a suggested mechanism for the development of the flow instability reported by Haward et al. [27] will be presented. The mechanism of the flow instability is explained with the dynamics of the flow transition.

1.2 Vortex dynamics at cross-slot flow

1.2.1 Mechanism and onset of the flow instability

In order to understand the mechanism of the flow instability, we look at the governing equations of the Newtonian flow in the cross-slot geometry, the Navier-Stokes equation:

$$\frac{\partial \overline{v}}{\partial t} + \overline{v} \cdot \overline{\nabla} \overline{v} = \frac{-1}{\rho} \nabla P + \nu \nabla^2 \overline{v} + \overline{\nabla} G, \tag{1.2}$$

and mass conservation for incompressible fluids

$$\overline{\nabla} \cdot \overline{v} = 0, \tag{1.3}$$

where v is the fluid velocity, t is time, ρ is the density, P is the pressure, ν is the kinematic viscosity, and G is the gravitational force.

Vorticity is defined as the curl of the velocity $\overline{\omega} = \overline{\nabla} \times \overline{v}$, and hence the vorticity equation is:

$$\frac{\partial \overline{\omega}}{\partial t} + (\overline{v} \cdot \overline{\nabla})\overline{\omega} = (\overline{\omega} \cdot \overline{\nabla})\overline{v} + \nu \nabla^2 \overline{\omega}. \tag{1.4}$$

The left hand side of Eq. 1.4 is the material derivative and the equation can be written as:

$$\frac{D\overline{\omega}}{Dt} = (\overline{\omega} \cdot \overline{\nabla})\overline{v} + \nu \nabla^2 \overline{\omega}, \tag{1.5}$$

where the 1st term on the right hand side is the rate of deformation of vorticity and the 2nd term is viscous diffusion.

In order to find the vorticity at the stagnation point $\omega_x \mid_{x=y=z=0}$ where the streamwise vortex is formed and stretched, we consider only the x component of Eq. 1.5:

$$\frac{\partial \overline{\omega}_x}{\partial t} = \overline{\omega}_x \frac{\partial \overline{v}_x}{\partial x} + \nu [\frac{\partial^2 \omega_x}{\partial x^2} + \frac{\partial^2 \overline{\omega}_x}{\partial y^2} + \frac{\partial^2 \overline{\omega}_x}{\partial z^2}]. \tag{1.6}$$

The terms in Eq. 1.6 are non-dimensionalized as follows: $\omega_x^* = \omega_x w/v$, $t^* = tv/w$, $x^* = x/w$, $y^* = y/w$, $z^* = z/d$, which leads to the non-dimensional center point vorticity:

$$\frac{\partial \overline{\omega}_x^*}{\partial t^*} = \overline{\omega}_x^* \frac{\partial \overline{v}_x^*}{\partial x^*} + \frac{1}{Re} [\frac{\partial^2 \overline{\omega}_x^*}{\partial x^{*2}} + \frac{\partial^2 \overline{\omega}_x^*}{\partial y^{*2}} + \frac{1}{\alpha^2} \frac{\partial^2 \overline{\omega}_x^*}{\partial z^{*2}}]. \tag{1.7}$$

The 1st term on the right hand side of Eq. 1.7 refers to vortex stretching and the 2nd term refers to viscous diffusion. By non-dimensionalizing Eq. 1.6, we identify the dimensionless groups that govern the flow: α (the aspect ratio of the flow channel) and the Reynolds number.

These equations were used in time dependent numerical simulation that was performed for the cross-slot geometry, showing that the transition could be described as a stagnation point instability coupled to vortex stretching [27].

When $\mathrm{Re} \ll \mathrm{Re}_c$, the diffusion term dominates the dynamics and the flow is stable and symmetric (Fig. 1.9 a). When $\mathrm{Re} \lesssim \mathrm{Re}_c$, the diffusion term still dominates the dynamics, disturbances are suppressed by viscosity and the flow is stable and symmetric.

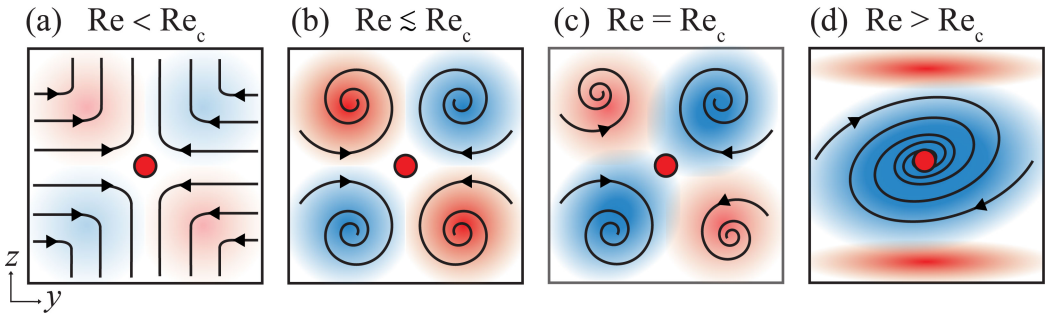

Figure 1.9: Illustration of the instability mechanism in the cross-slot geometry; red and blue colors indicate clockwise and anticlockwise rotation, respectively; (a) $\mathrm{Re} \ll \mathrm{Re}_c$, stable symmetric flow field; (b) $\mathrm{Re} \lesssim \mathrm{Re}_c$, formation of 4-cells of Dean vortices, flow field is stable and symmetric; (c) $\mathrm{Re} = \mathrm{Re}_c$, two co-rotating Dean vortices intensify and center point vorticity is generated; (d) $\mathrm{Re} > \mathrm{Re}_c$, a central vortex is formed by the merging process of two co-rotating vortices.

However, 4-cells of Dean vortices develop due to the curving streamlines of the flow (Fig. 1.9 b). When $\mathrm{Re} = \mathrm{Re}_c$ symmetry breaks, two co-rotating Dean vortices intensify at the expense of the two counter rotating vortices and center point vorticity is generated, the vortex stretching term, $\overline{\omega}_x^* \frac{\partial \overline{v}_x^*}{\partial x^*}$, grows and $\frac{\partial \overline{\omega}_x^*}{\partial t^*} > 0$ (Fig. 1.9 c). Similar to the experimental findings (Fig. 1.8), when $\mathrm{Re} > \mathrm{Re}_c$ numerical simulations found that $\frac{\partial \overline{\omega}_x^*}{\partial t^*}$ continues to grow as a central vortex is formed (Fig. 1.9 d).

As apparent from the mechanism shown in Fig. 1.9, the intensified Dean vortex pair that formed in the symmetry breaking stage, is the foundation for the central vortex formation and the determining factor of the central vortex direction of rotation. Therefor we will further explore the dynamics between co-rotating vortices and introduce the topic in the following section.

1.2.2 Dynamics of co-rotating vortices

The merging process of two co-rotating vortices has been broadly studied due to its practical importance to aircraft trailing vortices. Experimental data and numerical simulations of trailing vortices have been used to study the mechanism of vortex merging process which has been discussed in several studies [91–99].

Although there is still an ongoing debate about how to define a vortex [100, 101], there is a general agreement that the mechanism of merging consists of three main stages: (1) The first stage of merging is recognized as the slow stage in which diffusive growth of the vortex cores is seen and the vortex cores slightly move towards each other (Fig. 1.10 a). (2) Once a critical ratio between the core size (a) and the distance (b/b_0) is met, typically $0.24 \leq a/b \leq 0.32$, a convective stage will begin. In the fast convective stage, the vortices will deform, share filaments and will rapidly move towards each other (Fig. 1.10 b). (3) The last stage is called the second diffusive stage in which the vortices have merged into a single structure (Fig. 1.10 c) [98, 99, 102, 103]. Some studies have reported a fourth stage in the merging process, which is referred to as a second diffusive stage (a slow down in the merging process), that follows the convective stage, prior to the final merging, see experimental studies Fig. 1.10 d and numerical simulations in Fig. 1.10 e [92–94].

In contrast to vortex merging, the process of vortex splitting is much more challenging to induce and study, and experimental evidence of the phenomenon is scarce [104–107]. Vortex splitting was theoretically predicted decades ago, and was supported with computational evidence [108–110]. Experimental observation of vortex splitting were first reported by Freymuth et al. [104, 105]. Their experiments validated the previous theoretical predictions, by the observation of vortex splitting behind an airfoil where regions of vorticity of opposite signs were formed. Later on, numerical simulations revealed that the process of merging and splitting of Dean vortex pairs, in curved and rotating channel flows, could be attributed to spanwise perturbations which are known as the Eckhaus instability [106]. Additional reports suggest that merging and splitting events in arrays of counter-rotating Dean vortices are associated with the spacing between vortex pairs and are affected by centrifugal instabilities [107].

In this thesis, cross-slot geometries will be used to induce controlled merging and

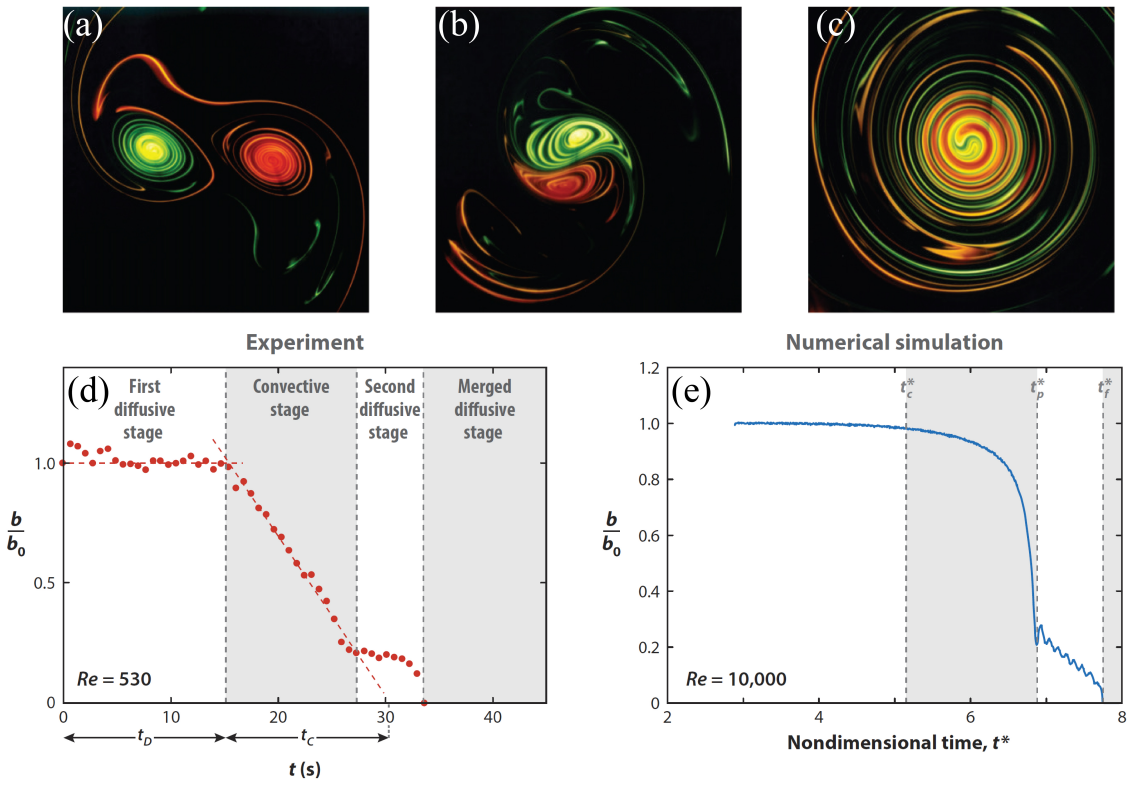

Figure 1.10: Various stages of vortex merging process; (a) First diffusive stage, growth of vortex cores; (b) Convective stage, vortices rapidly move towards one another; (c) Second diffusive stage in which the vortices have merged into a single structure. Figures (a-c) are taken from [93]. Evolution of the normalized vortex separation b/b_0 with time during merging; (d) Experimental data with Re = 530 [92]; (e) Direct numerical simulation at Re = 10,000 [94].

splitting of co-rotating vortices as will be shown in Chapter 4. In the following subsection we will introduce additional important background that is essential in characterizing vortex flows. We will describe important mathematical models of vortices that will assist to classify the vortex that is formed in the cross-slot intersection.

1.2.3 Vortex models

Axisymmetric vortices, such as the ones that are formed in extensional flows, are vortices in which the vorticity is concentrated by axial stretching and diffused by viscous stresses. There are dozens of models that describe axisymmetric Newtonian-fluid vortices in the literature, all of which are solutions to the Navier-Stokes equations. In Fig. 1.11 the normalized velocity profile of ten different vortex models is plotted as a function of the normalized radius of the vortex core. The vortices for which the azimuthal velocity, v_θ (in cylindrical coordinate system), can be described by an exponential function, include Lamb-Oseen, Burgers, Newman, Sullivan, Batchelor and others [111].

Interestingly, all these vortex models have common characteristics and can be

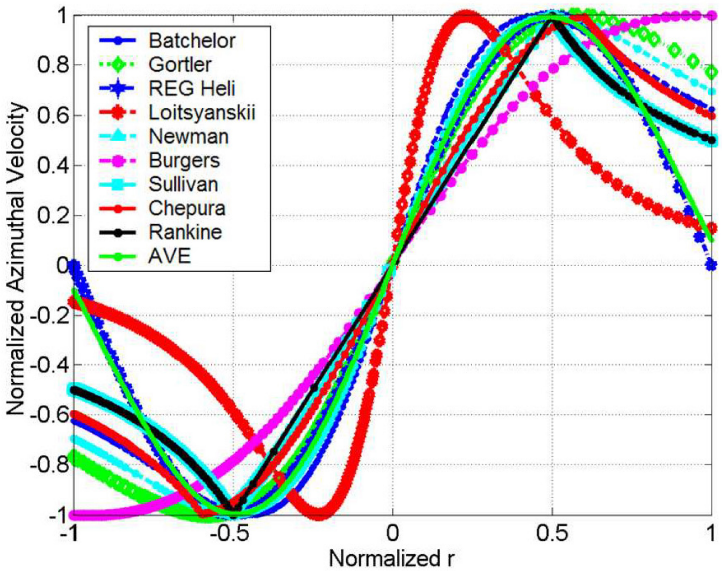

Figure 1.11: Comparison between the tangential velocity profile of different vortex models [111].

grouped to a single family with common mathematical traits. Three of these traits are captured by the vortex azimuthal velocity profile $v_\theta(r)$. First, at the center of the vortex, where the radius, $r = 0$, $v_\theta(r) = 0$ for all vortices. Secondly, they all share a sinusoidal profile. Third, $v_\theta(r)$ is asymmetric about r ($v_\theta(r) = v_\theta(-r)$) [111].

The Burgers and Lamb-Oseen vortices are both stagnation point vortices. The Burgers vortex is defined as a stagnation point stretched vortex for which the viscous diffusion is balanced by the concentration process induced by stretching. The radius of the Burgers vortex is described by $\delta_B = (\nu/\gamma)^{0.5}$, where ν is the kinematic viscosity of the fluid and γ is the stretching rate of the external stretching field.

A Lamb Oseen vortex is a non-stretched stagnation point vortex which is mainly affected by viscous diffusion. The vortex radius, δ_L, increases with time according to $\delta_L = (\nu t)^{0.5}$ while the circulation Γ remains constant. The velocity profile v_θ of the Burgers vortex and the Lamb-Oseen vortex are identical when the vortex radius is normalized by $\delta = \sqrt{2\nu/a}$, where $a = 1.2564$ [112]. The Burgers and Lamb-Oseen vortices are plotted in Fig. 1.12.

Experimental evidence indicate that in the 4-roll mill apparatus, which exhibits an intersecting extensional flow field similar to the cross-slot intersection, a stack of vortices will appear upon a critical Re [52]. These vortices are reminiscent of the Burgers vortex and they are called Kerr-Dold vortices, named after the scientists who first described them [55].

Confinement of vortices within a cross-slot channel of low aspect ratio α, allows to form a single, isolated, steady and stable vortex while maintaining the streamwise component of the vortex, allowing it to stretch downstream. The description of such a vortex fits well with the Burgers vortex description, however, a confinement factor is missing and therefore the Burgers vortex model does not perfectly describe the vortex in a cross-slot with low α. There is no existing model that describes a single confined

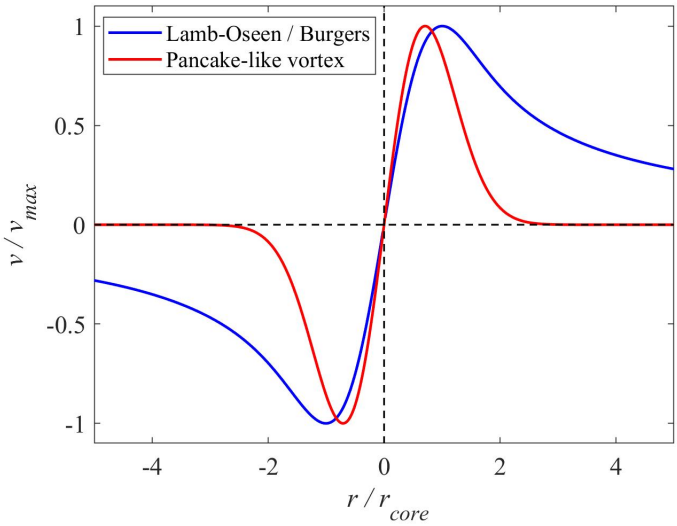

Figure 1.12: Tangential velocity profile of Lamb-Oseen - Burgers vortex and Pancake like vortex.

Burger-like vortex.

Other confined vortices, that are not stretched, such as Pancake-like vortices, are defined as vortices that are spatially confined within a stratified fluid layer, along their streamwise and spanwise directions. Pancake like vortices have an azimuthal velocity profile, v_θ, with a forced drop in the velocity due to confinement. Consequently, viscous diffusion is not the main factor influencing the velocity profile for these vortices (Fig. 1.12) [113]. It is important to note that the forced velocity drop not only affects the far edges of the vortex, it also affects the vortex core structure and stability [114].

In Chapter 5, it will be shown that changing the aspect ratio of a cross-slot geometry, significantly alters the velocity profile v_θ. This forcing affects the vortex core structure and stability, leading to time dependent periodic flows with characteristic frequencies. This leads us to the following section in which the topic of periodic flows at stagnation points and intersections is introduced.

1.2.4 Periodic flows at stagnation points and intersections

Flow instabilities may develop to unsteady time dependent flows when inertia is increased. For a certain range of Re, on their route to become chaotic and turbulent, these flows may exhibit ordered periodic cycles with typical frequencies. A benchmark example for a flow that shows periodic fluctuations is the von Kármán vortex that develops downstream of an obstacle, and has been briefly mentioned earlier in the introduction (Fig. 1.3 c). This flow instability emerges upon a relatively low critical Re, Re_c, as two attached spanwise vortices flowing downstream of an obstacle, the vortices grow in size upon an increase in Re to $\mathrm{Re} > \mathrm{Re}_c$. Upon a second critical Re, Re_p the flow becomes unsteady and the vortices are formed behind the two sides of the obstacle in an alternate manner, generating periodic asymmetric flow and consequently, vortex

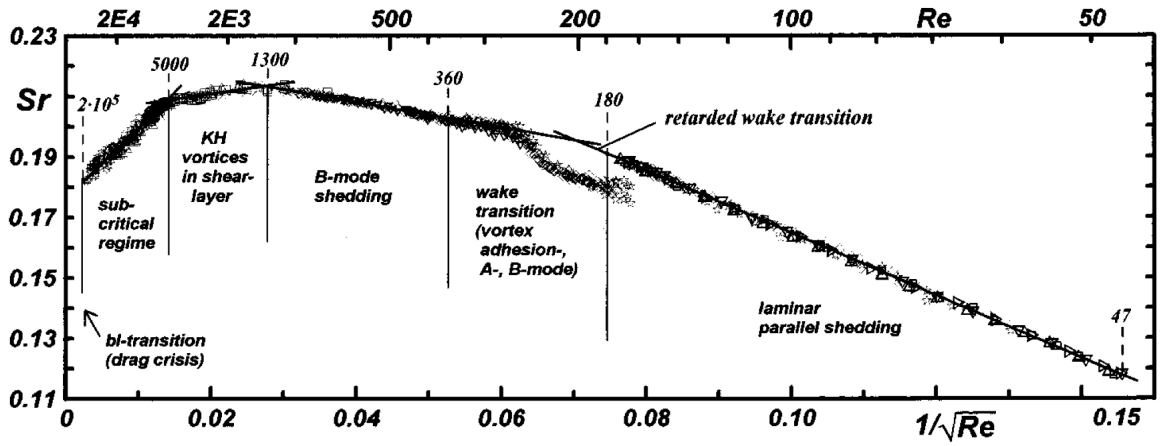

Figure 1.13: Periodic flow of von Kármán vortex street at the wake of a circular cylinder. St as a function of Re [116].

induced vibrations [115]. This periodic motion has a characteristic frequency that can be described with the non-dimensional Strouhal number (St)

$$St = fw/U, \tag{1.8}$$

where f is the frequency of the fluctuation, U is the average flow velocity and w is the characteristic length scale. For the case of flow around a circular cylinder, the relation between St and Re (for $47 \leq \mathrm{Re} \leq 180$) can be described by the following equation:

$$St = A - \frac{B}{\sqrt{Re}} \tag{1.9}$$

where $A = 0.2684$ and $B = 1.0356$. Upon an increase in Re the values of the constants A and B would slightly change, corresponding to different modes of the fluctuations as seen in Fig. 1.13 [116]. This equation is not the only way to describe the Re - St relation, other studies concerning flows around circular cylinders have described the relation between Re and St (for $\mathrm{Re} < 200$) with the following equation [117]:

$$St = x_1/Re + x_2 + x_3 Re, \tag{1.10}$$

where x_1, x_2 and x_3 are free parameters.

In recent years, periodic flows at flow intersections have been predicted by numerical simulations and are now experimentally validated. The T-shape geometry is well studied for its mixing efficiency and rich flow regimes. Different flow regimes were identified depending on the Re and the aspect ratio of the geometry, namely: stable symmetric (e.g. stratified), symmetric Dean-vortex flow, asymmetric vortex flow (e.g. engulfment flow) and unsteady flow regimes [118]. The onset of the unsteady periodic flow regime was at $\mathrm{Re} \simeq 200$, with $\mathrm{St} \simeq 0.1$, this value grew to $\mathrm{St} \simeq 0.2$ when $\mathrm{Re} \simeq 300$. The exact values slightly shifted in different studies, as seen in Fig. 1.14 [118–123].

Periodic flows with similar dependence between St number and Re were also observed in a microfluidic T-channel with offset inlets. In this work it was shown that for $120 \leq \mathrm{Re} \leq 170$, $\mathrm{St} \simeq 0.5$, corresponding to the periodically pulsating state of vortex

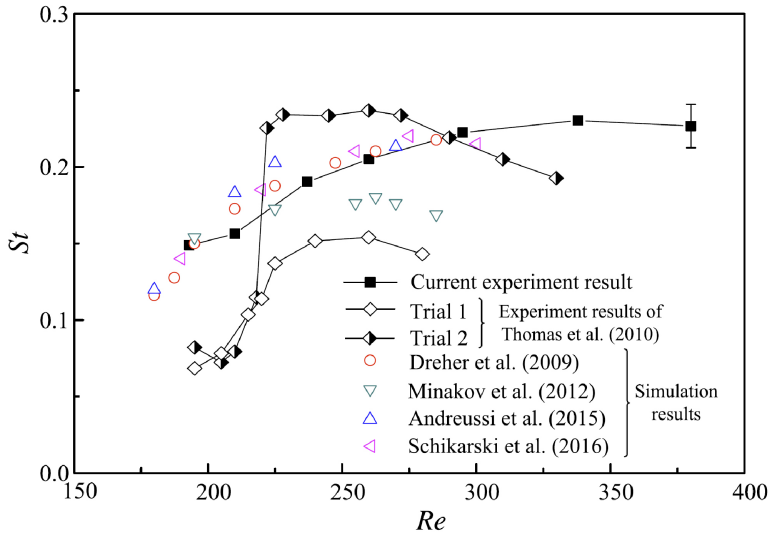

Figure 1.14: Periodic flow in T-channels. Strouhal number as a function of Re [118–123].

breakdown. For Re $\geq$ 160, St $\simeq$ 1.75 corresponds to a helically oscillating state of the vortex breakdown [31].

Very recently, in a cross-slot geometry with a square cross section and characteristic scale of $w = 10$ mm, periodic flow patterns were also observed [124]. These will be further discussed and compared to experimental results from this thesis in Chapter 5.

Other than purely inertial and confinement effects on the flow instability and vortex dynamics, there is a wide interest in weakly elastic effects on vortex flows [125–128]. The stable steady vortex in the cross-slot can serve as a simplified model to study the effects of weakly elastic flows on a single vortex. In the following section, elastic, non-Newtonian flows in the cross-slot geometry will be introduced.

1.3 Inertio-elastic effects on flow instabilities

Polymer solutions have unpredictable properties when they are subjected to the influence of a flow field. Due to their high prevalence in diverse processes it is valuable to understand their response to flows under different conditions. The following section introduces polymer solutions and their response to extensional flows.

1.3.1 Characterizing non-Newtonian polymer solutions

The cross-slot device has been instrumental in the study of polymer dynamics in strong extensional flows [80–84] and as a consequence has become widely considered as a benchmark flow for study of complex fluids. Since the device is also a component of central importance in a range of both fundamental and applied microfluidic technologies [72, 88, 129–134] it is of great importance to define conditions and stability criteria for cross-slot flows.

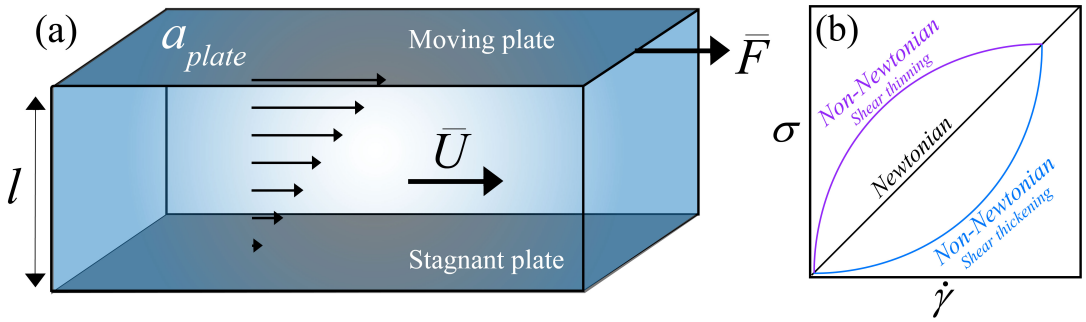

Figure 1.15: Characterizing non-Newtonian fluids: (a) Couette flow between two parallel plates, the upper plate is moving at velocity U and the bottom one is fixed. (b) $\dot{\gamma}$ as a function of σ for Newtonian and non-Newtonian shear thinning and shear thickening fluids.

Polymers are often involved in biological and industrial flows and display non-Newtonian properties. In the food industry, polymers are particularly important for the precise engineering of textures, viscosity and other properties of food products [135]. Biological fluids such as blood [136], saliva [137], mucus [138] etc. also contain natural polymers and their flow behavior is of great concern for medicinal purposes.

The properties of high molecular weight polymer solutions are non-Newtonian and they can be initially categorized by the response of the fluid to forces that are exerted upon it, or in other words, the relation between the shear stress ($\sigma = Fa_{plate}^{-1}$, where F is the force and a_{plate} is the area on which it works) and shear rate ($\dot{\gamma} = Ul^{-1}$ where U is the velocity and l is the length scale) of the flow. The relation between $\dot{\gamma}$ and σ can be measured in a Couette flow using two parallel plates as demonstrated in Figure 1.15 a. For a Newtonian fluid the relation between $\dot{\gamma}$ and σ is linear and therefore the viscosity ($\eta = \sigma\dot{\gamma}^{-1}$) is independent of $\dot{\gamma}$ and is only a function of temperature and pressure [139]. For non-Newtonian fluids, the relation between $\dot{\gamma}$ and σ is non-linear and η is a function of $\dot{\gamma}$ (see schematics in Fig. 1.15 b).

1.3.2 Purely elastic flow instabilities at intersecting flows

The non-linear response of a non-Newtonian fluid to shear can be expressed in terms of elasticity. Elasticity (relative to the viscous stress) is characterized by the ratio between the deformation rate of the flow ($\dot{\gamma}$) and the relaxation time of the polymer (λ), i.e. the Weissenberg number ($Wi = \lambda\dot{\gamma}$). For $Wi > 1$ a polymer is deformed at a faster rate than it can relax and elastic effects arise.

Another useful dimensionless parameter for characterizing non-Newtonian flows is the elasticity number $El \approx Wi/\,\mathrm{Re}$, which quantifies the ratio of elastic to inertial forces in the flow. For Newtonian flows, $El \equiv 0$, instabilities that may arise in these flows are considered "purely inertial" since they depend only on Re. Instabilities that may arise in highly elastic fluids ($El \gg 1$) are considered "purely elastic", and may occur in negligible inertia for $Wi > 1$. There is increasing evidence that suggests that all these elastic instabilities are driven by accumulation of elastic stresses along curving streamlines [44, 140–142].

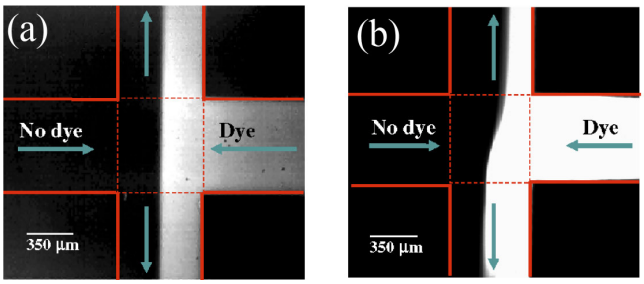

Figure 1.16: Purely elastic flow instability at a cross-slot junction. Dye advection patterns at Re $< 10^{-2}$ for (a) a Newtonian fluid, $Wi = 0$, and (b) a non-Newtonian fluid, $Wi = 4.5$ [144].

In the cross-slot device, purely-elastic instability appears as two-dimensional (2D) flow asymmetries, which can be steady or time dependent, depending on the particular fluid and geometric parameters [44, 77, 89, 143–148]. At higher Wi these purely elastic instabilities can develop into spatio-temporally disordered fluctuations described as "elastic turbulence" [149–152].

The onset of a "purely elastic" flow instability was previously demonstrated with asymmetric flow patterns in several studies [77, 144, 145]. A view of the center $x - y$ plane of the cross-slot is shown in Figure 1.16, which illustrates dye advection patterns at low Re $< 10^{-2}$ for Newtonian and non-Newtonian fluids. The interface between dyed and undyed fluid is deformed by an elastic instability [144]. The channel dimensions used for this study were of $w = 650$ μm and $d = 500$ μm with an aspect ratio $\alpha = 0.77$. In this work two novel flow instabilities of a planar extensional flow (of 0.02 wt.% solution of 18 MDa polyacrylamide (PAA) in 97 wt.% aqueous glycerol), were discovered. In the first instability, the flow became deformed and asymmetric but remained steady. Another instability occurred at higher strain rates, in which the velocity field fluctuated non-periodically in time. This purely-elastic instability in the cross slot did not exhibit hysteresis [145].

An additional mode of "purely elastic" instability was discovered by using an optimal configuration of the cross-slot geometry (the Optimized Shape Cross-slot Extensional Rheometer, OSCER). This instability appears at lower Wi than the onset of the asymmetric flow (shown in Fig. 1.16 b), and it is characterized by a lateral displacement and local unsteadiness of the stagnation point [44].

Investigation of "elastic turbulence" in the cross-slot flow (with highly elastic polymer solution) was also recently conducted, however in the parametric range studied, the flow could not be characterized as fully turbulent but it was described as chaotic [86].

1.3.3 Inertio-elastic instabilities

High elasticity numbers are characteristic of polymeric fluids with long relaxation times, i.e. those with viscous solvents, high molecular weights and relatively high concentrations, at small geometric length scales. However, for flows of highly dilute polymer solutions in low viscosity solvents in larger length scale flow configurations, typical of drag-reduced flows, inertia is not negligible ($0 < El \lesssim 1$) and the flow can be termed

"inertio-elastic" (or equivalently "elasto-inertial"). In this case there is a complex interaction and competition between inertial and elastic effects that remains to be fully described and understood.

The addition of high molecular weight polymers to a simple Newtonian fluid at even extremely low concentrations (parts-per-million) introduces a small but important degree of elasticity to the liquid, which can strongly influence macroscopic flow behavior. The effects of polymer additives are exploited for the reduction of drag in turbulent flows [43, 153–157], for enhancing the pressure drop in porous media flows [158] and for inhibiting jet breakup and the atomization of sprays [159, 160]. These effects are broadly understood in terms of the generation of localized anisotropic elastic stresses due to polymer stretching and orientation in specific regions of the flow field. However, detailed understanding of the mechanisms underlying the phenomena, such as how exactly polymer stretching feeds back on the flow field in order to suppress (or generate) instabilities, in many instances remains vague. Systems designed to model aspects of these flows, while avoiding their full complexity, can play an important role in filling the remaining knowledge gaps.

Only one study (1993) reported the increasing elastic effects in inertial cross-slot flow [161]. In this study, the effect of the polymer polyethyleneoxide (PEO) on the stability of planar flow was examined in high aspect ratio cross-slot devices with $\alpha = 32$ and $\alpha = 262$. In these devices, that were introduced in Section 1.1.2, Fig. 1.6, Newtonian fluid flows become unstable at $\mathrm{Re} = 55$ ($\alpha = 262$). It was found that increasing polymer concentrations reduced the critical Reynolds number in which the transition to unstable flow occurs. This effect reached a minimum at a concentration of 100 ppm where the critical Re drops to $\mathrm{Re}_c \simeq 20$ ($\alpha = 262$). Further increase in the polymer concentration led to an increase in Re_c.

1.3.4 Inertio-elastic turbulence

A fully turbulent inertio-elastic flow regime was also recognized in flows in a macroscale pipe, for which the transition to sustained turbulence occurred at $\mathrm{Re} \approx 2000$ in the Newtonian case. In this study it was shown that the increasing polymer concentration resulted in a delayed transition to turbulence, at higher Re [155]. However, in this study they observed a new type of turbulent fluctuation termed 'elasto-inertial turbulence' (EIT) due to the onset of an elastic instability driven by polymeric stresses (though for non-negligible inertia), for which the onset Re decreased significantly as the polymer concentration increased. As Re was increased beyond the onset of the instability, the measured friction factor directly approached the maximum drag-reduction (MDR) asymptote [153], without any excursion towards the 'Blasius' friction factor scaling expected for Newtonian turbulence. Furthermore, numerical simulations of the flow structures and dynamics showed that as the MDR asymptote was approached, streamwise-oriented vortices characteristic of Newtonian turbulence were suppressed.

In Chapter 6 it will be shown how a slight addition of polymers to Newtonian solvents affects the stability of a stagnation point flow in the cross-slot geometry. We will study the different components of the flow transition including symmetry breaking, vortex merging, formation and properties of a single streamwise vortex in inertio-elastic flows. As discussed in Section 1.1.2, streamwise vortices such as the one seen in the

cross-slot geometry are important elements of turbulent flows. By isolating certain components of flows (e.g. isolating a single vortex from a turbulent flow) we can avoid their full complexity and by so, it is possible to understand the very fundamentals of flow responses and transitions. Similar approach has been previously used to study porous media with a single sphere or a pole [162–165] and by using jet or spray breakup to approximate capillary thinning or drop pinch-off phenomena [166–169].

Chapter 2

Methods

2.1 Fabrication of microfluidic devices

In this thesis, a recent fabrication technique of microfluidic channels, based on selective laser-induced etching (SLE) is used [170]. SLE is a new subtractive 3D printing technique enabling microfabrication in transparent substrates, such as fused silica glass (SiO_2) [170]. The technique permits the fabrication of 3D structures that are fully embedded in a high modulus (≈ 75 GPa), highly transparent (optical transmission $> 90\%$ over the whole of the visible range) material with a resolution $\sim O\ 1\mu$m.

Although fabrication by soft lithography of microfluidic channels in poly-(dimethyl siloxane) (PDMS) is the most common method for producing microfluidic devices (relatively cheap, easy and rapid) there are many disadvantages when using PDMS channels for inertial flow studies that led us to choose fabrication in fused silica glass with SLE. Studying inertial flows requires high flow rates, yet applying high pressure in PDMS channels leads to channel deformation, non-uniform channel dimensions and may also cause leakage of fluid through the inlet and/or outlet connection points, all can be easily avoided with fused silica glass channels.

Additionally, collapse of PDMS channels is common due to the softness of the material, limiting the fabrication possibilities to channels with aspect ratio ~ 1. On the contrary, the stiff material used in SLE enables the fabrication of very slim structures and channels with very high or very low aspect ratios.

The softness of the PDMS material also makes it difficult to clean since fluorescent dyes and tracer particles may get trapped in the material and organic solvents may react with it. Therefore, it is not possible to perform a series of experiments with a single device, and multiple devices which are not perfectly identical will be required (even if fabricated from the same mold). Yet, fused silica glass can be washed vigorously with organic solvents and it is possible to remove blockages by applying high pressures, therefore it can be re-used unlimited amount of times.

Furthermore, the optical properties of PDMS devices are poor, and viewing the channel is restricted to the side of the glass cover slide. In contrast, fused silica glass devices have a good optical transparency and can be observed from different planes.

Apart from SLE we also considered fabrication with other techniques such as laser cutting [171], wire electrical discharge machining (wire-EDM) [172], micromilling [173], reactive ion etching or chemical etching in silicon or glass [174]. Although these ap-

proaches offer some solutions to the problems with PDMS, none of them provide a solution to the 3D fabrication limitations; most are restricted to rather low aspect ratio devices, and most have optical access limited to only one plane.

Microfluidic cross-slot devices

Fabrication of cross-slot devices with PDMS, allows to directly visualize the stagnation point region only from the $x-y$ plane. Visualization of the vortex formation across the $y-z$ plane can therefore only be done with non-direct methods such as imaging of dye advection pattern with scanning confocal microscopy, as was previously done [27, 63]. From dye advection measurements it is possible to obtain qualitative information of the flow structures and to quantify mixing efficiency.

The main limitations of experiments with dye advection patterns are: (1) it is not possible to resolve flow patterns which are not at the interface between dyed and undyed fluid streams. For example, the Dean vortices in Fig. 1.7 c, that are formed while the flow is still symmetric are not visible (Fig. 1.8 a); (2) it is not possible to perform detailed dynamic studies due to long scanning times of the confocal microscopy; (3) dye advection experiments do not provide any quantitative information on the flow, and therefore it is difficult to compare experiments with numerical simulations [3, 4, 27].

For these reasons, SLE provides the ideal solution for device fabrication that enables to directly image and perform dynamic measurements by vertically mounting the cross-slot on an inverted microscope, giving direct access to the $y-z$ plane.

2.1.1 The selective laser induced etching technique

The SLE method is a two-step process including laser modification and chemical etching of the substrate. A femtosecond laser is used to irradiate a selected volume of material, thereby increasing the chemical etch rate of specific regions within the glass substrate by up to 1000 times compared with the unirradiated material. To produce the SLE structures we use the commercially available LightFab 3D printer (LightFab GmbH), which uses a 4 W, $\lambda = 1030$ nm, femtosecond-pulsed laser, with a 2.6 μm (x, y) by 6 μm (z) spot size [175].

The SLE process begins with the preparation of a 3D computer-aided design (CAD) model (Fig. 2.1 a) of the portion of the substrate that will be removed during fabrication. The 3D model is sliced to create the programmed laser paths that the LightFab scanner will use to modify the fused silica volume during the printing process (Fig. 2.1 b).

Great care is taken in optimizing the slicing and filling of the volume: if the programmed laser paths are too dense, overlap frequently or form too many sharp corners, cracking of the substrate will occur during the laser modification or wet etching steps. Creating the laser paths for an SLE structure is a compromise between achieving the most accurate representation of a desired 3D model and fabricating a structure without failure.

Owing to the compromise between densely and minimally filled SLE structures, an appropriate slicing and filling scheme needs to be chosen. Often an internal cubing scheme is chosen (Fig. 2.1 b) to break up the internal volume of material into smaller

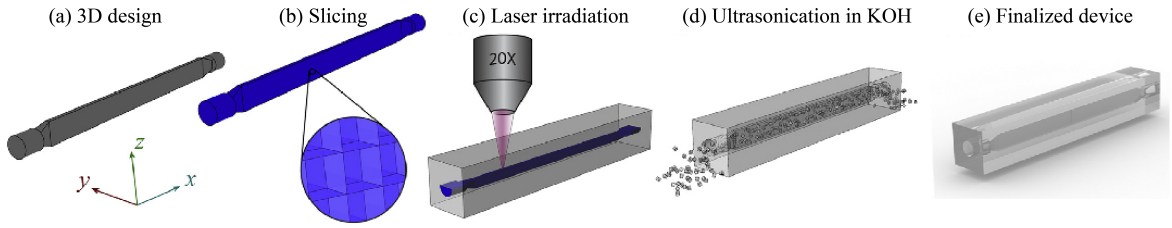

Figure 2.1: Fabrication of micro-channels by selective laser-induced etching [2]: (a) The inner volume of a desired microfluidic channel is created using 3D CAD software. (b) The 3D model is then sliced and filled to create a z-stack of lines used to define individual laser paths. (c) A femtosecond laser irradiates a polished fused silica substrate following the specified slices. (d) The laser-irradiated material is preferentially etched by KOH (assisted by ultrasonication at 85°C), and the inner volume of the microfluidic channel is removed. (e) The finished monolithic glass microfluidic device.

volumes that can be easily removed through the narrow inlet and outlet regions during the subsequent ultrasonic wet etching step. Once the programmed laser path file and a polished fused silica substrate are loaded into the LightFab, laser modification is performed (Fig. 2.1 c).

The laser-modified fused silica substrate is then placed in an 85°C KOH ultrasonic bath to perform the chemical etching (Fig. 2.1 d). The laser-modified regions of the fused silica etch at a rate of between 50 and 100 μm hr $^{-1}$ (compared with 0.1 $\approx$ μm hr $^{-1}$ for the unmodified regions), allowing the removal of specified regions within the material. After etching is complete, the device is rinsed with deionized water and is ready for use (Fig. 2.1 e).

2.1.2 Microfluidic cross-slot devices - experimental set up

For this thesis, several cross-slot intersections have been fabricated using SLE. The devices are fabricated with different aspect ratios ($\alpha = d/w$) that are selected in order to span a range of subcritical (hysteretic, $\alpha \gtrsim 0.55$) and supercritical (smooth, $\alpha \lesssim 0.55$) transitions [27] (Fig. 2.2). Detailed specifications of the devices can be found in Table 2.1. The error in the measurement of α is estimated to be $\pm$ 1%.

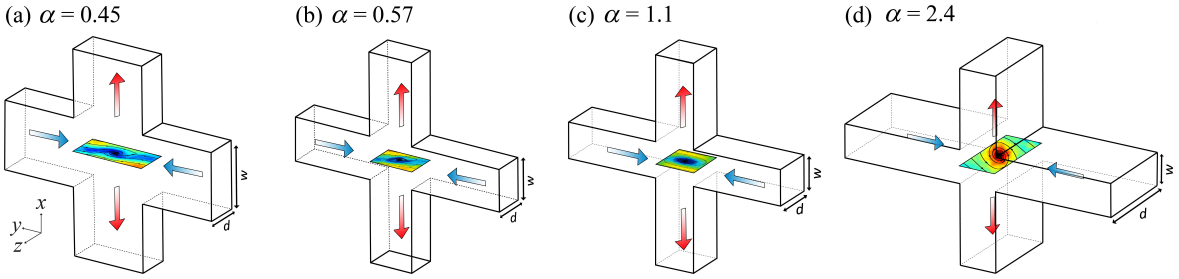

Figure 2.2: Schematic illustration of the cross-slot devices used for studying flow instability and vortex dynamics at the proximity of a tricritical point. (a) $\alpha = 0.45$ superitical transition; (b) $\alpha = 0.57$ near tricritical transition; (c) $\alpha = 1.1$ subcritical transition; (d) $\alpha = 2.4$ subcritical transition.

Table 2.1: Microfluidic cross-slot devices specifications

α	w	d	Transition type	Re_c	Re_c^*	Used in chapter
0.45	1490	670	supercritical	107.5	107.5	4 & 5
0.57	1460	830	near tricritical	76.0	75.0	4
1.1	990	1060	subcritical	40.2	36.5	4
2.4	620	1500	subcritical	26.5	21.4	4 & 5
1.0	430	430	subcritical	40.0	38.8	6

The inlet lengths of the cross-slot devices are set to be either 13 mm or 16 mm, giving a high ratio (> 10) between the inlet length and the larger channel dimension ensuring fully developed flow before the fluid reaches the center of the cross-slot geometry. The outlets are designed to be as long as possible (≈ 5 mm), while still allowing imaging to be performed in the $y - z$ centerplane (at $x = 0$) with a long working distance microscope objective (see Fig. 2.3 a). In this manner, it is possible to directly visualize the stagnation point at the $y - z$ centerplane and perform dynamic experiments (see Fig. 2.3 b). A picture of the microfluidic device with tubing connections mounted on an inverted microscope is shown in Fig. 2.3 c.

Flow within the glass microfluidic device is driven using four individually-controlled high precision neMESYS syringe pumps (Cetoni GmbH, Germany) fitted with Hamilton Gastight syringes and operating at a minimum of 10× (and typically $> 50\times$) the specified lowest "pulsation-free" dosing rate. Two of the pumps drive fluid into the two opposed inlets, while the other two pumps withdraw fluid simultaneously from the two outlets of the device (all at an equal volumetric flow rate Q). In order to keep the system compliance at a minimum, the tubing between the syringes and the device is made of rigid PTFE (polytetrafluoroethylene), and is kept as short as possible, and great care is taken to purge all air from the system.

All of the experiments involve the flow of deionized water with a kinematic viscosity

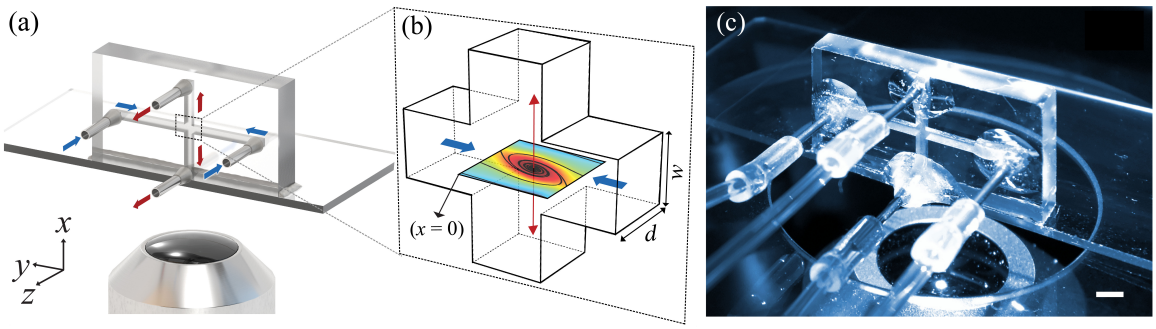

Figure 2.3: Experimental set up of the microfluidic cross-slot device; (a) A schematic diagram of the experimental setup; (b) Schematic diagram of a vortex in the cross-slot device. Inflow (along y) and outflow (along x) are indicated by the blue and red arrows, respectively; (c) A picture of the experimental set-up, showing the microfluidic cross-slot device mounted on a microscope.

$\nu = 8.9 \times 10^{-7}$ m^2 s^{-1} at 25°C. All experiments are carried out at 25 ± 1°C, and the estimated error in Re is around ±1%.

2.2 Flow field measurement with the Differential Spinning Disk confocal microscope

Flow structures formed by dye-advection patterns in the cross-slot geometry are achieved by introducing a solution containing the fluorescent dye rhodamine B (10 μM) through one inlet while an undyed solution is introduced through the other inlet. The microfluidic device is mounted on the stage of an inverted microscope (Nikon Eclipse Ti), and the $y - z$ plane is brought into focus using a long working distance lens (Nikon Plan Fluor) with magnification of 10×, numerical aperture (NA) = 0.3, working distance (WD) = 16 mm. With the use of a differential spinning disk confocal microscope system (DSD2 - Andor Technology Ltd, Belfast, UK) it is possible to focus on a single plane (the $y - z$ plane) while the light emitted from out of focus planes is filtered. The spinning disk confocal microscopy utilizes multiple pinholes that are located between the objective lens and the camera, in order to project light onto the channel in a multiplexed pattern that is detected after fluorescence emission passes through the same pinholes. The signal is then detected with an Andor Zyla scientific complementary metal-oxide-semiconductor (CMOS) camera at a resolution of 0.1 μm per pixel. The maximal frame rate of the camera is 10 fps and a green fluorescent light source is used for illumination.

2.3 Micro Particle Imaging Velocimetry (μ-PIV)

2.3.1 μ-PIV working principles

Particle imaging velocimetry (PIV), is one of the most common technique for measuring instantaneous velocity fields, without interfering the flow. With the PIV technique, the plane of measurement is defined by a laser light sheet that continuously irradiate tracer particles that are added to the fluid. μ-PIV systems have similar principle of operation, with a difference in the type of illumination. Due to the small length scales of microfluidics, it is very difficult to align a laser sheet within the channel and therefore volume illumination is used. When using volume illumination, the recording optics (i.e., camera, lens) defines the depth of the measurement plane. To achieve the optimal signal-to-noise ratio that may be disrupted by unfocused particles in the different illuminated planes, it is important to carefully choose the lens and tune the concentration of the tracer particles in the sample [176, 177].

A scheme of a μ-PIV system is shown in Fig. 2.4. The dual pulse laser passes through the inverted microscope and the optic lens illuminates the area of interest in the microfluidic device. A high speed camera captures the frames simultaneously with the illumination of the dual pulse laser. In order to represent correctly the flow field, the separation between the dual pulses of the laser light should be smaller than the time scales of the flow. The exact synchronized operation of the laser and the camera

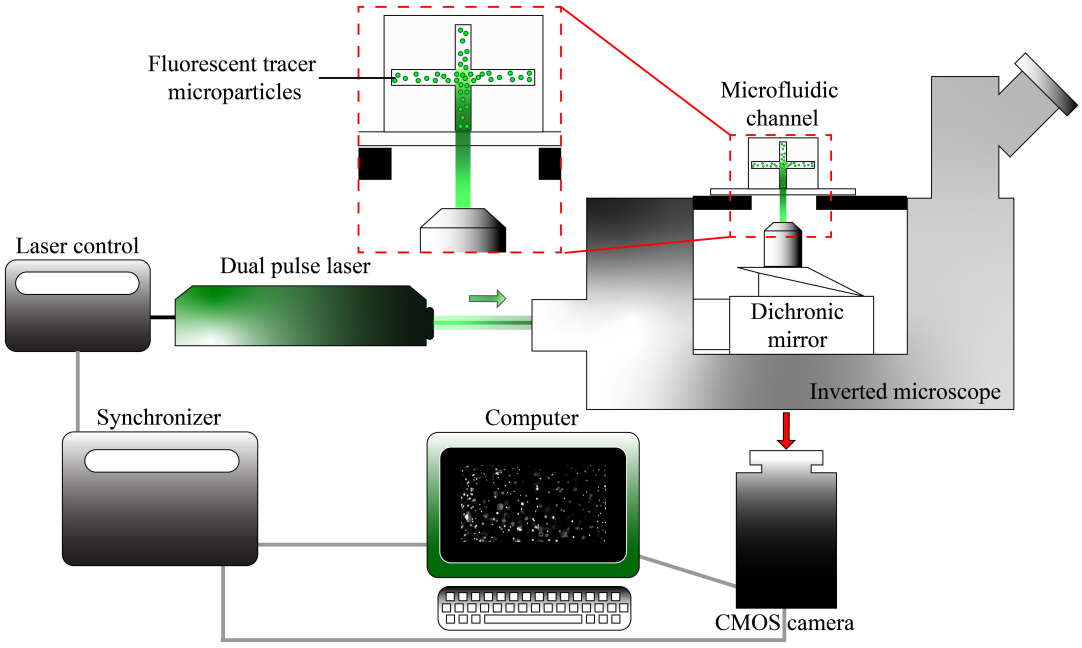

Figure 2.4: μ-PIV system, for flow field measurement. The main parts of the system consists of a dual-pulsed laser, a high speed CMOS camera, an inverted microscope and a synchronizer.

is determined with a synchronizer system. Dual frames of the flow field are illustrated in Fig. 2.5 a & b. The flow field is divided to smaller interrogation areas and the displacement of the particles between one frame to the other is analyzed with a cross-correlation algorithm (Fig. 2.5 c). For each one of the interrogation areas determined, the algorithm produces a vector that is placed in the center of the interrogation area providing a full vector representation of the flow field (Fig. 2.5 d).

2.3.2 Flow field measurements with μ-PIV

Quantitative measurements of the flow field are made in the $y-z$ center plane ($x = 0$ plane) of the cross-slot device (Fig. 2.3 b) using a microparticle image velocimetry (μ-PIV) system (TSI Inc., MN) [176, 178]. The microfluidic device is mounted on the stage of an inverted microscope (Nikon Eclipse Ti), and the $x = 0$ plane is brought into focus. Details about the tracer particles, lens and resulting measurement depth are listed below:

1. For experiments where the channel's characteristic length scale $w < 500$ μm:

   Test fluids are seeded with fluorescent particles (PS-FluoRed, MicroParticles GmbH, Germany) of diameter $d_p = 2.08$ μm with excitation and emission wavelengths of 530 and 607 nm, respectively. A long working distance lens Nikon Plan Fluor is used, with magnification of 10×, NA = 0.3, WD = 16 mm. With this combination of particle size and objective lens, the measurement depth over which particles contribute to the determination of the velocity field is $\delta x_m \approx 40$ μm ($\delta x_m < 0.1$ w) [176]. Image pairs are binned into interrogation areas of 32

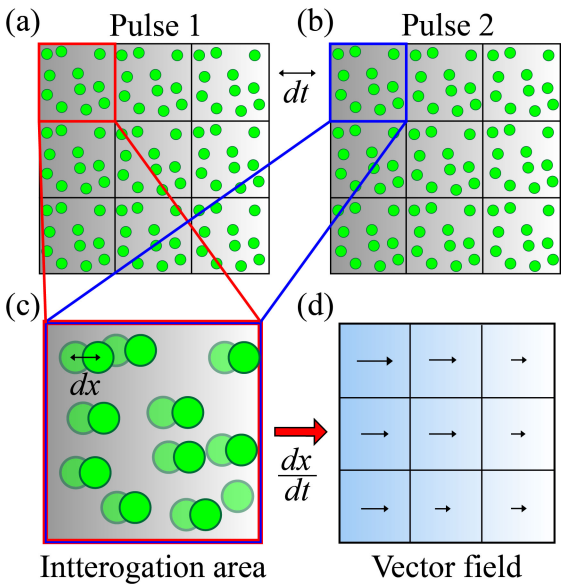

Figure 2.5: Creating a velocity vector field with the cross-correlation algorithm. The camera captures two images synchronized with the illumination of the dual pulse laser (a) image from pulse 1 and; (b) image from pulse 2; (c) the flow field is divided into interrogation areas, in each area the displacement of each particle is measured between the pulses; (d) the displacement of particles and the time separation between pulses are used to resolve the velocity vector field of the flow at each interrogation area. For simplification only dx is indicated yet there is also a displacement in the y direction that is accounted for in real measurements.

$\times$ 32 pixels and cross-correlated using a standard μ-PIV algorithm (TSI Inc.) to obtain velocity vectors spaced on a square grid of 12.8 $\times$ 12.8 μm in y and z.

2. For experiments where the channel's characteristic length scale $w > 500$ μm:

   Test fluids are seeded with fluorescent particles (PS-FluoRed, MicroParticles GmbH, Germany) with diameter of $d_p = 5.0$ μm with excitation and emission wavelengths of 530 nm and 607 nm, respectively. A long working distance lens Nikon Plan Fluor is used, with magnification of 4$\times$, NA = 0.13 and WD = 16 mm. With this combination of particle size and objective lens, the measurement depth over which particles contribute to the determination of the velocity field is $\delta x_m \approx$ 210 μm ($\delta x_m < 0.33\ w$) [176]. Image pairs are binned into interrogation areas of 64 $\times$ 64 pixels and cross-correlated using a standard μ-PIV algorithm (TSI Inc.) to obtain velocity vectors spaced on a square grid of 32 $\times$ 32 μm in y and z.

The μ-PIV system is equipped with a 1280 $\times$ 800 pixel high-speed CMOS camera (Phantom MIRO), which operates in frame-straddling mode and is synchronized with a dual-pulsed Nd:YLF laser light source with a wavelength of 527 nm (Terra PIV, Continuum Inc., CA). The laser illuminates the fluid with pulses of duration $\delta t < 10$ ns, thus exciting the fluorescent particles, which emit at a longer wavelength. Reflected laser light is filtered out by a G-2A epifluorescent filter so that only the light emitted by the fluorescing particles is detected by the CMOS imaging sensor array. Images are

captured in pairs (one image for each laser pulse), where the time between pulses Δt is set by the instrument operator such that the average particle displacement between the two images in each pair is around 4 pixels. The typical error on individual velocity vector components is around $\pm$ 0.05 U, where $U = Q/wd$ is the average flow velocity in the channel.

2.4 Experimental protocols

2.4.1 Quasistatic flow measurements

Initially, in order to identify the approximate value of Re_c for each experimental system, several images are captured for fixed Re applied below and above the transition. Next, more detailed quasistatic experiments are conducted over a range of Reynolds numbers spanning $\mathrm{Re} < \mathrm{Re}_c$ to $\mathrm{Re} > \mathrm{Re}_c$ by programming the syringe pumps to perform ramps up and down in Re with small step increases or decreases of $0.1 \leq \mathrm{Re} \leq 2$, depending on the precise system under study. Performing experiments with decreasing time steps allows to reveal if the transition is smooth or abrupt (i.e. if there is hysteresis in the transition). If the flow turns back to symmetric at $\mathrm{Re}_c^* = \mathrm{Re}_c$, there is no hysteresis in the flow. If the flow turns back to symmetric at $\mathrm{Re}_c^* < \mathrm{Re}_c$ than the transition is defined as hysteretic.

Typically 5 s of steady flow is imposed at each increment in Re. Note that this is significantly longer than the diffusion time scale of the least viscous sample (water) tested in the device with the largest length scale ($\alpha = 0.45$, $w = 1490$ μm), which is given by $t_d = (w/2)^2/\nu \approx 0.56$ s. Dynamic experiments carried out to track the startup of flow at $\mathrm{Re} > \mathrm{Re}_c$, indicate that steady-state conditions are achieved for the flow of water within approximately 0.5 s, as expected.

Images pairs are captured at a rate of 5 Hz using the μ-PIV system, typically yielding 25 velocity vector fields per step in Re. Avoiding data captured during the transient at the start of each Re step, velocity fields from each step are averaged using the software Tecplot Focus (Tecplot Inc., WA) and further processed to obtain streamline projections on the $x = 0$ plane and the x-component of the vorticity $\omega_x = (\partial v_z/\partial y) - (\partial v_y/\partial z)$, where v_z and v_y are the z and y components of the local flow velocity vectors, respectively.

It is worthwhile to mention that for each test fluid the range of Re we can examine in this way is restricted fundamentally by limitations of the μ-PIV system, which does not allow the value of Δt to be varied during a given experiment. Given a fixed Δt, if the flow velocity (or Re) during an experiment becomes too low, particles are displaced insufficiently in the time between laser pulses to obtain reliable vectors. Conversely, if the flow velocity becomes too high then too many particles can become displaced into neighboring interrogation areas between laser pulses and the cross-correlation algorithm again fails to resolve vectors. Ideally, for optimal function of the algorithm, the average particle displacement between laser pulses should be around 1/8 of an interrogation area (maximum 1/4 of an interrogation area). In our experiment Δt must therefore be carefully selected in order that velocity fields can be resolved reliably over a range of flow rates that spans the onset of the flow instability.

2.4.2 Dynamic flow measurements

Time dependent flow measurements are conducted to capture the dynamics of the transition, in the proximity of Re_c, from stable symmetric flow to unstable asymmetric flow, and from unstable asymmetric flow to stable symmetric flow. Once the flow transition is completed, the flow is at a steady state (e.g., unstable flows). Additional dynamic measurement are conducted for time dependent flows at Re well beyond Re_c, in these cases the flow does not reach a steady state (e.g., unsteady flows).

Measurement of unstable flow

Based on the values of Re_c and Re_c^* found in the quasistatic experiments, time dependent measurements are conducted. The transition from symmetric to asymmetric flow field is studied by inducing a single step in Re from an initial Re below the critical value ($\mathrm{Re}_i < \mathrm{Re}_c^*$) to a final Re above the critical value ($\mathrm{Re}_f > \mathrm{Re}_c^*$). Similarly, the opposite experiments are conducted with a single step in Re, from $\mathrm{Re}_i > \mathrm{Re}_c$ to a final value $\mathrm{Re}_f < \mathrm{Re}_c$. For each α, several measurements are performed for various values of Re_f while Re_i is held constant. Data acquisition starts before flow is imposed. The Reynolds number is increased from 0 to Re_i and held steady for 5 seconds. Subsequently we increase or decrease Re from Re_i to Re_f and again the flow is kept steady for 5 s. In this way, the moment during acquisition where the second step begins, which defines the time $t = 0$, can be easily determined. Image pairs are captured at 100 Hz and are processed individually to obtain 100 velocity fields per second. This is found to be more than sufficient to capture the detailed dynamics of the flow transition. Velocity fields from each experiment are processed using the software Tecplot Focus (Tecplot Inc., WA) to obtain streamline projections on the $x = 0$ plane. Further data analysis of the vector field is done with Matlab.

Measurement of unsteady flows

In these experiments, we set $\mathrm{Re} \gg \mathrm{Re}_c$ to study time dependent flow for two extreme cases of vortex spatial confinement in the cross-slot geometry: high spatial confinement with $\alpha = 0.45$ (see Fig. 2.2 a) and moderate spatial confinement with $\alpha = 2.4$ (see Fig. 2.2 d). The Re is set using a the syringe pumps to a constant value and kept steady for 5 s. Then, image pairs are captured at a high frequency of 500 - 1000 Hz in order to capture the time dependent periodic cycles in the flow. For each Re studied, 100 velocity vector fields are produced. Vector fields from each experiment are used to calculate velocity and vorticity contours using Matlab.

2.5 Rheology of non-Newtonian fluids

2.5.1 Materials

The effects of increasing elasticity on the onset and development of flow instability and vortex formation in the cross-slot device, are studied using solutions of a high molecular weight poly(ethyleneoxide) (PEO, $M_w = 4$ MDa, Sigma Aldrich) over a

range of concentrations $0.0001 \leq c \leq 0.3$ wt% (i.e. $1 \leq c \leq 3000$ parts-per-million by weight). Solutions are prepared in two different solvents: de-ionized (DI) water and an aqueous solution of 8 wt% of a low molecular weight poly(ethyleneglycol) (PEG, $M_w = 8$ kDa, Sigma Aldrich). At this molecular weight, 8 wt% aqueous PEG behaves as a Newtonian fluid with its shear viscosity approximately four times greater than water [179]. Stock PEO solutions are prepared by dispersing a weighed quantity of the polymer powder in the appropriate quantity of solvent. To assist dissolution while avoiding mechanical degradation of the PEO, only low speed (30 rpm) magnetic stirring is applied. Dissolution is allowed to proceed until no refractive index variations or residual gels are visible in the fluid (typically 24 to 48 hrs). The fluids are stored at 4°C and are used within a maximum of 4 weeks. Solutions with lower concentration of polymers are prepared by dilution of the stock fluids in the appropriate quantity of solvent.

2.5.2 Test fluid characterization

Shear rheology for viscosity measurements

Steady flow curves of shear viscosity η as a function of the imposed shear rate $\dot{\gamma}$ are measured for the polymer solutions and the solvents using a stress controlled rotational rheometer (Anton Paar, MCR 502) with a 50 mm diameter 1° cone-and-plate fixture. The results are presented in Fig. 2.6. Most of the fluids are essentially non-shear-thinning over the imposed range of shear rates, however for the two highest concentrations of PEO in water a mild reduction in viscosity is observed as the shear rate increases.

To estimate the viscosity of these shear-thinning fluids at arbitrary shear rates

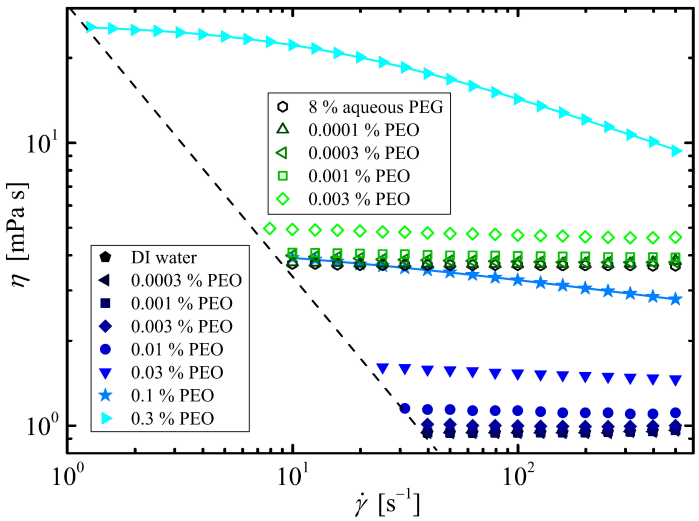

Figure 2.6: Shear viscosity measurements with a stress-controlled rotational rheometer (Anton Paar MCR 502) for PEO solutions of various concentrations in two different solvents: water and 8 wt% aqueous PEG. Curve fitting for the shear thinning fluids is done with the Carreau-Yasuda GNF model (Eq. 2.1). The diagonal dashed line represents 10× the minimum sensitivity of the rheometer [3].

Table 2.2: Parameters extracted by fitting the Carreau-Yasuda GNF model (Eq. 2.1) to the steady flow curves of the shear-thinning solutions of PEO dissolved in water.

c [wt%]	η_0 [mPa s]	η_∞ [mPa s]	$\dot{\gamma}^*$ [s^{-1}]	n	a^*
0.1	3.9	1	22.7	0.83	1
0.3	25	1	12.1	0.71	1

imposed within the microfluidic channel, the shear-thinning flow curves are fitted with a Carreau-Yasuda generalized Newtonian fluid (GNF) model [180]:

$$\eta = \eta_\infty + \frac{\eta_0 - \eta_\infty}{[1 + (\dot{\gamma}/\dot{\gamma}^*)^{a^*}]^{(1-n)/a^*}}, \tag{2.1}$$

where η_0 and η_∞ are the zero and infinite shear rate viscosities, $\dot{\gamma}^*$ is the characteristic shear rate for the onset of shear-thinning, n is the power law index in the shear-thinning region and a^* is a parameter that controls the sharpness of the transition to the power-law regime. The values of these parameters for the two shear-thinning fluids are provided in Table 2.

Extensional rheology for relaxation time measurements

As far as possible, the relaxation times λ, of the test fluids, are measured using capillary breakup extensional rheometry, (CaBER, Thermo Scientific). Measurements with this device are performed as follows: a fluid is placed between two plates that rapidly separate from each other, causing elongation of the solution until the thread of stretched fluid breaks. A laser micrometer measures the diameter of the fluid thread at the center point between the two plates. The rate of the thinning can then be used to calculate the relaxation time of a fluid [167, 181, 182]. For many of the more dilute PEO solutions, the relaxation times are too low to be measured accurately using the standard CaBER technique and therefore the more sensitive slow retraction method (SRM) is employed (Fig. 2.7) [183]. In this method, the drop of fluid is placed between two plates (Fig. 2.7 a) but the detachment rate is slower (Fig. 2.7 b). The measurement

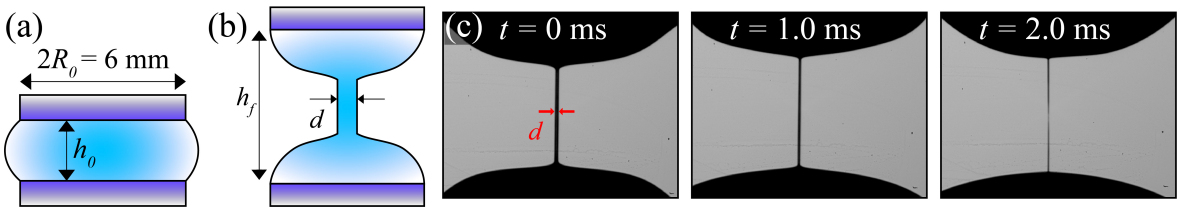

Figure 2.7: Demonstration of an SRM measurement performed using a CaBER device (a) A droplet of the test fluid is placed between two plates with separation of h_0. (b) The plates are then separated at a rate of 0.1 mm s^{-1} while imaging is being performed. (c) Image sequence of the thinning filament for PEO solution of 0.0003 wt% PEO in 8 wt% PEG dissolved in water. Images are taken at 18,000 fps with a high speed Phantom camera.

of the diameter of the fluid thread is done with a high speed camera and calculated with a Matlab code (Fig. 2.7 c). Two of the fluids (0.001 wt% PEO in water and 0.0003 wt% PEO in PEG) are measured using both techniques (CaBER and SRM) and we obtain good agreement.

Zimm relaxation time

The Zimm relaxation time (λ_{Zimm}) is used to estimate the relaxation time for very dilute solutions which cannot be measured by CaBER or SRM. For the lowest concentration (0.0003 wt%) PEO in water, λ could not be reliably measured even by SRM and therefore we estimate the relaxation time of this fluid using the Zimm formula:

$$\lambda_{\text{Zimm}} = F^* \frac{[\eta] M_w \eta_s}{N_A k_B T}, \tag{2.2}$$

where $M_w = 4\times10^6$ g mol^{-1} is the PEO molecular weight, N_A is the Avogadro constant, k_B is the Boltzmann constant, T is the absolute temperature, $\eta_s = 0.94$ mPa s is the measured solvent viscosity, and the front factor $F^* = 0.463$ [184]. The intrinsic viscosity $[\eta] = 1.323$ m^3 kg^{-1} is calculated according to the Mark-Houwink-Sakurada correlation [185]. According to this calculation the longest relaxation time of the 4MDa PEO molecule in water is $\lambda_{Zimm} \approx 1$ ms.

The characteristic relaxation times of all the test fluids are summarized in Table 2.3. We note that the values of $1/\dot{\gamma}^*$ obtained from the Carreau-Yasuda fit to the steady shear rheology of the two fluids shown in Table 2.2 are consistent with the values of λ obtained from the CaBER measurements on the same two fluids. Table 2.3 also

Table 2.3: Composition and material parameters of the experimental test fluids at 25°C.

solvent	c [wt%]	c/c^*	η_0 [mPa s]	λ [ms]	$\beta = \eta_s/\eta_0$	El
water	0.0003	0.007	0.95 ± 0.01	1.0[1]	0.99 ± 0.01	$(5 \pm 5) \times 10^{-5}$
$\eta_s = (0.94 \pm 0.01)$ mPa s	0.001	0.02	0.95 ± 0.01	3.6 ± 0.3[2]	0.99 ± 0.01	$(1.8 \pm 1.8) \times 10^{-4}$
$\rho = 997$ kg m^{-3}	0.003	0.07	1.02 ± 0.01	5.0 ± 0.4[2]	0.92 ± 0.01	$(2.1 \pm 0.3) \times 10^{-3}$
$\beta = 1$	0.01	0.22	1.12 ± 0.02	12 ± 1[3]	0.84 ± 0.02	$(1.1 \pm 0.2) \times 10^{-2}$
	0.03	0.66	1.59 ± 0.02	23 ± 1	0.59 ± 0.01	$(7.8 \pm 0.4) \times 10^{-2}$
	0.1	2.2	3.90 ± 0.05	44 ± 2	0.24 ± 0.00	0.68 ± 0.03[4]
	0.3	6.6	25.0 ± 0.1	84 ± 4	0.04 ± 0.00	10.4 ± 0.5[4]
8 wt% PEG	0.0001	0.002	3.81 ± 0.02	2.2 ± 0.3[2]	0.97 ± 0.01	$(8.3 \pm 0.4) \times 10^{-3}$
$\eta_s = (3.71 \pm 0.01)$ mPa s	0.0003	0.007	3.92 ± 0.05	12 ± 1[3]	0.95 ± 0.01	$(1.2 \pm 0.5) \times 10^{-2}$
$\rho = 1011$ kg m^{-3}	0.001	0.02	4.07 ± 0.02	28 ± 1	0.91 ± 0.01	$(5.2 \pm 0.6) \times 10^{-2}$
$\beta = 1$	0.003	0.07	4.90 ± 0.04	57 ± 2	0.76 ± 0.01	0.34 ± 0.03

[1] relaxation time estimated from the Zimm formula (Eq. 1.2).

[2] relaxation time measured using the slow retration method (SRM) implemented on a capillary breakup extensional rheometer (CaBER).

[3] relaxation time measured using both standard CaBER and SRM techniques.

[4] representative El for the fluid calculated based on the zero-shear viscosity η_0.

shows the measured zero shear viscosities of all the test fluids and the "solvent-to-total viscosity ratio" $\beta = \eta_s/\eta_0$, where $\eta_0 = \eta_s + \eta_p$ and η_p is the polymer contribution to the viscosity. With these values we can calculate the Weissenberg number $Wi = \lambda\dot{\gamma}$. In order to account for the polymer contribution to the Wi we can calculate the effective Wi, $Wi_{\text{eff}} = Wi(1-\beta)$. Additionally, we can find the elasticity of the fluid $El = Wi_{\text{eff}}/\text{ Re} = (1-\beta)(\lambda\eta/\rho w^2)$ (see Table 2.3).

It is apparent from Fig. 2.6 and Table 2.3 that by using the more viscous aqueous solvent containing 8 wt% PEG, we are able to increase the relaxation time of the fluid while maintaining the viscosity ratio close to 1 and avoiding significant shear-thinning effects, which occur for higher concentrations of PEO in water.

Overlap concentration

Also shown in Table 2.3 is the ratio of the polymer concentration c to the overlap concentration c^*. The overlap concentration for PEO in the aqueous-based solvents used here is estimated based on space filling of polymer coils with a radius of gyration R_g [186]:

$$c^* = \frac{3M_w}{4N_A\pi R_g^3}, \tag{2.3}$$

where the value of $R_g = 152$ nm is estimated according to previous results of light scattering experiments [187]. Equation 2.3 provides a value of $c^* \approx 0.045$ wt%.

The equilibrium root-mean-square end-to-end separation of the PEO molecule is given by $< {r_0}^2 >^{1/2} = \sqrt{6}R_g = 372$ nm. The contour length may be estimated by $L_c = lM_w/m = 26.5$ μm, where $l = 0.278$ nm and $m = 42$ Da are the length and mass of the PEO repeat unit, respectively [188]. The ratio $L = L_c/< {r_0}^2 >^{1/2} \approx 71$ indicates the highly extendible nature of this high molecular weight PEO sample. This estimate of L is used to compute an appropriate extensibility parameter ($L^2 = 5000$) used for subsequent numerical simulations using a finitely extensible non-linear elastic (FENE) dumbell model, see Appendix A.

Chapter 3

The Landau model

In many physical systems, phase transitions or bifurcations, occur when a system is disturbed out of its equilibrium (or symmetry) due to external fluctuations, resulting in a new stable state. The physical parameters of a system will determine the nature of the transition. Bifurcations may also appear in fluid flows when a flow transitions from one regime to another, usually including loss of symmetry [189]. In certain phase transitions, there is a point on the phase diagram in which the transition type transforms from a continuous to discontinuous state, such a point is defined in the literature as a tricritical point [190].

A sixth order polynomial Landau type model is particularly useful in capturing the complexity of transitions near tricritical points [191]. Traditionally, the Landau model has been used for the description of thermodynamic related transitions (i.e. phase transitions in liquid crystals [192], melting of graphite [193] and solidification of iron [194, 195]). However, it can also be used to describe flow transitions, such as the secondary instability in the Taylor-Couette apparatus [49, 50] and the flow instability in the cross-slot geometry [27]. The Landau model does not explain the mechanisms behind a physical phenomenon but, as will be shown in this thesis, it can provide information on some physical parameters in the system. For example, with the Landau model we can precisely determine the critical Re, account for imperfections in the experiments and find the extent of memory (hysteresis) of a system.

When using the Landau model we first need to identify the base state of a certain physical system with a measurable parameter such as temperature or velocity that indicates changes in the system (i.e. an order parameter, ψ). By changing the control parameter, ε, the system is perturbed out of its equilibrium and will undergo a phase transition.

According to the Landau theory, these bifurcations occur due to a change in the "free energy" of the system, which can be described with a sixth order polynomial potential, F:

$$F = -\frac{1}{2}\varepsilon\psi^2 + \frac{1}{4}g\psi^4 + \frac{1}{6}k\psi^6 - h\psi. \tag{3.1}$$

The value of $\psi(\varepsilon)$ corresponds to the extrema of F, where $\dfrac{\partial F}{\partial \psi} = 0$:

$$-\varepsilon\psi + g\psi^3 + k\psi^5 - h = 0. \tag{3.2}$$

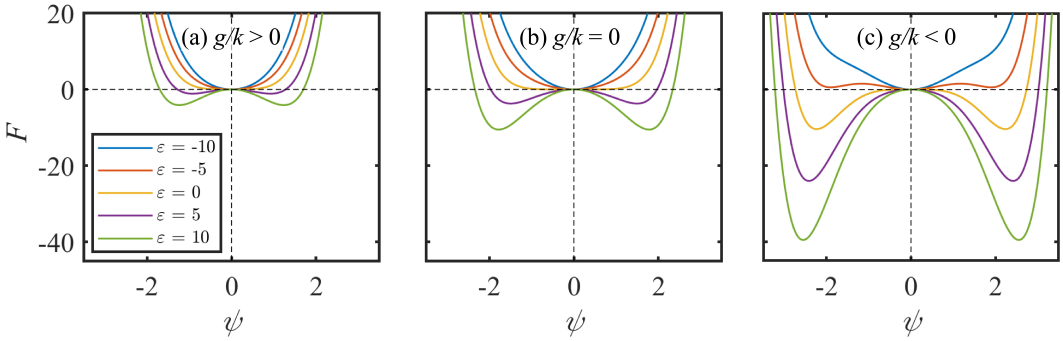

Figure 3.1: Landau potential in the form of sixth order polynomial in a perfect system $h = 0$. ε is varied above and below the critical point. The potential F is plotted as a function of ψ for the three different transition types: (a) supercritical; (b) tricritical, and; (c) subcritical transition.

Therefore, ε can be expressed as

$$\varepsilon = [k\psi^4 + g\psi^2 - h\psi^{-1}], \tag{3.3}$$

where g, k, and h are free parameters. The ratio between the parameter g and k (Eq. 3.1) determines the order of the transition and the extent of the hysteresis and the parameter h corresponds to imperfections in the system. Plots of F as a function of ψ in a perfectly symmetric system for which $h = 0$ (perfect system) are shown in Fig. 3.1, where the control parameter ε is changed from below and above the critical point. Fig. 3.1 a & b, represent the potential energy in a supercritical and a tricritical transition, respectively. For $\varepsilon \leq 0$, the plots have one minimum, indicating that the system is stable at the symmetric state. Increasing the control parameter to $\varepsilon > 0$ will initiate a phase transition, resulting in the formation of two minimum points in the Landau potential. The system will evolve to one of the new minimum points into its new state, with an equal probability evolve to one minimum or the other. Fig. 3.1 c represents the potential energy in a subcritical transition. For $\varepsilon \leq 0$, the

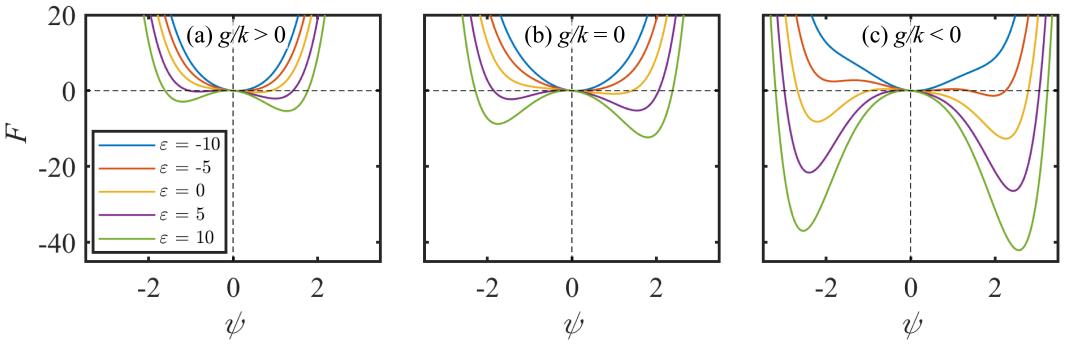

Figure 3.2: Landau potential in an imperfect system, $h \neq 0$. ε is varied above and below the critical point. The potential F is plotted as a function of ψ for the three different transition types: (a) supercritical; (b) tricritical, and; (c) subcritical transitions

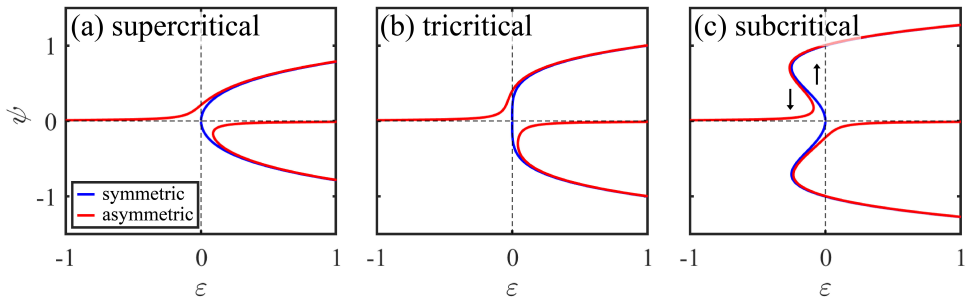

Figure 3.3: Sixth order polynomial Landau type model describing flow bifurcations near tricritical points (see Eq. 3.1). ψ is plotted as a function of ε for the three different cases of transitions near tricritical points: (a) supercritical smooth transition; (b) tricritical transition, and; (c) subcritical non-continuous transitions. Each sub-figure shows an example for a perfect system (blue) and a system with a slight imperfection (red).

plots have three minimum points, indicating that the state of the system has three different solutions, and it will evolve to one of them, depending on the history of the system. Increasing the control parameter to $\varepsilon > 0$ will initiate a change in the Landau potential, resulting in a potential with two minimum points.

This asymmetry will result in the development of asymmetric potential wells as seen in Fig. 3.2 a-c for supercritical, tricritical and subcritical transitions, respectively. Once the system is perturbed beyond equilibrium, it will have a high probability to evolve to the deeper potential well.

In Fig. 3.3, bifurcation diagram of ψ as a function of ε is plotted for the different transition types near a tricritical point (Eq. 3.3). A perfect system (in blue) can be calculated numerically and a slightly imperfect systems (in red) represents a more realistic experimental system. A supercritical 2^{nd} order continuous transition is plotted in Fig. 3.3 a, the transition at the tricritical point is plotted in Fig. 3.3 b and a subcritical 1^{st} order discontinuous transition with hysteresis is plotted in Fig. 3.3 c. When $g/k > 0$ the transition is a 2^{nd} order forward bifurcation (Fig. 3.3 a). When $g/k = 0$ the transition is tricritical (Fig. 3.3 b). At the tricritical point, ε and g/k simultaneously become zero. For $g/k < 0$ the transition is a 1^{st} order backward bifurcation, displaying a characteristic discontinuity in the curve and hysteretic behavior (Fig. 3.3 c). As previously mentioned, the parameter h accounts for any initial imperfections that may exist in the system. When initial conditions are slightly asymmetric, $h \neq 0$, it is pronounced in the roundness of the curve near $\varepsilon = 0$ (Fig. 3.3).

3.1 Flow transition in the Taylor-Couette cell

In the early 1980's it was shown that the Landau model can be used to describe flow transitions, such as the secondary instability in the low aspect ratio ($\alpha = l/r_o$) Taylor-Couette apparatus that was presented in Chapter 1, Fig. 1.4. b & c [49, 50]. Slight variations of α in a low α Taylor-Couette flow (with only a single pair of counter rotating vortices) leads to variation in the flow transition. The order parameter is

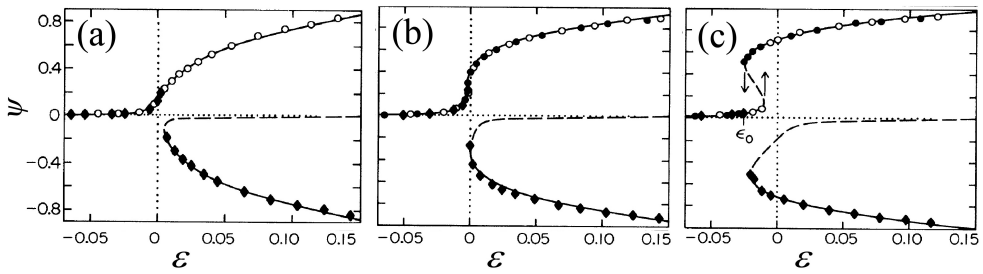

Figure 3.4: Tricritical transition in low α Taylor-Couette flow [49]. ψ is plotted as a function of ε, for (a) $\alpha = 1.129$, supercritical transition; (b) $\alpha = 1.266$, near tricritical transition, and; (c) $\alpha = 1.281$, subcritical transition. The data is fitted with Eq. 3.3.

defined in these experiments as $\psi = \int_0^l v_z dz / \int_0^l \mid v_z \mid dz$ where l is the height of the geometry and v_z is the axial velocity component. Hence, ψ is a measurement of the axial velocity along l in the vorticity direction, and it is plotted as a function of the control parameter $\varepsilon = v_w/v_{w,c} - 1$ (where v_w is the angular velocity and $v_{w,c}$ is the critical angular velocity of the rotor of the Taylor-Couette geometry). Aitta et al., have demonstrated in their analysis that the Landau model (solid and dashed lines) captures all types of the flow transitions, a smooth supercritical transition (Fig. 3.4 a), a tricritical transition (Fig. 3.4 b) and an abrupt subcritical transition (Fig. 3.4 c).

The time dependency of the transition in low aspect ratio Taylor-Couette flow cells

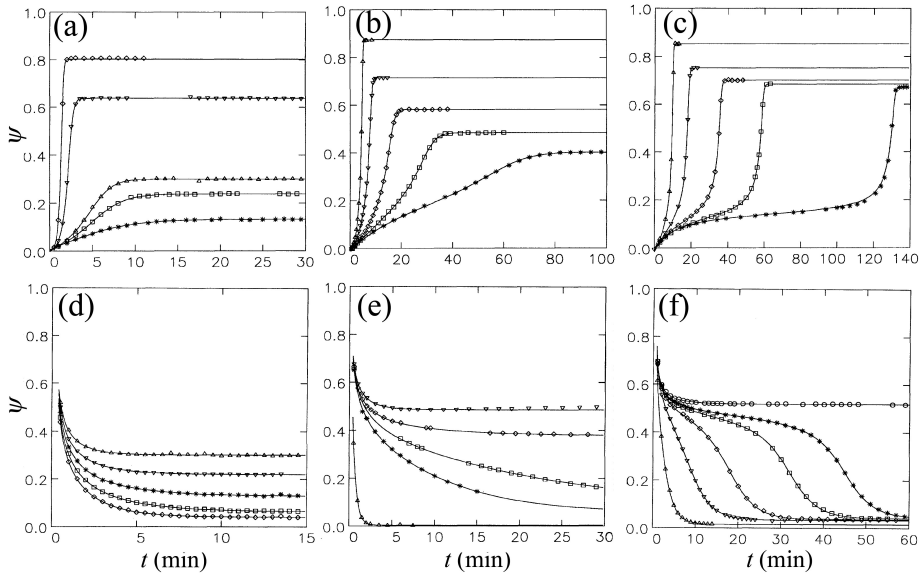

Figure 3.5: Dynamics of flow transition in low α Taylor-Couette flow [196]. ψ is plotted as a function of t, for (a & d) $\alpha = 1.129$, supercritical transition; (b & e) $\alpha = 1.266$, near tricritical transition, and; (c & f) $\alpha = 1.281$, subcritical transition. (a-c) v_w is increased from $v_w < v_{w,c}$ to $v_w > v_{w,c}$ and (d-f) v_w is decreased from $v_w > v_{w,c}$ to $v_w < v_{w,c}$. The data is fitted with Eq. 3.5.

was described by a dynamic form of the Landau model (Eq. 3.4) [196]:

$$\tau \frac{d\psi}{dt} = \frac{-dF}{d\psi}, \tag{3.4}$$

where τ is the characteristic time required to induce a transition in ψ. Combining with Eq. 3.3, we obtain a dynamic model for the instability,

$$\tau \dot{\psi} = [h + \varepsilon\psi - g\psi^3 - k\psi^5]. \tag{3.5}$$

The dynamic results for the Taylor-Couette experiments were plotted in Fig. 3.5 for increasing values of v_w (from $v_w < v_{w,c}$ to $v_w > v_{w,c}$, Fig. 3.5 a-c) and for decreasing values of v_w (from $v_w > v_{w,c}$ to $v_a < v_{a,c}$, Fig. 3.5 d-f), for supercritical, tricritical and subcritical transitions. The results for the dynamic flow experiments were found to be quite different when the order of the transition changed with different aspect ratios, slowing down when approaching a tricritical point [196]. The shape of the potential wells plotted in Fig. 3.1 and 3.2 explain the nature of the dynamics of the transition. Shallow potential wells that form for ε that is slightly above $\varepsilon = 0$, lead to F at $\psi = 0$ that is nearly flat which translates to slow transition dynamics. This dynamic model will be used for describing the time dependency of the symmetry breaking flow transition in the cross-slot geometry (Chapter 4).

3.2 Flow transition in the cross-slot geometry

Similar to the experiments done with the Taylor-Couette geometry, quasistatic experiments and numerical simulations were also conducted with cross-slot geometries with low aspect ratios on the order of $\alpha \simeq 1$. Numerical simulations revealed that the order of the transition in the cross-slot geometry was also strongly dependent on the aspect ratio with a tricritical point at $\alpha = 0.55$ (Fig. 3.6) [90].

As shown in the introduction, the flow instability in the Taylor-Couette is a centrifugal flow instability while the flow instability in the cross-slot geometry is a stagnation point instability. Even though these are different instabilities that occur in different flow fields, the nature of symmetry breaking flow transition is very similar and both can be described with the Landau model.

3.2.1 The order parameter ψ in the cross-slot geometry

There are many possible definitions for the order parameters ψ. In this thesis, the two definitions that will be used are shown in Eq. 3.6 and Eq. 3.7.

In the cross slot geometry, the order parameter can be defined as the x component of the central point vorticity $\omega_x = (\partial v_z/\partial y) - (\partial v_y/\partial z)$ which is the local rate of rotation in a fluid, $\vec{\omega} = \vec{\nabla} \times \vec{v}$.

$$\psi = sgn(\omega_x \mid_{y=z=0}) \omega_x \mid_{x=y=z=0} . \tag{3.6}$$

Alternatively, a dimensionless order parameter can be calculated as the sum of ω_x

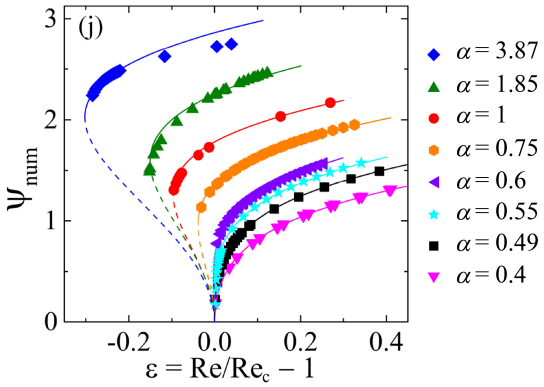

Figure 3.6: Numerical simulations of the order parameter as a function of normalized Re for different α [27]. The order of the phase transition shows strong dependency on α. For $\alpha < 0.55$ the transition is of 2^{nd} order, for $\alpha = 0.55$ the transition is tricritical and for $\alpha > 0.55$ the transition is 1^{st} order as indicated by the discontinuity of the function.

divided by the sum of $\mid \omega_x \mid$ over the $x = 0$ plane:

$$\psi = sgn(\omega_x \mid_{y=z=0}) \frac{\int_{-\frac{w}{2}}^{\frac{w}{2}} \int_{-\frac{d}{2}}^{\frac{d}{2}} \omega_x dz dy}{\int_{-\frac{w}{2}}^{\frac{w}{2}} \int_{-\frac{d}{2}}^{\frac{d}{2}} \mid \omega_x \mid dz dy}. \tag{3.7}$$

This definition is particularly useful for detecting small fluctuations across the field in time dependent experiments.

Positive or negative values of ω_x are possible, depending on which vortex pair intensifies. However, ψ is made to be always positive by accounting for the sign of $\omega_x \mid_{y=z=0}$.

As described in the Introduction, Chapter 1, Section 1.2.1, when $\text{Re} < \text{Re}_c$ the flow in the cross-slot geometry is symmetric and at equilibrium. At this point, $\psi = 0$.

Loss of equilibrium by an increase in Re to $\text{Re} > \text{Re}_c$ is expressed by the intensification of a co-rotating Dean vortex pair and the generation of center point vorticity ($\omega_x > 0$) which leads to $\psi \neq 0$. Upon reaching the critical value of Re, the flow bifurcates to one of two stable solutions, depending on which of the two pairs of Dean vortices intensify and eventually merge to a single central vortex (see Fig. 1.9).

In cross-slot devices, wall imperfections due to limitations in fabrication can lead to non-zero h, while in the numerical simulations they are completely avoided and $h = 0$ (as seen in Fig. 3.6). The imperfections in the experimental system can cause a favored branch or handedness for the transition, i.e. clockwise or anticlockwise vortex formation. However, in numerical simulations these imperfections are avoided and hence the Landau potential is perfectly symmetric, therefore, clockwise or anticlockwise rotation have the same probability to occur.

3.2.2 The control parameter ε in the cross-slot geometry

The control parameter ε is a normalized Re around the critical value (Re_c) and defined as:

$$\varepsilon = \frac{Re}{Re_c} - 1. \tag{3.8}$$

According to this definition, ε is assumed to vary linearly with Re_c. In order to test the validity of the linear approximation of ε, the theoretical value of ε is calculated for the cross-slot experimental system. According to Aitta [50], the linear approximation of the control parameter ε = Re/Re_c-1, is valid only near Re_c. More generally, ε is assumed by Aitta [50], to behave as a parabola of the following form:

$$\varepsilon_{Aitta} = p(X^2 + 2XY + Y^2 + 2X - 2Y + 1), \tag{3.9}$$

where p is a constant and X and Y are defined as:

$$X = \frac{Re_x - Re}{Re_m - Re_x}, \tag{3.10}$$

and

$$Y = \frac{\alpha - \alpha_m}{\alpha_x - \alpha_m}. \tag{3.11}$$

Here, Re_x is the smallest critical Re in which the transition occurs and α_x is the corresponding aspect ratio. α_m is the smallest aspect ratio in which the transition occurs and Re_m is the corresponding critical Re. According to Aitta, the control parameter ε depends quadratically on Re and therefore it is a reasonable assumption that the phase curve is a parabola. We found that the phase curve for our cross-slot flow was oriented in the opposite way of the Taylor-Couette phase curve, and therefore the parameters are defined slightly different from those described in Aitta's papers [50, 196]. An estimated $\alpha_m = 0.4$ is used, which is the smallest aspect ratio for which

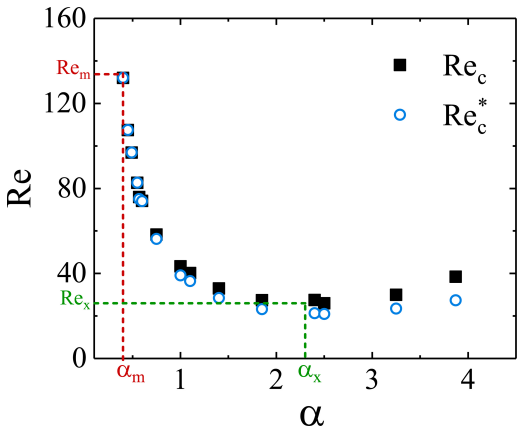

Figure 3.7: Phase curve for the onset of the flow instability in the cross-slot geometry. Black squares describe the non-hysteretic branch (Re_c) and blue circles describe the hysteretic branch (Re_c^*). Data is taken from both experiments and numerical simulations from the current work and from [27].

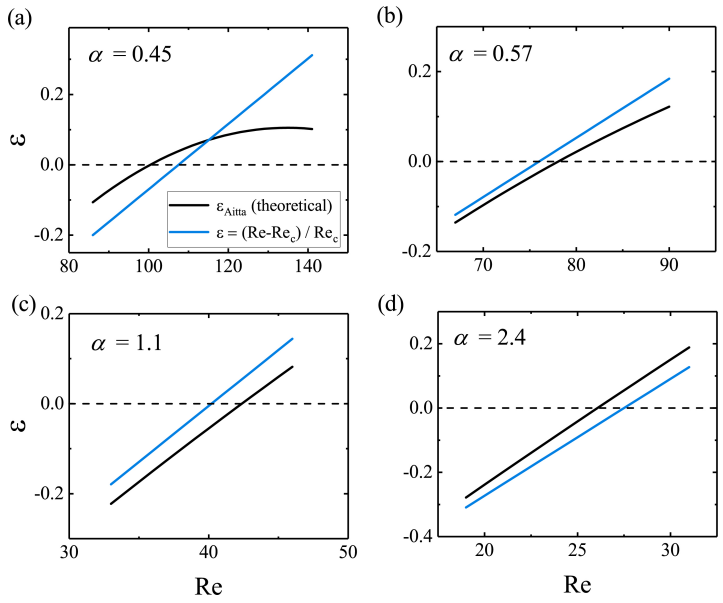

Figure 3.8: Comparison between the theoretical prediction of ε_{Aitta} and the linear approximation of ε. dashed line indicates the critical value where $\varepsilon = 0$.

we have data for, and $\mathrm{Re}_m = 132$ is the corresponding Re. $\mathrm{Re}_x = 26$ is the smallest Re at which the transition appears according to the minimum point of the phase curve (Fig. 3.7), $\alpha_x = 2.3$ is the corresponding aspect ratio.

The solutions to Eq. 3.9 are:

$$X_{1,2} = -(1 \pm \sqrt{Y})^2. \tag{3.12}$$

Then, the expression for ε can be re-written using 3.12 and 3.11,

$$\varepsilon_{Aitta} = -p(X - X_1)(X - X_2), \tag{3.13}$$

and therefore,

$$\varepsilon_{Aitta} = -p\frac{(Re - Re_1)(Re - Re_2)}{(Re_c - Re_m)^2}, \tag{3.14}$$

where Re_1 and Re_2 can be calculated:

$$Re_{1,2} = -X_{1,2}(Re_m - Re_c) - Re_c. \tag{3.15}$$

Fig. 3.8 shows the theoretical ε and the linear approximation of ε in the Re range that will be used in this thesis. From this analysis we can conclude that it is reasonable to use a linear approximation of ε near the critical point and therefore there is no need for the complex definition with multiple unknown variables when defining ε. A linear approximation of ε allows us to perform reliable curve fitting to our experimental data, which enables to extract the parameters from the model and quantify the size of the hysteresis loop, the asymmetry in our system and the critical Re in which the flow instability occurs. Nevertheless, it is noted that the theoretical ε becomes increasingly non-linear as α decreases (Fig. 3.8 a) displaying a clear curvature for the lowest $\alpha = 0.45$. This will be considered in the later analysis given in Chapter 4.

Chapter 4

Controlled symmetry breaking and vortex dynamics in intersecting flows

In this chapter (adapted from our publication [1]) we discuss how vortex dynamics depends on the nature of the flow transition that develops in the cross-slot geometry when Re is increased beyond a critical value, Re_c. Our observations and analysis show that changing the aspect ratio, α, affects the degree to which the Dean vortices, that appear due to the curving streamlines in the flow, are confined within their respective quadrants of the channel cross section (lower α implies greater confinement). Our findings show that by controlling α we are able to modify the relative rates of vortex merging and splitting as Re is increased or decreased, respectively, past the critical point. By reducing the aspect ratio we are able to reduce the relative vortex intensity resulting in a weak attraction between co-rotating vortices. In this chapter we find the link between vortex dynamics and symmetry breaking, which provides a rationalization for the emergence of hysteresis in the system at higher values of α.

4.1 Introduction

The formation of vortices in confined spaces such as pipes and micro-sized channels or veins and arteries is common, yet due to experimental limitations, confined merging and splitting of vortices was not reported in the literature. Since the basic structure of vortical flows is independent of Re, the process of merging and splitting is expected to show similarities across length scales (as discussed in the introduction section 1.2.2). Therefore, we anticipate that principles derived from the micro-scale experiments presented in this chapter will have general applicability.

By employing the cross-slot geometry, we can control the dynamics of both vortex merging and splitting. At low values of Re the flow along the outlet channels is symmetric along y and z and comprises of four cells of Dean vortices (Fig. 4.1 a). However, if Re is increased beyond a critical value Re_c, the flow breaks symmetry and one pair of co-rotating Dean vortices approach each other (Fig. 4.1 b) and merge to form a single steady streamwise stretched vortex (similar to a Burgers vortex described in the Introduction, Chapter 1, Section 1.1.2) [51, 55], centrally aligned along the outlet channel (Fig. 4.1 c). By reducing the Reynolds number from an initial value $\mathrm{Re} > \mathrm{Re}_c$,

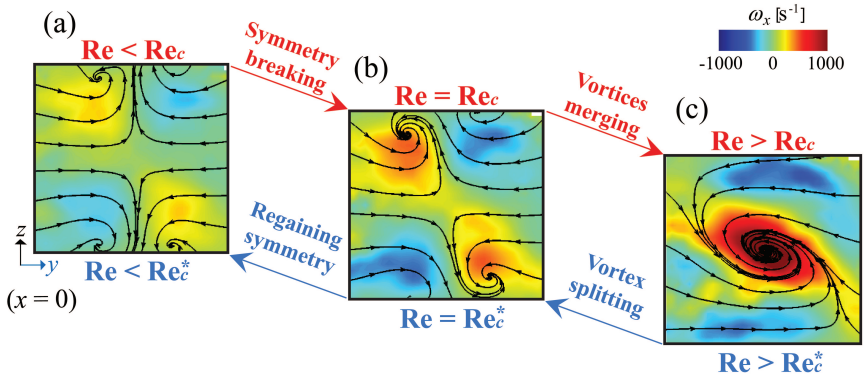

Figure 4.1: Flow transitions in the cross-slot geometry [1]. μ-PIV images of the vorticity field at $x = 0$: (a) a symmetric flow field with 4 cells of Dean vortices; (b) an asymmetric flow field where two intensified Dean vortices have commenced to merge; and (c) a single steady, central streamwise vortex is formed by the merging of the two Dean vortices.

to a final value $\mathrm{Re} < \mathrm{Re}_c^*$ the opposite process is observed, and a single vortex splits into two co-rotating vortices that migrate away from each other as the flow regains its symmetry.

Using SLE-fabricated cross-slots (see Methods Section 2.1), the processes can be directly visualized, and the streamwise vorticity can be quantitatively measured using time-resolved flow velocimetry. In our experimental system, each of the Dean vortices is confined within a quadrant of the channel cross section that is dictated by the boundaries of the channel and by the neighboring counter-rotating vortices. As a result, the Fujiwhara effect, in which co-rotating vortices mutually orbit each other around a point between them, is eliminated. Typical experiments in vortex dynamics studies exhibit the Fujiwhara effect and therefore a rotating reference frame is needed when analyzing the results. Besides avoiding a rotating reference frame, our experimental set-up eliminates any uncertainties in the determination of vortex location [101, 197, 198]. In addition, in our experimental set-up the Re can be maintained as a constant throughout an experiment, allowing to keep a constant distance between vortices that are in the process of merging or splitting.

As described in details in the Methods, Chapter 2, Section 2.4, we perform experiments by controlling Re in two distinct ways: (1) increasing and decreasing small quasistatic ramps of Re in which the flow is observed under steady conditions at each Re increment and, (2) large step increases or decreases in Re in which the flow is observed as it dynamically approaches the steady state at above or below Re_c.

Previous numerical studies of the vortex shedding downstream of a circular cylinder [199] have indicated that vortex dynamics is linked to symmetry breaking transitions. In our work we experimentally show, for the first time, that there is a mutual relationship between symmetry breaking and the merging and splitting of vortices. Furthermore, we show that the intensity of Dean vortices and distance between them, is determined by the aspect ratio α of the rectangular inlet and outlet channels.

Since the onset of the flow asymmetry is interrelated to the merging process, we

will describe the flow asymmetry by using the Landau model and study its relation to the merging and splitting process.

Through time dependent experiments we find that the relation between the emergence of a flow instability and the onset of merging to be independent of Re. We discover the effect of confinement on the merging and splitting of vortices and identify possible changes in the physical mechanism that governs the process.

Our findings not only suggest that the mechanism of vortex merging can be affected by confinement of the vortices, but they also introduce a new approach in the study of vortex dynamics and specifically vortex splitting and its mechanism in a well controlled experimental frame.

4.2 Quasistatic control of Re

4.2.1 Direct experimental observation on a streamwise vortex in a square channel cross-slot flow

For an overall view on the Re parameter range where the flow instability appears, initial observations were conducted with a confocal microscope (DSD2, Andor Technology, Methods Section 2.2) focused on the $x = 0$ plane of a square cross section cross-slot device with $\alpha = 1$ (as described in the Methods Sections 2.1 and 2.2). For flow visualization, water mixed with fluorescent dye is introduced from the left inlet while pure water is introduced from the right inlet. Snapshots of the flow field are taken for quasistaticaly increasing and decreasing Re (Fig. 4.2). At Re = 20 the flow is symmetric and stable, increasing Re to a critical value ($\mathrm{Re}_c \simeq 40$) results in symmetry breaking and the initiation a spiral vortex formation at the center of the $x = 0$ plane. Further increase in Re results in an increase of the vortex size and additional loops are added to the spiral vortex (Fig. 4.2 top row). At Re $\sim$ 128 secondary spirals form in the top-left and bottom-right of the image, creating a "mushroom" shape, similar to the findings in [27]. At Re $>$ 280 the spiral structure no longer holds as the flow becomes unsteady. When the experiments begin at Re $>$ 280 and then Re is reduced in a quasistatic manner (Fig. 4.2 bottom row) the steady spiral structure holds for

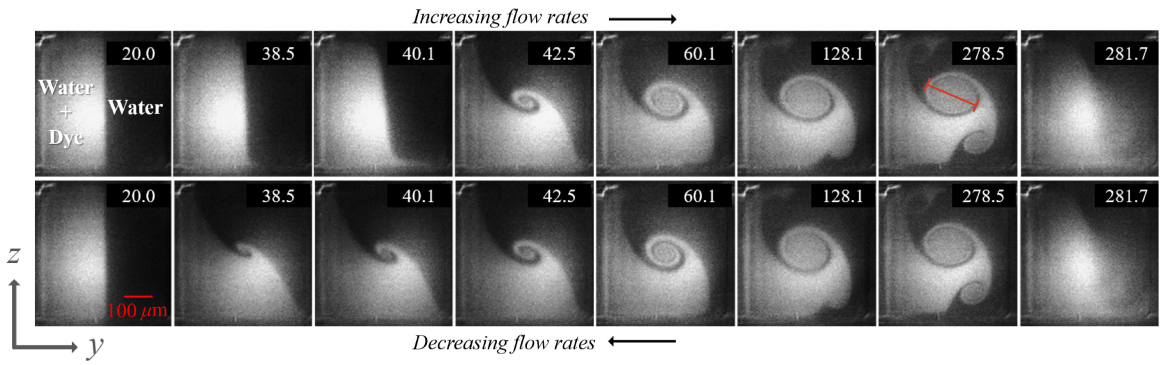

Figure 4.2: Initial direct observation of the flow instability with a confocal microscope, Re is indicated in the labels, red line marks the diameter of the central vortex, d_{vortex}.

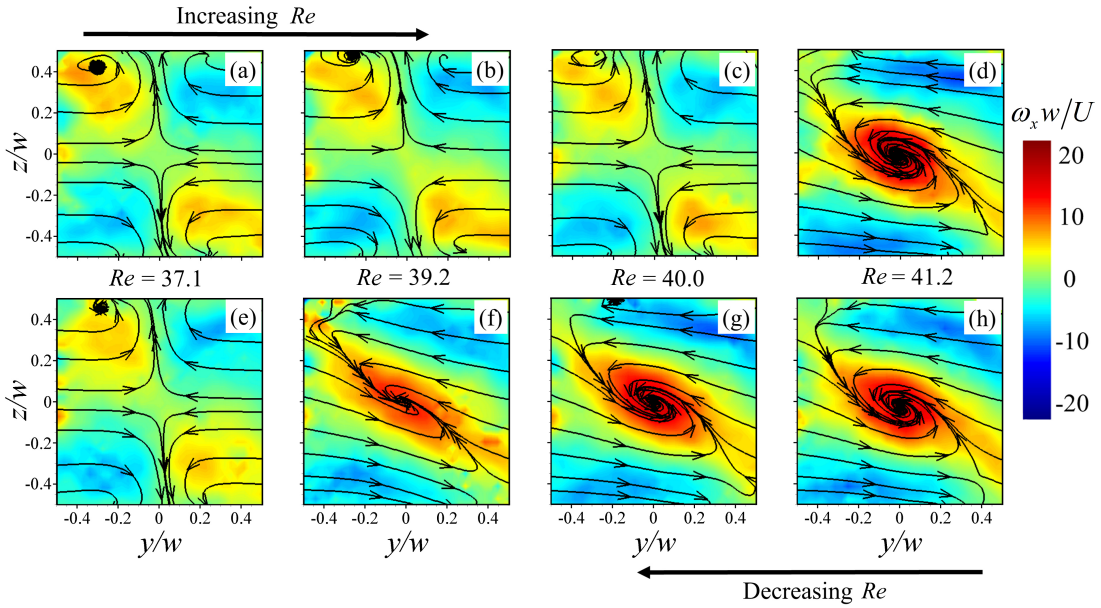

Figure 4.3: μ-PIV images of vorticity in the $x = 0$ plane measured under the quasistatic experimental condition with $\alpha = 1$ [3]. Parts (a)-(d) show results for progressive increases in Re from $\mathrm{Re} < \mathrm{Re}_c$ to $\mathrm{Re} > \mathrm{Re}_c$, while parts (h)-(e) show progressively decreasing Re from $\mathrm{Re} > \mathrm{Re}_c$ to $\mathrm{Re} < \mathrm{Re}_c^*$. (a) & (e) Re = 37.1; (b) & (f) Re = 39.2; (c) & (g) Re = 40.0; (d) & (h) Re = 41.2. The color scale indicates the local value of the normalized axial vorticity.

$\mathrm{Re} < \mathrm{Re}_c = 38.5$, which indicates the existence of hysteresis in the system.

Flow measurements are conducted using μ-PIV in the channel cross section at the centerplane ($x = 0$ plane) for increasing and decreasing Re ramps. With this measurement technique we can quantitatively characterize the flow transition in detail, and validate our experimental setup and the measurement technique with previous studies. The results from μ-PIV experiments in a microfluidic cross-slot geometry with $\alpha = 1$, close to Re_c are shown in Fig. 4.3. Here, for increasing Re, starting at Re = 37.1 (Fig. 4.3 a) the flow is steady and symmetric. The two incoming fluid streams from opposing y-directions meet at $y = 0$ and form an essentially straight interface along the z-axis. At this Re, the four cells of Dean vortices previously reported in the numerical simulations of Haward *et al* [27] are already apparent in the four quadrants of the channel cross-section.

In Fig. 4.3 a, the four Dean vortices are relatively balanced and hence the interface is straight and symmetric. As Re is increased (Fig. 4.3 b, c) the flow remains approximately symmetric, with a slight tilt of the interface between incoming fluid streams with respect to the y and z axes. This tilt results from an imbalance between the two diagonally-opposed pairs of co-rotating Dean vortices. This asymmetry leads to a small non-zero value of the centerpoint axial vorticity. For $\mathrm{Re} > \mathrm{Re}_c \approx 40$ a fully-developed steady spiral vortex forms, centered on $y = z = 0$ with a counter clockwise rotation, about the x-axis (Fig. 4.3 d). At this stage, the centerpoint axial vorticity jumps greatly in its magnitude, indicating a discontinuity in the flow transition. As

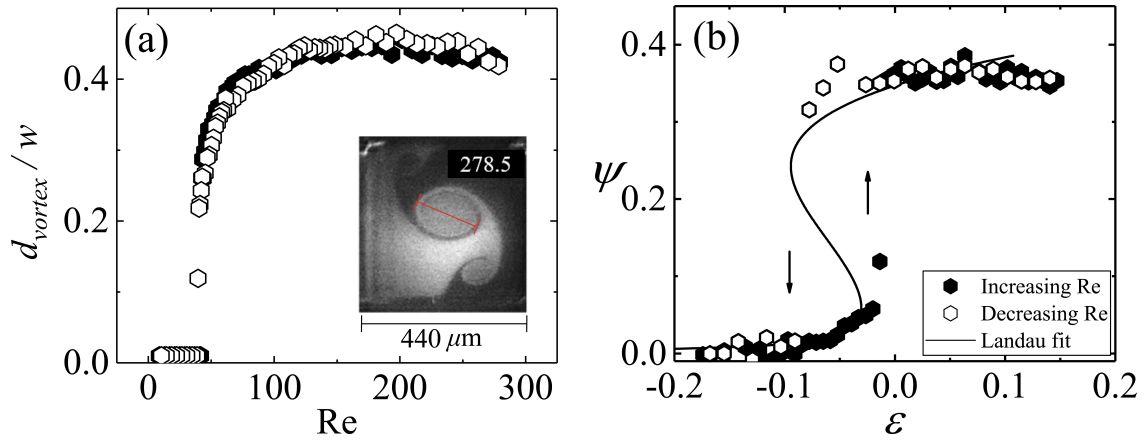

Figure 4.4: Central spiral vortex in a cross-slot with $\alpha = 1$. (a) Confocal microscope data of normalized central spiral vortex diameter, d_{vortex}, as a function of Re. (b) μ-PIV data of ψ as a function of ε, in the proximity of the critical point ($\varepsilon = 0$), revealing the hysteresis in the transition, arrows indicate the jump between stable and unstable branches. The data is fitted with the Landau model presented in Chapter 3, Eq. 3.3.

expected for a Newtonian fluid in a cross-slot device of square cross-section (i.e. $\alpha = 1$) [27], hysteresis is observed in the transition. When the Reynolds number is slowly decreased from $\mathrm{Re} > \mathrm{Re}_c$ (Fig. 4.3 e-h) we find that the flow only recovers symmetry once $\mathrm{Re} < \mathrm{Re}_c^* = 38.8$.

The central vortex diameter, d_{vortex} is extracted from the measurements conducted with the confocal microscope (Fig. 4.2) and normalized with the width of the channel, $w = 440$ μm. Measurement of d_{vortex} is demonstrated by the red line in the inset of Fig. 4.4 a. A plot of d_{vortex}/w as a function of Re is presented in Fig. 4.4 a, showing how the central spiral diameter changes when Re is increased. Upon Re_c, the central vortex is formed with a CCW rotation and its diameter rapidly grows, where it reaches a peak size at $\mathrm{Re} \sim 130$. The central vortex size remains stable up to $\mathrm{Re} \sim 200$ where two additional CW rotating side vortices appear. For $\mathrm{Re} \gtrsim 200$, a small decrease in the diameter of the central vortex is seen and eventually the flow becomes unsteady at $\mathrm{Re} = 280$.

The order parameter ψ (as defined by Eq. 3.7) is extracted from μ-PIV measurements (Fig. 4.3) and plotted as a function of the control parameter ε (Eq. 3.8) for a narrow range near the flow transition region (see Fig. 4.4 b). The plot is fitted with the Landau model (Chapter 3, Eq. 3.3), revealing the critical values of $\mathrm{Re}_c = 40.2$ and $\mathrm{Re}_c^* = 38.0$.

These findings are in close agreement with experimental and numerical observations conducted with a similar system by Haward *et al* [27]. However, we point out that in their work, it was not possible to resolve the hysteresis in the flow transition experimentally and they could find indications on hysteresis from numerical simulations only. In their experiments, laser-scanning confocal microscopy was employed to visualize dye-advection patterns in the channel cross-section, however, their microfluidic cross-slot device was not vertically mounted, and the only direct observation was obtained at the $x - y$ plane. In order to visualize the $y - z$ plane in their system, they had to perform

multiple scans of the $x-y$ plane across the z direction and then reconstruct the $y-z$ plane. Performing quasistatic variations in the Re was not possible and therefore hysteresis could not be resolved [27]. Furthermore, comparisons between the results of the experiments and the numerical simulations were made using different order parameters: a specific local velocity component in the case of the numerical simulations and a dilution-based mixing parameter in the case of the experiments [27]. Here, with our glass microfluidic devices and μ-PIV measurements, not only we resolve the hysteresis experimentally, but we also directly obtain quantitative spatially-resolved information on the velocity field which can be directly compared with numerical simulations.

4.2.2 Flow bifurcation and the Landau potential in a cross-slot flow with different aspect ratios

In this section, we present the results of quasistatically controlled ramps of increasing and decreasing Re carried out in the four cross-slot devices with different values of α (for microfluidic device specifications see Methods, Chapter 2, Section 2.1.2). The flow bifurcation in each device is characterized in detail in terms of the Landau model (from which we produce a phase diagram for the transitions). We then proceed to analyze vortex merging and splitting of the dominant Dean vortex pair.

As defined in Chapter 3, Eq. 3.7, the quantity ψ is plotted as a function of the normalized control parameter $\varepsilon = (\mathrm{Re}/\mathrm{Re}_c) - 1$ for all values of α in Fig. 4.5. Increasing ramps in Re are represented by solid symbols and decreasing ramps by open symbols. In all cases, the data are well described with the Landau model, Eq. 3.3 (solid lines), from which we obtain the parameters g, k, h, and Re_c. For subcritical transitions ($g < 0$) we also obtain $\mathrm{Re}_c^* = \mathrm{Re}_c(1 - g^2/4k)$. For $g \geqslant 0$, $\mathrm{Re}_c^* = \mathrm{Re}_c$. All the parameters extracted from the Landau model fit are summarized in Table 4.1.

Table 4.1: Landau model parameters in different cross-slot devices.

α	Transition type	Re_c	Re_c^*	gk^{-1}	h
0.45	supercritical	107.5	107.5	0.11	0.001
0.57	near tricritical	76.0	75.0	-0.03	0.0001
1.1	subcritical	40.2	36.5	-0.12	0.0012
2.4	subcritical	26.5	21.4	-0.14	-0.002

As discussed in Chapter 3, the Landau model does not account for any underlying mechanisms behind a physical phenomenon, but the parameters of the model (Eq. 3.3) may have physical significance. For example, a perfect bifurcation will appear as a sharp transition in ψ at $\varepsilon = 0$. In a perfect experimental system, the transition will be just as likely to result in a positive or a negative value of ψ, due to the symmetric shape of the Landau potential (see Chapter 3, Fig. 3.1). However, for our microfluidic devices, we do not observe perfect bifurcations and the h parameter, gives us indication about how "perfect" our experimental system is (or how asymmetric the Landau potential is, see Chapter 3, Fig. 3.2). Although small, in our experiments, the h parameter is always non-zero, as specified in Table 4.1. The value of h with smallest magnitude is

found for $\alpha = 0.57$ and it can be seen in the sharpness of the transition of ψ near $\varepsilon = 0$ (Fig. 4.5 b). A larger magnitude h term is found for $\alpha = 2.4$ as can be seen in the noticeable roundness of ψ near $\varepsilon = 0$ (Fig. 4.5 d). The other free parameters in the model, g and k are inter-related. When k is set to 1, the ratio gk^{-1} will remain the same as for the case where k remains a free parameter. Therefore, the ratio between these parameters is the only real free parameter in our fit and it determines the width and shape of the hysteresis loop, the values are specified in Table 4.1. The relation between the parameters g and k to α is found through exponential curve fitting to the values extracted from the Landau model, $g = -4.7 + 9.9e^{-1.6\alpha}$ and $k = 32.4 - 107.1e^{-2.7\alpha}$.

As expected by prediction of numerical simulations [27], our data reveal that a supercritical transition occurs at the lowest aspect ratio, $\alpha = 0.45$ (Fig. 4.5 a). A near tricritical transition is observed for $\alpha = 0.57$ (Fig. 4.5 b), for which the transition

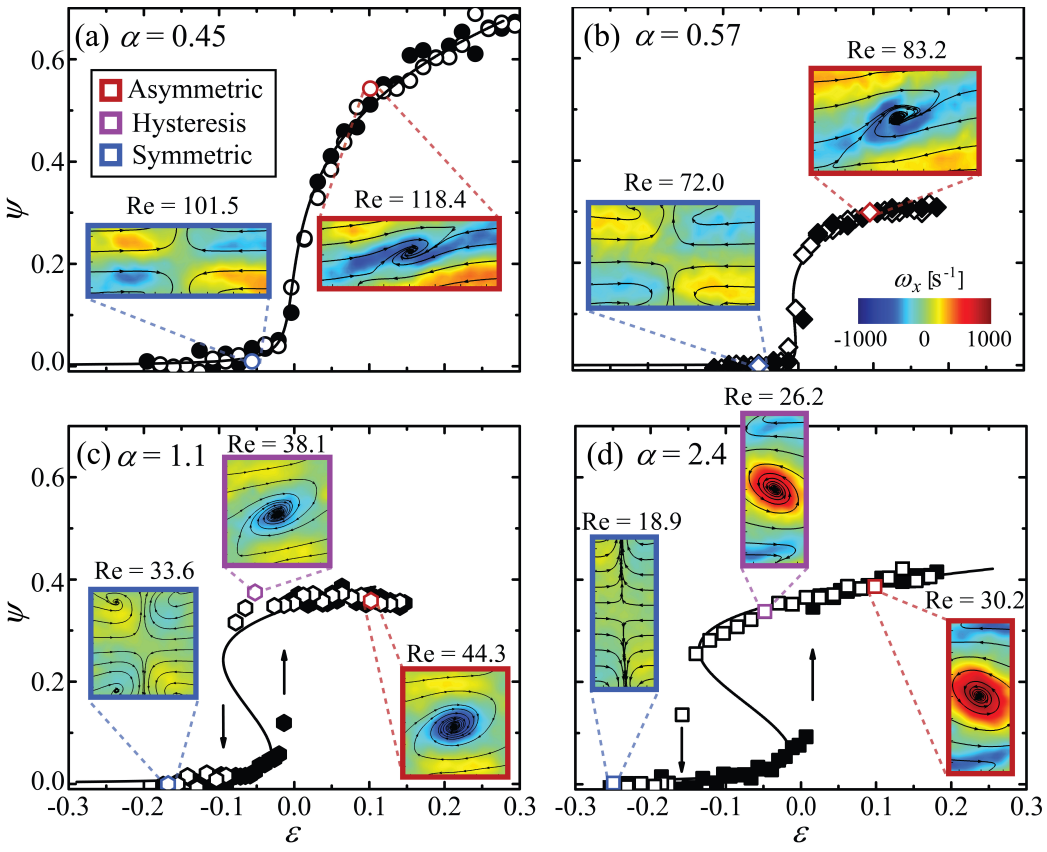

Figure 4.5: The order parameter ψ as a function of the control parameter ε for quasistatic measurements in cross-slot channels with different α [1]. (a) Supercritical transition for $\alpha = 0.45$, (b) near tricritical transition for $\alpha = 0.57$, (c) subcritical transition with a small hysteresis loop for $\alpha = 1.1$, and (d) a larger hysteresis loop for $\alpha = 2.4$. Closed and open symbols represent data obtained by controlled increases and decreases in Re, respectively. Curves are fitted with the Landau model [Eq. (3.3)]. Arrows indicate the jump between stable and unstable branches where hysteresis is detected. Insets are μ-PIV images of the vorticity at the center plane ($x = 0$) at the values of Re indicated above each image.

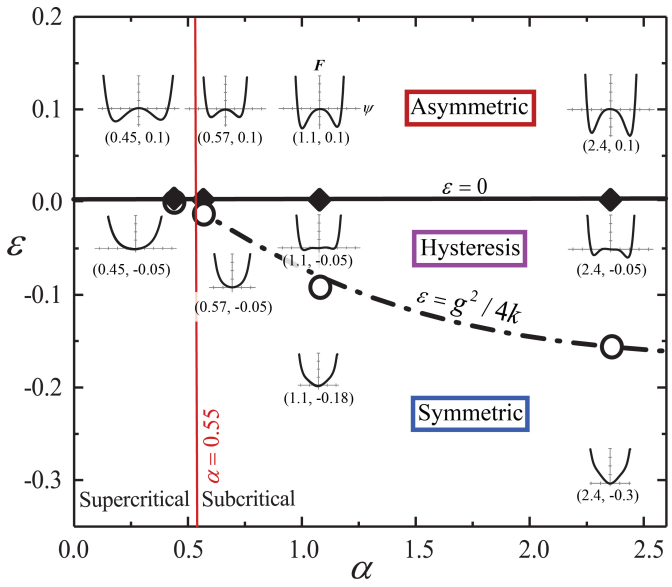

Figure 4.6: Phase diagram for the flow transitions in (α, ε) parameter space, the Landau potentials are indicated (ψ as a function of F found with Eq. 3.1) [1].

appears slightly backwards, but $\mathrm{Re}_c^* = \mathrm{Re}_c$ within experimental error. Subcritical transitions with small and larger hysteresis loops, occur at $\alpha = 1.1$ and $\alpha = 2.4$, respectively (Figs. 4.5 c and 4.5 d).

From Table 4.1, we can see that Re_c increases as α is decreased. The confinement of the flow field by the solid channel walls at $z = \pm d/2$ increasingly stabilizes the flow as α is decreased, and therefore a higher Re_c is needed for the symmetric flow state to become unstable. The insets of Fig. 4.5 show contour plots of the vorticity over the $x = 0$ plane (an average of 15 images) with superimposed streamlines. These plots demonstrate the flow field for decreasing Re ramps from values above Re_c. The flow fields enclosed by a red frame show a single spiral vortex structure for $\varepsilon = 0.1$. The flow field enclosed by a blue frame corresponds to symmetric stable flow at $\mathrm{Re} < \mathrm{Re}_c^*$. For $\alpha = 0.45$ and 0.57 the symmetric flow state is regained at $\varepsilon \leqslant 0$ (see Fig. 4.5 a-b). For the channels with higher $\alpha = 1.1$ and $\alpha = 2.4$, the regaining of symmetry happens at lower values of $\varepsilon \leqslant -0.1$ and $\varepsilon \leqslant -0.18$ (respectively), due to hysteresis (Fig. 4.5 (c) and 4.5 d). For these cases, we show an additional inset flow field (enclosed in a mauve frame) for conditions within the hysteresis loop, where $\varepsilon = -0.05$ and the vortex has lower intensity when compared to the intensity at $\varepsilon = 0$.

We note that for $\alpha = 0.45$, the order parameter ψ reaches significantly higher values when compared to the other aspect ratios. This difference is related to the vortex flow field that develops at this high flow confinement and will be further discussed in Chapter 5.

By varying α and ε we can control the shape of the Landau potential and the free energy of the system. The Landau potentials ($F(\psi)$, Eq. 3.1) can be calculated from the parameters used to fit Eq. 3.3 to the experimental bifurcation diagrams in Fig. 4.5. Examples of $F(\psi)$ for various (α, ε) are shown as insets in the phase diagram presented in Fig. 4.6. The vertical red line in Fig. 4.6 marks the aspect ratio $\alpha = 0.55$

for which a tricritical point is formed at $\varepsilon = 0$. To the left hand side of the red line, the transition will be supercritical and to the right hand side the transition will be subcritical. The black horizontal line marks the line of critical points, where $\varepsilon = 0$. The dash-dot black line marks Re_c^* and the hysteretic curve, where $\varepsilon = g^2/4k$. Below the dashed-dotted line, F has a single minimum at $\psi = 0$, indicating that symmetric flow is always the only stable state. Above the solid black line, for $\varepsilon > 0$, F has a maximum at $\psi = 0$ (symmetric flow becomes unstable), and acquires two new minima, the new stable points, where the flow is asymmetric. The left-hand-side minimum corresponds to a negative solution ($\psi < 0$, clockwise rotation) while the right-hand-side minimum corresponds to a positive solution ($\psi > 0$, counter-clockwise rotation). Since the bifurcations in these experiments are not perfect, and we get a non-zero h term in Eq. 3.3, one minimum will be deeper than the other, and to this deeper well the instability will evolve corresponding with the direction of the vortex rotation. Between the black solid line and the black dashed-dotted line is the hysteretic region in which F has three minima and the symmetric state can be either stable or unstable, depending on the history of the system.

As ε is increased up to the onset of the asymmetry, and becomes non-zero, a dominant pair of co-rotating Dean vortices begin to approach each other in the process of merging. In Sec. 4.2.3, we describe for the first time, a controlled merging process captured during quasistatic experiments. We will also present the data from the opposite experiments, in which a single vortex splits into two corotating vortices that migrate away from each other as ε is decreased in a quasistatic fashion.

4.2.3 Quasistatic vortex merging and splitting

In the process of vortex merging, two co-rotating vortices grow in size and share their outer vorticity bands as they approach each other. This process and its mechanism has been described in detail in the literature for unconfined macroscale vortices [91–99]. The first stage of merging is recognized as the slow stage in which diffusive growth of the vortex cores is seen and the vortex cores slightly move towards each other. Once a critical ratio between size and distance is met, typically $0.24 \leq a/b \leq 0.32$, a convective stage will begin. In the fast convective stage, the vortices will deform, share filaments and will rapidly move toward each other. The final third stage is the merged diffusive stage in which the two vortices are merged into a single structure [94, 200, 201]. Some studies have reported a fourth stage in the merging process, which is referred to as a second diffusive stage (a slow down in the merging process), that follows the convective stage, prior to the final merging [92–94].

In all of the previous reports, the experiments were time dependent, where only the initial Re was controlled [91, 93, 200–203]. Here, with quasistatic experiments, we are able to precisely control Re in very small increments, which allows us to arrest the merging process at any stage while maintaining a constant background flow. To the best of our knowledge, such a controlled experimental system for the study of vortex merging was not reported before.

The process of merging is commonly studied by following the distance between the cores of the merging vortices, b, normalized by the maximal distance between the cores b_0 [102]. In order to identify the location of the cores first we need to define the planar

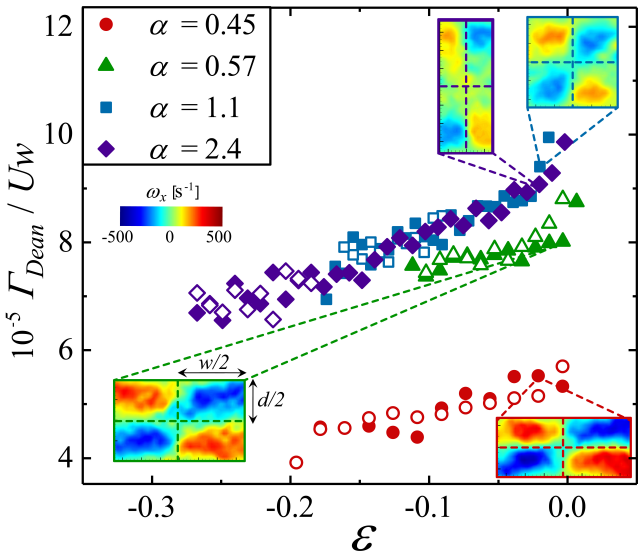

Figure 4.7: The nondimensional circulation Γ_{Dean}/Uw of a quadrant from the cross section at $x = 0$ is plotted as a function of ε [1]. Closed and open symbols correspond to increasing and decreasing increments in Re. Insets are μ-PIV images of the vorticity at $x = 0$ for $\varepsilon = -0.02$, dashed lines divide the flow field into the defined quadrants.

domain in which the vortex is confined and find the circulation of the Dean vortex (Γ_{Dean}) within the domain. In our experiments, it is reasonable to assume that the planar domain for each Dean vortex is its respective quadrant of the cross-section of the channel. The circulation in each quadrant, Γ_{Dean} is given by:

$$\Gamma_{Dean} = \int_0^{\pm\frac{w}{2}} \int_0^{\pm\frac{d}{2}} \omega_x dz dy. \tag{4.1}$$

In our experimental system, an equivalent analysis can also be performed for vortex splitting, i.e., b can be evaluated as Re is progressively reduced as well as increased for $\mathrm{Re} < \mathrm{Re}_c$.

In Fig. 4.7 the non-dimensionalized average circulation of the two merging Dean vortices Γ_{Dean}/Uw is plotted as a function of ε for $\varepsilon < 0$. From this figure we can see that the maximal circulation of a Dean vortex is measured just before the onset of the asymmetric flow. We note that near $\varepsilon = 0$, the dimensional circulation is higher in channels with lower α (as illustrated by the inset images). However, in dimensionless form Γ_{Dean}/Uw is higher for $\alpha = 1.1$ and 2.4 than it is for $\alpha = 0.57$ and 0.45, even though the Reynolds number has now effectively been scaled out and a data collapse might be expected.

The insets of Fig. 4.7 show the vorticity of the flow field at $x = 0$ for $\varepsilon = -0.02$, just before the onset of the asymmetric flow. The vorticity patches shown in the insets of Fig. 4.7 give an indication of the space within the quadrant occupied by a Dean vortex. For $\alpha = 0.45$ and 0.57 the vorticity patches occupy nearly the entire quadrant. The size of the Dean vortex is set by the channel half-width $w/2$, so for $\alpha < 1$ the Dean vortices are compressed by the shallow depth and are constricted between the wall and

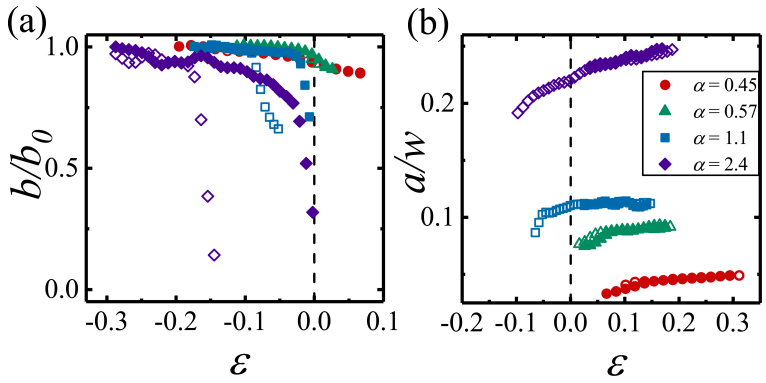

Figure 4.8: Separation distance between Dean vortex pairs as a function of ε and central vortex non-dimensional radius [1]. (a) Normalized distance between Dean vortex pairs prior to merging, b/b_0 as a function of ε. (b) Normalized characteristic radius a/w of the single merged vortical structure as a function of ε. Closed/open symbols represent increasing/decreasing Re steps.

the counter rotating vortices. By contrast, for higher α >1, the vorticity patches are localized near the walls at $z = \pm d/2$, occupy a space that is smaller than the quadrant, and are therefore less spatially confined.

The center position of the merging Dean vortices X^c is calculated from the velocity field as follows [102]:

$$X^c = \frac{1}{\Gamma_{Dean}} \int_0^{\pm\frac{w}{2}} \int_0^{\pm\frac{d}{2}} X\omega_x dz dy, \tag{4.2}$$

where X is the coordinate within the quadrant containing the vorticity ω_x. After finding the center position of each Dean vortex for each imposed Re, the distance between the two merging vortices (b) is computed by subtraction. The parameter b/b_0 is plotted as a function of ε in Fig. 4.8 (a), closed and open symbols refer to vortex merging (increasing ε) and splitting (decreasing ε), respectively.

In low aspect ratio channels ($\alpha < 1$), we observe that the approach of the dominant Dean vortex pair with increasing ε is very gradual and actually continues beyond the onset of symmetry breaking. Merging into a single central vortex occurs after displacement of the Dean vortices through a relatively short distance ($\approx 0.1 b_0$). Since the Dean vortices are relatively close to each other even in the symmetric state (see insets of Fig. 4.7), merging occurs for a relatively small displacement of the cores.

For the deep channels with ($\alpha > 1$), the two merging Dean vortices show an initially gradual approach as ε is increased but then rapidly merge into a single structure at $\varepsilon = 0$. In these cases, the Dean vortices are more widely separated in the symmetric flow state (see insets of Fig. 4.7), so must displace a considerable fraction of their maximal separation b_0 before merging occurs.

Apart from the vortex merging process, our experimental system allows the controlled study of vortex splitting. As mentioned in the introduction section 1.2.2, studies on the dynamics of splitting vortices are scarce. The vortex flow field in the first experimental observation of vortex splitting [104, 105] resemble that in our own experiments

(see Fig. 4.5). Additional reports suggest that merging and splitting events in arrays of counter-rotating Dean vortices are associated with the spacing between vortex pairs and are affected by centrifugal instabilities [107].

Yet in all of the previous studies mentioned above, the control over the experimental conditions was limited. Additionally, the previous studies involved stacks of multiple vortices that exhibit complex interactions [104–107]. By contrast, in our experimental setup, a single vortex is isolated at a fixed location and forced to split in a controlled fashion by a simple manipulation of the Reynolds number.

In our experiments, we are able to measure the separation between vortices as we reduce Re in a finely controlled manner, as demonstrated by the open symbols in Fig. 4.8 a. For the low α channels the merging and splitting processes are clearly reversible as the curves follow the same path. However, for $\alpha = 1.1$ and 2.4, the vortex splitting occurs for lower values of ε than vortex merging. This is due to the hysteresis in the flow that permits the existence of a central vortex for $g^2/4k < \varepsilon < 0$.

Once the dominant Dean vortex pair has merged into a single central vortex, we can continue our analysis by tracking the size of the vortex core as a function of the imposed ε. The characteristic radius of the central vortex core is evaluated from the second moment of vorticity [102]:

$$a^2 = \frac{1}{\Gamma} \int_{-\frac{w}{2}}^{\frac{w}{2}} \int_{-\frac{d}{2}}^{\frac{d}{2}} \mid X - X^c \mid^2 \omega_x dz dy. \tag{4.3}$$

The vortex core radius is normalized by the characteristic length scale w and is plotted as a function of ε in Fig. 4.8 b. For increasing Re ramps, the plots show how the radius of the central vortex core increases with increasing ε, starting from the value at which the merging process is completed and the central vortex is formed. For $\alpha = 0.45$ and 0.57, the growth and reduction of the central vortex radius follow the same curve. However for $\alpha = 1.1$ and 2.4 the curve for reducing Re is prolonged to negative values of ε and smaller values of a/w due to the hysteresis in the flow. As α is increased, the central vortex occupies a greater portion of the channel width w. However, the size of the central vortex is not limited simply by w since the vortex can actually impinge into the channel inlets (as reported previously [27] and demonstrated by the inset in Fig. 4.5 d where Re = 30.2). This implies that the central vortex size is limited by d, the depth of the channel. Therefore, higher values of α enable relatively larger, more intense vortices to be formed, while low α suppresses vortex growth and intensification.

4.3 Dynamic experiments

In this section, we will describe the dynamic flow experiments in which we impose a large step increase or decrease in Re across the critical value and observe the time evolution of the flow as it approaches the steady state. We begin by presenting the time dependence of the symmetry breaking flow instability before describing the dynamics of the associated vortex merging and splitting processes.

4.3.1 Dynamics of the flow transition

Time dependent experiments are conducted by imposing a single step increase or decrease in Re from an initial value Re_i to a final value Re_f across the transition, as described in the Methods, Section 2.4.2. This results in an instantaneous change in the free energy of the system F. We follow ψ as it subsequently evolves in time towards equilibrium in one of the new potential wells (Fig. 4.6).

For time dependent experiments, the initial and final imposed control parameters are defined as $\varepsilon_i = (\mathrm{Re}_i - \mathrm{Re}_c)/\mathrm{Re}_c$ and $\varepsilon_f = (\mathrm{Re}_f - \mathrm{Re}_c)/\mathrm{Re}_c$, respectively.

For increasing Re steps, we begin with an initial $\mathrm{Re}_i < \mathrm{Re}_c^*$ and end with a final

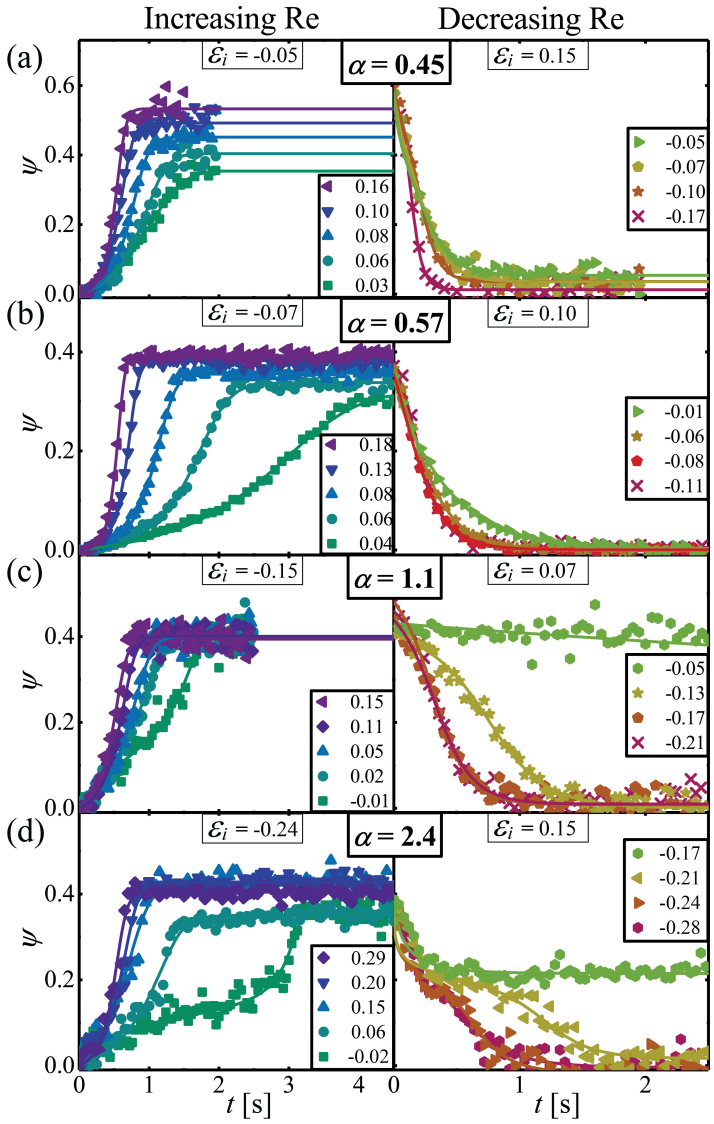

Figure 4.9: Time dependence of the ψ for all four aspect ratios [1]: (a) $\alpha = 0.45$, (b) $\alpha = 0.57$, (c) $\alpha = 1.1$, (d) $\alpha = 2.4$. Experiments are done for various values of ε_f, indicated in the legends. The data are fitted with the dynamic form of the Landau model (Eq. 4.4). (Left) Increasing Re steps, and (right) decreasing Re steps.

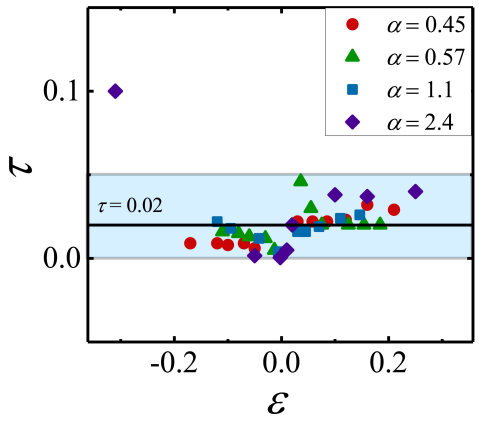

Figure 4.10: The parameter τ is extracted from the dynamic Landau model fit and plotted with ε_f (SI-[1]). τ remains positive throughout the fittings and is nearly constant.

$\mathrm{Re}_f > \mathrm{Re}_c^*$. The left-side column of 4.9 shows ψ plotted as a function of time (t) for an increasing Re step, from ε_i (indicated in the figure) to ε_f which is specified in the legend. For experiments involving decreasing Re steps, we begin from an initial $\mathrm{Re}_i > \mathrm{Re}_c$ and reduce to a final $\mathrm{Re}_f < \mathrm{Re}_c$ (i.e., $\varepsilon_f < 0$ including values within the hysteresis regions). The curves showing $\psi(t)$ for decreasing ε experiments are plotted in the right-side column of Fig. 4.9, where again ε_i is indicated in the figure and the various values of ε_f imposed at each aspect ratio are indicated in the legends. The solid lines in Fig. 4.9 are fits to the data using a dynamic form of the Landau model [50]:

$$\tau \frac{d\psi}{dt} = -\frac{dF}{d\psi} = \varepsilon\psi - g\psi^3 - k\psi^5 + h, \tag{4.4}$$

where τ is the characteristic time.

In order to reduce the number of free parameters, k was set to be equal to 1. The parameters g, h, ε and τ which represent the extent of hysteresis in the transition, channel imperfections, Re and the time constant, respectively, were left free. As is evident from Fig. 4.9 Eq. 4.4 provides an excellent description of the relaxation dynamics observed in our experiments at all α and ε_f.

The parameter h was found to vary insignificantly between experiments, and it shifts only slightly from the value originally found in the quasistatic experiments (see Table 4.1). The maximum deviation from the quasistatic h value is 0.1%. This indicates that h is independent of ε and only depends on the imperfections of a specific channel.

The parameter τ was found to remain nearly constant between $0 \leq \tau \leq 0.05$ throughout the experiments, for all α. A plot of τ as a function of ε is shown in Fig. 4.10.

In Fig. 4.11 a and b, plot of the parameters ε_f and g are presented as a function of ε for each of the four tested aspect ratios.

The value of Re_c found in the quasistatic experiments is very similar to the value of Re_c that is retrieved from curve fitting of the dynamic Landau model for the time dependent experiments. Therefore the relation between ε and ε_f is linear (Fig. 4.11 a).

A shift from the linear trend is seen for $\alpha = 2.4$ and for $\alpha = 1.1$ (purple and blue symbols in Fig. 4.11 a) where the value of ε is strongly affected by the hysteresis and where the critical value to regain symmetry is no longer Re_c but is now Re_c^*.

The parameter g increases linearly, passing through the origin, with the increase in ε. A slight shift from the linear trend is seen for the $\alpha = 0.45$ (red symbols in Fig. 4.11 b). This can be explained by the linear approximation that is performed for the parameter ε_f and according to the theory should slightly curve, keeping a linear relation with g. The linear trend of the parameter g was also observed in the experiments done with the Taylor-Couette configuration [196].

For increasing steps in ε (Fig. 4.9, left), the results are in general accordance with the quasistatic flow curves in Fig. 4.5 and the steady state value of ψ grows as the imposed ε_f is increased. For the subcritical transitions, we note some interesting cases, e.g., for $\alpha = 2.4$ at $\varepsilon_f = -0.02$, where ψ appears to settle at an intermediate metastable value for $1 \lesssim t \lesssim 2.5$ s before eventually increasing to the final steady state value. The intermediate and final values of ψ are approximately consistent with the values found on the lower and upper branches within the hysteresis loop shown in Fig. 4.5 d at the same $\varepsilon = \varepsilon_f =$ -0.02. Despite the resulting complex time evolution of ψ , Eq. 4.4 captures the dynamics in a very precise manner.

From the plots in Fig. 4.9 (left) it is apparent that the transition becomes prolonged as ε_f is decreased. This can be explained by the shape of the Landau potential. For small values of ε_f, the new potential wells that form are shallow and therefore F at $\psi = 0$ is nearly flat, which causes ψ to evolve slowly. A larger ε_f results in deeper potential wells with steeper slopes near $\psi = 0$ which cause the transition to occur faster. This trend is seen for all values of α that are studied here; however, the slowdown in the dynamics of the transition is most prominent near the tricritical point [i.e. for $\alpha = 0.57$ as $\varepsilon_f \to 0$, Fig. 4.9 b]. Similar behaviors have also been reported for flow transitions near critical points in the Taylor-Couette geometry [196, 204].

The right-hand side of Fig. 4.9 shows the evolution of ψ as ε is decreased from $\varepsilon_i > 0$ to $\varepsilon_f < 0$. From these plots it is seen that for lower aspect ratios (Fig. 4.9 a and

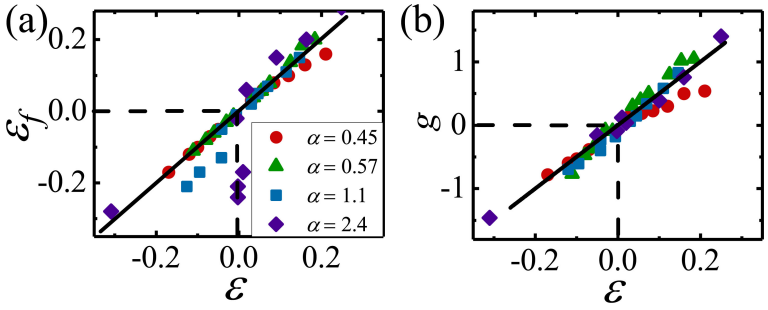

Figure 4.11: Landau model parameters extracted from the dynamic model fits (SI-[1]). (a) The parameter ε_f is plotted as a function of the parameter ε obtained from the fit with the dynamic Landau model. The solid line is a linear fit to the data showing that the free parameter ε remains similar to the original critical value obtained from the quasistatic experiments. (b) The parameter g is plotted as a function of ε. The solid line is a linear fit to the data.

4.9 b) the transition back to symmetry (i.e. $\psi = 0$) occurs faster than the symmetry breaking even as $\varepsilon_f \to 0$. This can again be explained simply by considering the change in shape of the Landau potential, which changes directly from having two minima to having a single minimum as ε_f is decreased below the critical value (see insets in Fig. 4.6). For the subcritical transitions at higher aspect ratios (Fig. 4.9 c and 4.9 d) where hysteresis emerges, the process of regaining symmetry is more complicated, as seen by the convoluted curve shapes. For values of $-g^2/4k < \varepsilon_f < 0$ that lie within the hysteresis loop, the Landau potential develops three minima (see Fig. 4.6) and it is possible to remain at a high value of ψ in a stable or metastable state.

Figure 4.12 shows the flow fields measured in dynamic experiments for three different cases of a subcritical transition ($\alpha = 2.4$). For an increase in ε from $\varepsilon_i = 0.24$ to $\varepsilon_f = 0.06$, Fig. 4.12 a shows how the flow field breaks symmetry at $t > 0$ and evolves to a stable asymmetric field with a fully developed central vortex. This set of figures correspond with the plot shown in Fig. 4.9 d, where $\varepsilon_f = 0.06$ (turquoise circles). The evolution of the flow for a reduction of ε from $\varepsilon_i = 0.15$ into the hysteresis region is shown by the images in Fig. 4.12 b, where $\varepsilon_f = -0.17$. Here, the flow field evolves from stable central vortex at $t = 0$ s to a smaller central vortex at $t = 0.25$ s and finally to an even smaller vortex at $t = 1$ s that subsequently remains stable and steady in time. This set of figures corresponds with the plot shown in Fig. 4.9 d, where $\varepsilon_f = -0.17$ (bright green symbols). Regaining of symmetric flow, from an initially asymmetric state at $\varepsilon_i = 0.15$ is illustrated by Fig. 4.12 c, for $\varepsilon_f = 0.28$ (corresponding to the dark red symbols in Fig. 4.9 d). Here we can see how the flow field is transformed from a fully developed central vortex back to a symmetric state within ≈ 1 s.

In Sec. 4.3.2, we will focus on analysing the dynamics of confined merging vortices and the opposite process in which a single vortex splits into two vortices.

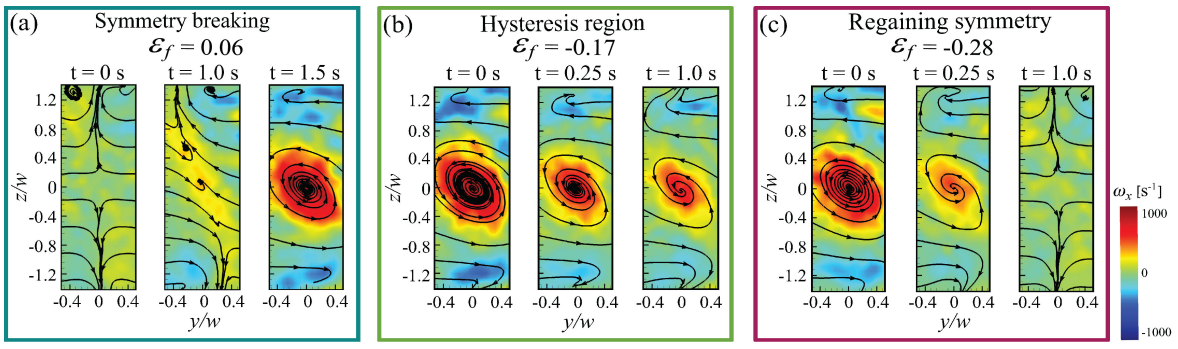

Figure 4.12: Evolution of vorticity fields observed in the center plane ($x = 0$) of a cross-slot device with $\alpha = 2.4$ [1]. (a) Symmetry breaking and formation of a central vortex are captured for an increase from ε_i = -0.24 to $\varepsilon_f = 0.06$. (b) Decay of a central vortex for a reduction from $\varepsilon_i = 0.15$ to ε_f = -0.17 (within the hysteresis loop). (c) Regaining of symmetric flow for a reduction from $\varepsilon_i = 0.15$ to ε_f = -0.28. The colored frames surrounding the sets of images correspond to the data sets shown in Fig. 4.9 d.

4.3.2 Dynamics of vortex merging and splitting

The normalized separation distance between vortices b/b_0, is plotted as a function of dimensional time in Fig. 4.13. The left hand side of Fig. 4.13 shows the data for increasing Re experiments during the process of merging. The right hand side of Fig. 4.13 shows the opposite experiments where a step decrease in Re causes the single central vortex to split into two Dean vortices that migrate away from each other towards the channel walls.

We notice that for $\alpha = 0.45$ and 0.57 the range of movement of the Dean vortices prior to merging is $\approx 0.1b_0$ (Figs. 4.13 a and 4.13 b), similarly to the finding in the quasistatic experiments shown in Sec. 4.2. For $\alpha = 1.1$, the range of movement is $\approx 0.5b_0$ (Fig. 4.13 c), while for the highest aspect ratio $\alpha = 2.4$, we observe that the Dean vortices pass through an even larger relative distance $\approx 0.7b_0$ before merging (Fig. 4.13 d). The merging process that is seen for $\alpha = 1.1$ and $\alpha = 2.4$ has a qualitative

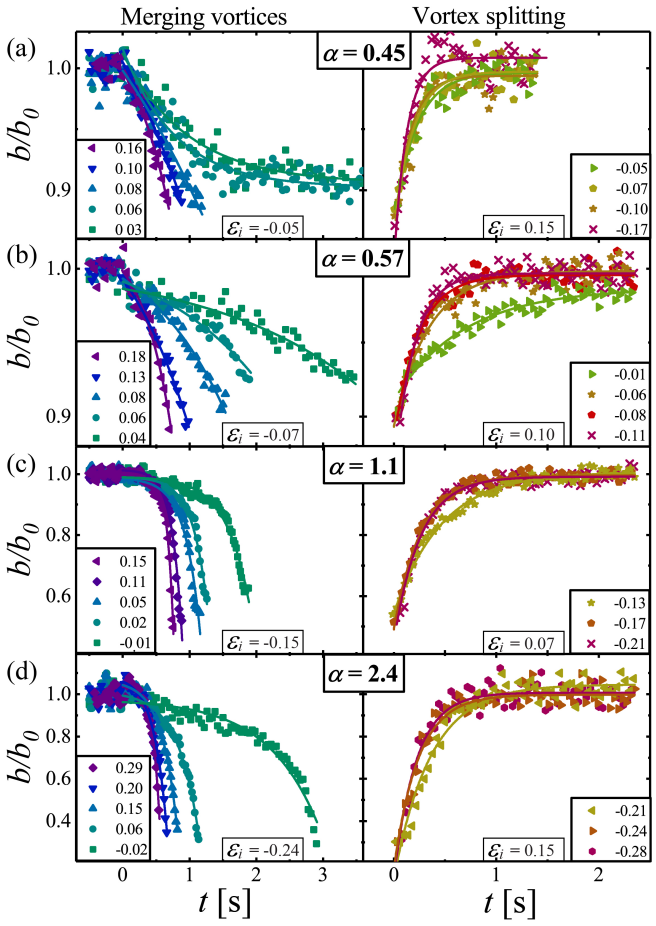

Figure 4.13: Normalized distance between the center position of merging and separating Dean vortices (b/b_0) as a function of time for four aspect ratios [1] ; (a) $\alpha = 0.45$, (b) $\alpha = 0.57$, (c) $\alpha = 1.1$, (d) $\alpha = 2.4$. Experiments are performed for step increases (left) and decreases (right) in ε_f which is indicated in the legend. Solid lines correspond to exponential curve fitting.

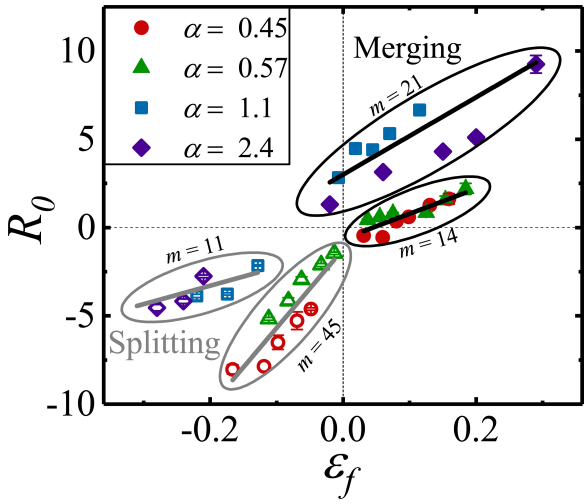

Figure 4.14: R_0 as a function of ε_f [1]. R_0 is extracted from the exponential fits to the data in Fig. 4.13 a. The solid lines are linear fits to the data, where m is the slope. Merging data are located in the upper right quadrant; splitting data are located in the lower left quadrant.

similarity to previous studies in which the vortices are not confined [93, 94, 200–202, 205].

Since the experimental system enables control of the initial and final Re, we are able to capture unique cases in which the vortices are in the process of merging but never fully merge, due to the balance achieved between inertial and viscous forces at the final Re_f. Examples for this equilibrium state within the vortex merging process can be seen for two experiments with the channel $\alpha = 0.45$ for which $\varepsilon_f = 0.03$ and $\varepsilon_f = 0.06$ (as shown in the left side of Fig. 4.13 a). By fixing Re_f in the dynamic experiments, we are also able to arrest the process at any given stage while remaining under constant flow. This can potentially enable a very detailed study of the flow field during merging and splitting of vortices.

In order to get further insight about the effects of confinement on the dynamics of the merging process we performed curve fitting to the plots in Fig. 4.13 at different aspect ratios.

All of our experimental data sets (for vortex merging and splitting) are well-described by a simple exponential of the form $b/b_0 = 1 + Ae^{R_0 t}$ where A is a constant and R_0 is the rate of the exponential growth. Note that vortex merging has been described as an exponential process in various previous studies [41, 99, 206–209].

The parameter R_0, is extracted from the fit and plotted as a function of ε_f in Fig. 4.14. From our results, it is seen that the rates of both the merging and the splitting processes are linearly dependent on the imposed Re_f, with an apparent change in slope at the critical point. Considering first the merging process, at all aspect ratios we observe faster merging for higher ε_f. This is in agreement with previous experiments which measured the time taken for vortices to merge for different initial imposed Re [92].

For a given ε_f, merging rates are faster in high α devices compared to the low α channels. Now, considering the splitting process, we observe the opposite trend, i.e.,

faster splitting in low α channels than in high α channels (for a given ε_f).

Considering only the low α channels, it is apparent that, equidistant from the critical point, the merging is significantly slower than the splitting of vortices. The opposite is true for high α channels, where merging proceeds at a faster rate than splitting.

The contrasting dynamics can be attributed to the higher value of Γ_{Dean}/Uw (see Fig. 4.7) that leads to stronger attraction between Dean vortices in high α channels. Hence the vortices in high α channels are relatively quick to merge but relatively slow to separate in comparison with lower α channels. This disparity provides a basis for understanding the hysteresis in the flow transition observed in the higher aspect ratio channels.

Confining vortices by reducing the channel aspect ratio forces them to be in an "unnatural" constricted environment. At higher aspect ratios, the vortices are less confined, show a more natural circular shape and gain further spatial freedom. Consequently, we can expect that in an un-confined system (for instance in aerodynamics or geophysical flows), the splitting dynamics will be slower than that of merging.

In Sec. 4.3.3, we will discuss the relation between the onset of the flow instability and regaining of symmetry with the merging and splitting of vortices.

4.3.3 Relation between flow instability and vortex dynamics

Here, we present the relation between the order parameter ψ which and the distance between the merging and separating Dean vortices b.

For each α, the plots of ψ as a function of $1 - b/b_0$ are presented in Fig. 4.15 for a wide variety of ε_f. In general, there is a good collapse of the data at each aspect

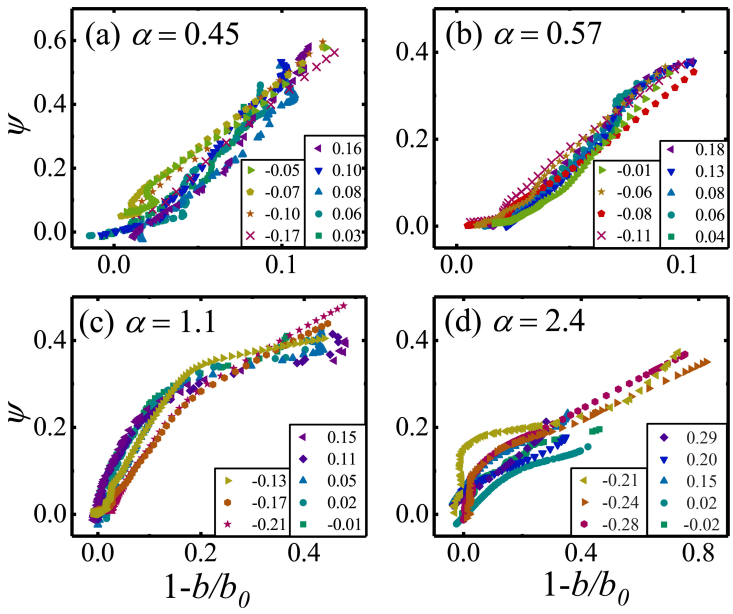

Figure 4.15: Relation between the order parameter ψ and the distance between merging Dean vortices b/b_0 [1]. The data plots show both increasing and decreasing Re steps experiments, ε_f is indicated in the legend. Supercritical transition (a) $\alpha = 0.45$ and (b) $\alpha = 0.57$. Subrcritical transition (c) $\alpha = 1.1$ and (d) $\alpha = 2.4$.

ratio, clearly showing the inter-relation between the two quantities and suggesting that ψ depends only on the distance between Dean vortices, independently of the history of the system. The relation between ψ and $1 - b/b_0$ is solely affected by the value of α, which determines the extent of confinement and the initial distance of the vortices from each other.

For the different transition types we see a different trend. For the supercritical transition, ψ shows a general linear change with $1 - b/b_0$ with an apparently α-dependent slope (Fig. 4.15 a and 4.15 b). However, for subcritical transitions the relation between the parameters is non-linear (Fig. 4.15 c and 4.15 d).

In the high α channels we can see that initially, ψ changes rapidly as a function of the distance between the vortices. As the vortices approach each other, there is a change in slope and ψ increases more moderately while the distance between the vortices decreases rapidly.

We interpret these two regimes as corresponding to the diffusive and convective stages of the merging and splitting processes. The general linear relation between ψ and $1 - b/b_0$ for low α channels suggests the absence of one of the stages in merging and splitting in these more confined cases. Since the vortices only move through a relatively short distance in these low α cases, we conclude that the confinement results in a dominant diffusive stage and the absence of an observable convective stage.

4.4 Summary

In this chapter, we have examined the vortex dynamics associated with a symmetry breaking flow instability that occurs beyond a critical Reynolds number in a 4-way intersecting flow. At low Re, the flow in the cross section of the intersecting region is symmetric and composed of four cells of Dean vortices. As Re is increased beyond the onset of bifurcation, one pair of diagonally opposed Dean vortices intensifies and begins to approach each other, ultimately merging to form a single vortex located on the channel centerline. By a subsequent reduction of Re, the opposite process can be induced in which a single vortex splits into two co-rotating vortices that migrate away from each other. While vortex merging has been studied extensively, the process of vortex splitting is much more challenging to induce and study. Here, by careful manipulation of the imposed Reynolds numbers in quasistatic and dynamic experiments, we are able to easily induce both the merging and splitting processes while keeping the system under a well-controlled constant steady flow. Furthermore, we can arrest the dynamics at any desired stage, permitting a detailed study of the complex flow fields and vortex interactions.

Our dynamic experiments show that the process of merging and splitting is exponential with a rate R_0 that depends linearly on the imposed Reynolds number and also depends on whether the vortices are merging or separating. By changing the aspect ratio (α) of the channels leading to and from the intersection, we vary the degree of confinement of the four Dean vortices in the symmetric flow state, which has a significant effect on the rates of vortex merging and splitting. For channels with lower values of α, the Dean vortices are tightly confined within quadrants of the channel cross section. This results in a relatively slow rate of vortex merging compared with

splitting and reversibility of the flow transition. By contrast, for channels with higher α, the Dean vortices are relatively widely spaced and unconfined. In this case, we find a faster rate of merging than of splitting. The change in the relative rates of vortex merging and splitting as α is varied provides a rationalization for the emergence of hysteresis in the symmetry breaking transition at higher values of α [27].

The symmetry breaking and the vorticity dynamics are intimately linked, and our order parameter that describes the degree of flow asymmetry is shown to depend only on the separation distance b between Dean vortices, independent of Re or the history of the system. The relation between ψ and b is linear for low α channels (supercritical transitions, for which only a slow diffusive merging and splitting are observed) but is non-linear for the more complicated hysteretic subcritical transitions in higher α channels (for which both slow diffusive and fast convective stages are seen). Our results are clearly relevant to understanding and predicting flow transitions associated with the merging and splitting of vortices in confined environments such as pipe flows, microfluidics, and biological flows within veins and arteries. Our discoveries may also benefit the understanding of vortex dynamics in general, particularly, with regard to the turbulent energy cascade and the prediction of vortex behavior and interactions in geophysical flows.

Chapter 5

Vortex structure and periodic flow fluctuations

In this chapter, the Re $-\alpha$ phase diagram is further explored by increasing Re well beyond Re_c. We study the changes in the flow field under different confinement conditions and how confinement affects the properties of the central vortex and its dynamics. The main findings from this chapter indicate that by tuning the confinement parameter, α and Re, it is possible to control vortex properties such as its intensity and core structure. Additionally, it is shown that the vortex type at the steady state will determine the nature of the unsteady fluctuations that arise upon an increase in Re.

5.1 Introduction

Periodic flow patterns commonly occur, upon a critical flow rate, when the fluid is interrupted by an obstacle, around which stagnation points are formed [19]. As briefly mentioned in the general Introduction in Chapter 1, the resulting motion, vortex induced vibration, may be destructive for structures such as bridges, pipes, buildings and underwater cables [19, 20]. Vortex induced vibration is one of the major issues in the engineering of deepwater risers for oil and gas production and many efforts have been made to suppress it [210]. In order to avoid vibrations of such underwater pipes, they are often fitted and covered with small structures, that are designed to stabilize the flow and control the vortex induced motion [211–213].

In recent years, vortex induced vibration is being acknowledged as a source for renewable energy from fluid flows [9, 21]. Vortex induced vibration is described as a high energy phenomena and is already in use for energy harvesting from ocean currents at high Re ($10^4 < \mathrm{Re} < 10^5$) [214].

The stagnation point flow in the cross-slot geometry, becomes unstable and unsteady at relatively low Re and can potentially offer improved conditions for energy harvesting by vortex induced vibrations. The control over the flow instability and vortex formation in the cross-slot geometry was thoroughly studied in the Chapter 4. In this chapter, vortex types and properties will be further characterized. Additionally, it will be shown that the nature of periodic vortex flows is affected by the vortex type and can be controlled by flow confinement.

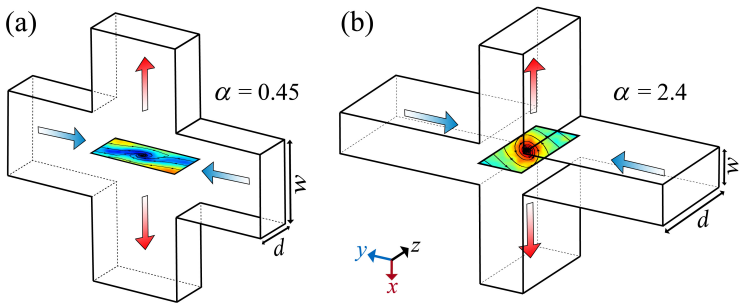

Figure 5.1: Schematic diagrams demonstrating cross-slot devices with (a) highly confined (low aspect ratio $\alpha = d/w = 0.45$) and (b) moderately confined (higher aspect ratio $\alpha = d/w = 2.4$) vortices. Inflow (along y) and outflow (along x) are indicated by the blue and red arrows, respectively.

The cross-slot intersections that are studied in this chapter are selected as they are located at the two opposite ends of the Re $-\alpha$ phase diagram presented in Chapter 3 Fig. 3.7. The first geometry is a low aspect ratio cross-slot device, $\alpha = 0.45$ (Fig. 5.1 a) with a distinct supercritical transition, the second is a high aspect ratio cross-slot device, $\alpha = 2.4$ (Fig. 5.1 b) with a distinct subcritical transition. In Chapter 4 the transition to unstable flow and its dynamics are discussed in detail. Briefly, for low aspect ratio, stabilization of the flow occurs due to the close proximity of the walls located at $z = \pm d/2$, leading to slower dynamics of the transition and determining its type (super rather than subcritical). Higher aspect ratio cross-slot devices allow greater spatial freedom, therefore a vortex will grow and intensify at relatively low Re. It should be noted that the central vortex that is formed at $\alpha = 0.45$ is fully contained within the borders of the outlet channel (the $y - z$ plane), however, the vortex that is formed for $\alpha = 2.4$, may occupy a larger space than that of the outlet channel, the borders of this vortex may intrude into the inlet channels (along y direction) as previously reported [1, 27].

In this chapter we will test higher values of Re, well beyond Re_c to study time dependent flows for these two contrasting cases of vortex under spatial confinement. As described in the Methods, Section 2.4, μ-PIV is used to capture image pairs of the flow field at a high rate of 500 - 1000 Hz in order to study the dynamics of the time dependent flow. For each Re studied, 100 velocity vector fields are produced and processed to present velocity and vorticity contours. In order to study the nature of the periodic fluctuations and to find the characteristics frequencies, a fast Fourier transform analysis is performed by using a Matlab code.

5.2 Results

5.2.1 Steady vortex at high spatial confinement

As shown in Chapter 4, Section 4.2.2, at an intersection with $\alpha = 0.45$ a single steady vortex will form at $\mathrm{Re}_c = 107$. According to the experimental measurements, the

central streamwise vortex persists and remains steady for a range of $107 < \mathrm{Re} < 473$. A contour plot of the velocity component v_y/U, is constructed for a steady vortex flow at $\mathrm{Re} = 446$ (Fig. 5.2 a). The velocity profile v_y/U is plotted as a function of z/w (Fig. 5.2 b). In Fig. 5.2 c, a contour plot of the vorticity, $\omega_x w/U$, is presented, showing a central counter clockwise (CCW) rotating vortex. The vorticity distribution, $\omega_x w/U$ is plotted as a function of z/w ($x = y = 0$) in Fig. 5.2 d, showing a clear single peak of $\omega_x w/U$ at the center of the $y - z$ plane, where the stagnation point is located ($x = y = z = 0$).

A vortex with a single peak in the vorticity distribution, such as the one formed in this channel, can be termed "monopolar". Monopolar vortices, do not have counter rotating vortices surrounding them. Such vortices are commonly seen in stratified fluids, as described in several studies [113, 215, 216]. Apart from the central monopolar vortex, the flow field contains two smaller vortices with the same CCW rotation which appear in the corners of the $y-z$ plane. These vortices are less intense than the central one. All vortices in the flow field remain steady in the range of $107 < \mathrm{Re} < 473$.

5.2.2 Steady vortex at a moderate spatial confinement

At an intersection with $\alpha = 2.4$ a single steady vortex will form at $\mathrm{Re}_c = 26.5$, as shown in Chapter 4, Section 4.2.2,. For this aspect ratio the steady central streamwise vortex persists over a range of $26.5 < \mathrm{Re} < 69$. Contour plots of v_y/U, are constructed for

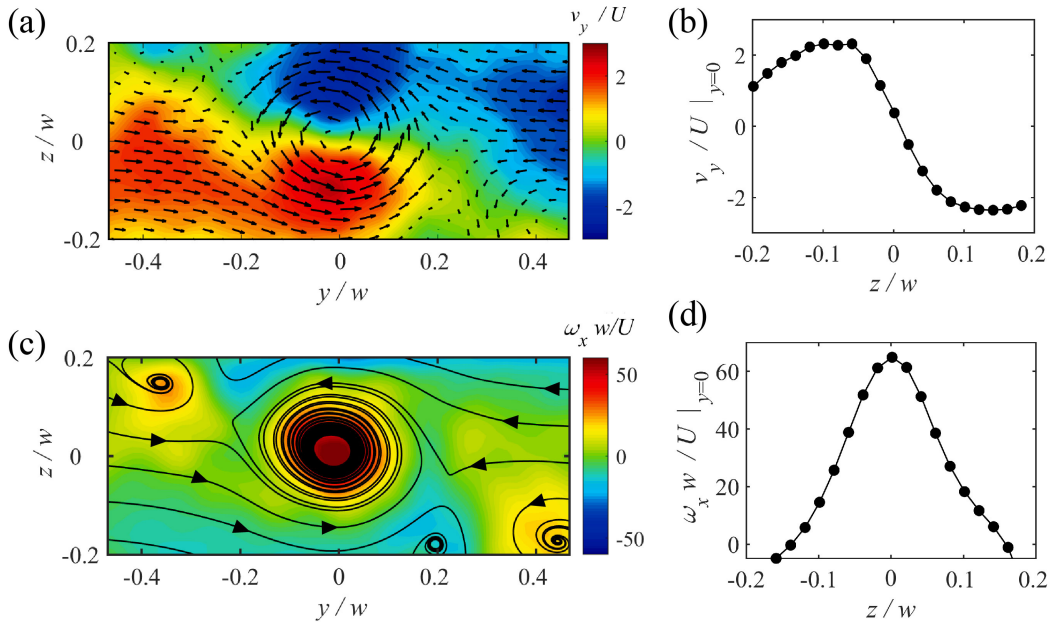

Figure 5.2: Nondimensional velocity component, v_y/U and vorticity $\omega_x w/U$ for $\alpha = 0.45$, $Re = 446$. (a) Contour plot of v_y/U at the center plane ($x = 0$) and; (b) velocity profile, v_y/U at y=0 plotted as a function of z/w. (c) Contour plot of $\omega_x w/U$ at the center plane ($x = 0$) and; (d) vorticity distribution, $\omega_x w/U$ at $y = 0$ plotted as a function of z/w.

steady flow at Re = 37 and Re = 62 (Fig. 5.3 a and b). The velocity profiles v_y/U at $32 \leq \mathrm{Re} \leq 62$ for which the flow is steady are plotted as a function of z/w in Fig. 5.3 c.

Contour plots of the vorticity, $\omega_x w/U$, are constructed for Re = 37 and Re = 62 (Fig. 5.3 d and e). A CCW vortex is seen at the center of the plane at $z = y = 0$. At the coordinate $z/w \gtrsim 0.9$ and $z/w \lesssim -0.9$ there are vorticity patches with CW rotation but there are no vortices in these regions. When comparing the vorticity field at Re = 37 (Fig. 5.3 d) and Re = 62 (Fig. 5.3 e), it is visible that the core of the central vortex changes as Re is increased. A plot of the vorticity distribution, $\omega_x w/U$ along $y = 0$ is shown in Fig. 5.3 f for $32 \leq \mathrm{Re} \leq 62$. With this plot we can identify a clear difference of the voritcity distribution when Re is increased (the vortex remains steady). At Re = 32 the vorticity distribution shows a clear single peak at the center of the $y - z$ plane, similar to the vorticity peak that is seen for the lower aspect ratio $\alpha = 0.45$ (see Fig. 5.2 d). At Re = 37, the peak flattens, and at Re = 50 and Re = 62 a clear double-peak profile is seen (Fig. 5.3 f).

As Re is increased from Re = 32 to Re = 62 the double-peak profile becomes

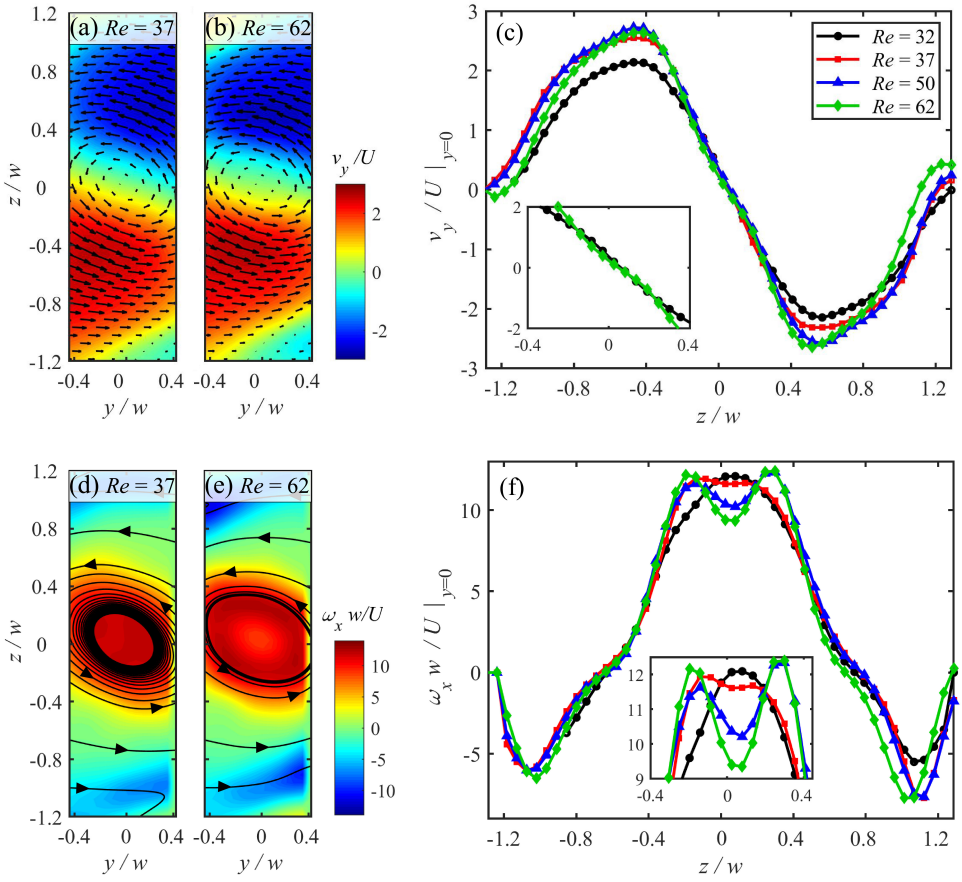

Figure 5.3: Velocity and vorticity distributions for steady flow in $\alpha = 2.4$. Contour plot of v_y/U for (a) Re = 37 and (b) Re = 62; (c) v_y/U at $y = 0$ as a function of z/w. Contour plots of $\omega_x w/U$ for (d) Re = 37 and (e) Re = 62; (f) $\omega_x w/U$ at $y = 0$ plotted as a function of z/w for different Re. Insets in c and f show the core region.

more distinct and a local minimum point is formed at $z/w = 0$. This ring of high vorticity around a lower intensity vorticity region, resembles the initial stages of an "eye" development, similar to the eye formed in hurricanes and tornadoes. Within the eye, the vorticity drops and a "wall" of high vorticity is formed around it. In these atmospheric vortices, the existence of such an eye is also Re dependent. However, in storm systems, the Re is orders of magnitudes higher than the values in our experiments and the eye structure and formation is far more complicated and affected by many factors such as humidity, heat convection and atmospheric conditions. Additionally, in such large storms the vorticity at the center of the eye can develop a counter rotating motion to that of the vorticity that is measured outside the eye [217, 218].

5.2.3 Characterization of vortex profiles

As discussed in the Introduction, Chapter 1, Section 1.2.3, there are many existing vortex models that describe velocity and vorticity profiles of vortices such as the Burgers, Lamb-Oseen, Rankine and many others [111]. However, these models can not account for the sharp decrease in the velocity profile that occurs in the case of confined vortices. Additionally, these models assume that the peak of the vorticity distribution is at the center of the vortex. Confined vortices were previously described mainly in stratified fluid layers [219] or short annulus in which the vortex is confined in both streamwise and spanwise directions. Here we will use a modified pancake-like vortex model, based on previous studies [113], to describe the velocity and vorticity profiles of the vortices in the cross-slot geometry that are confined only in the spanwise direction and are stretched at the streamwise direction.

There are several ways to define vortex size, but in order to apply the pancake model we will use the same definition used in [113]. The vortex radius $R_{v_{y,max}}$, is defined at the point where $v_y = v_{y,max}$ along z at $x = y = 0$. In Fig. 5.4 we re-scale the velocity, $v_y/v_{y,max}$ and plot it as a function of $z/R_{v_{y,max}}$ for $\alpha = 0.45$, Re = 446 (Fig. 5.4 a) and $\alpha = 2.4$, Re = 62 (Fig. 5.4 b). To use the pancake model for the vorticity distribution, ω_x along z is re-scaled with $\omega_{x,max}$. Figure 5.4 c-d shows $\omega_x/\omega_{x,max}$ plotted with $z/R_{v_{y,max}}$ for $\alpha = 0.45$ (Re = 446) and $\alpha = 2.4$ (Re = 62), respectively. These cases display Re slightly below Re_p, in which the flow field becomes unsteady.

For $\alpha = 0.45$ the peak of the vorticity distribution is at the center of the vortex (at $z/R_{v_{y,max}} = 0$). However, for $\alpha = 2.4$ ($50 < \mathrm{Re} < 69$), the peak of the vorticity is not located at the center of the vortex as demonstrated in Fig. 5.3 d-f.

In order to capture the complexity of the velocity and vorticity profiles within the core of the vortex, near $v_y/v_{y,max} = 0$, the fit equation from [113] needs an adjustment,

Table 5.1: Pancake-like vortex model fit parameters for the vortices in the cross-slot devices.

α	a_1	a_2	b_1	b_2	R_1	R_2
0.45	0.6	-	0.6	-	0.84	-
2.4	1.5	-2.0	0.84	-0.38	0.88	0.34

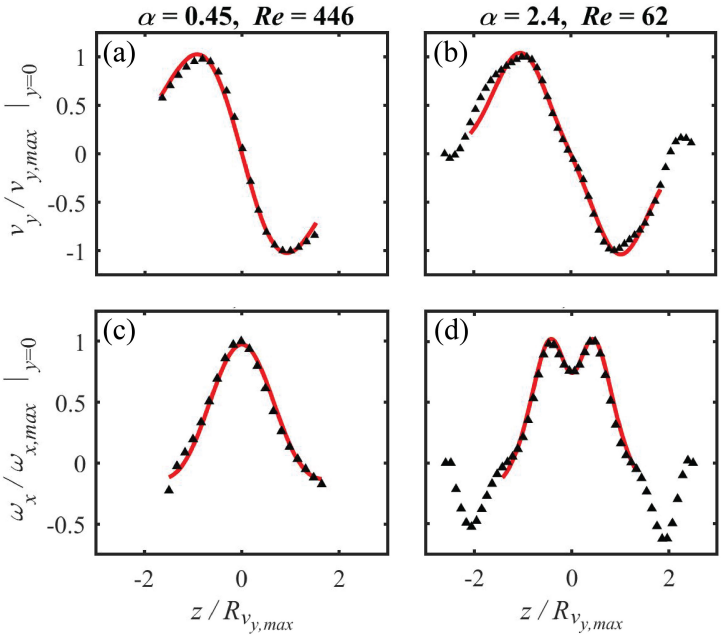

Figure 5.4: Highly and moderately confined vortices fitted with a modified pancake-like vortex model. $v_y/v_{y,max}$ plotted as a function of $z/R_{v_{y,max}}$ for; (a) $\alpha = 0.45$, Re $= 446$ and (b) $\alpha = 2.4$, Re $= 87$. $\omega_x/\omega_{x,max}$ plotted as a function of $z/R_{v_{y,max}}$ for; (c) $\alpha = 0.45$, Re $= 446$ and (b) $\alpha = 2.4$, Re $= 87$. Black triangles are data points and red lines are fits to the data described in the text.

since it can only be applied for a simple pancake vortex. Such complex velocity and vorticity profiles are not common and we could only find scarce evidence in numerical studies of fluid drainage systems [220] and for tangential wind profiles of vortices [221].

We apply modification to the model of [113], assuming that within the vortex core an additional vortex may form with a smaller diameter than that of the high intensity vorticity area surrounding it. The inner vortex may develop a counter rotating motion, similarly to the motion that is observed in large scale storms [217, 218].

The velocity profile is fitted with Eq. 5.1 (Fig. 5.4 a-b),

$$v_{y,p} = a_1(z/R_1)\ exp(\frac{1-(z/R_1)^s}{s}) + a_2(z/R_2)\ exp(\frac{1-(z/R_2)^s}{s}), \tag{5.1}$$

and the vorticity profile is described by Eq. 5.2 (Fig. 5.4 c-d),

$$\omega_x = b_1[(1-\frac{1}{2}(z/R_1)^s\ exp(\frac{1-(z/R_1)^s}{s})] + b_2[(1-\frac{1}{2}(z/R_2)^s\ exp(\frac{1-(z/R_2)^s}{s})], \tag{5.2}$$

where a_1, a_2, b_1, b_2, R_1 and R_2 are free parameters and their best-fit values by the model above, are specified in Table 5.1. For $\alpha = 0.45$ we set $a_2 = 0$ and $b_2 = 0$. The parameters a_1, a_2, b_1, b_2 are related to the orientation and intensity of the vorticity. The radii of the larger and smaller vortex are depicted by R_1 and R_2 respectively.

It was previously found that close to $s \sim 2$, the value that accounts for the steepness in the velocity profile, a pancake like vortex will become unsteady [113]. Since we are

testing cases that are close to Re_p, it is a reasonable assumption that $s \sim 2$ in our cases. In order to reduce the free parameters in the fit, we set $s = 2$ and indeed show that this value fits well for the cases studied here.

As seen in Fig. 5.4 d, Eq. 5.2 describes well the central vortex and the double peak, however it does not apply to the areas of counter rotating vorticity close to the bounding walls.

5.2.4 Periodic fluctuation at high flow confinement

For a cross-slot channel with $\alpha = 0.45$, when Re is increased to $\mathrm{Re} > 473$, the flow field loses steadiness and fluctuations appear. A high temporal resolution μ-PIV measurement of the flow field (at 500 Hz, time step between images is 0.002 s), reveals that the fluctuations are periodic with a period time of 0.016 s, for $473 \leqslant \mathrm{Re} \leqslant 543$.

We define non-dimensional time t^* by normalizing t with the average flow velocity, U and the width of the cross-slot channel, w,

$$t^* = tU/w. \tag{5.3}$$

A time series, of instantaneous contour plots of $\omega_x w/U$ are constructed from experimental data for $\mathrm{Re} = 488$ and shown in Fig. 5.5.

The nature of the fluctuation can be described as follows; at $t^* = 0$ the flow field contains a large CCW rotating vortex, the center of the vortex is located at $y = z = 0$

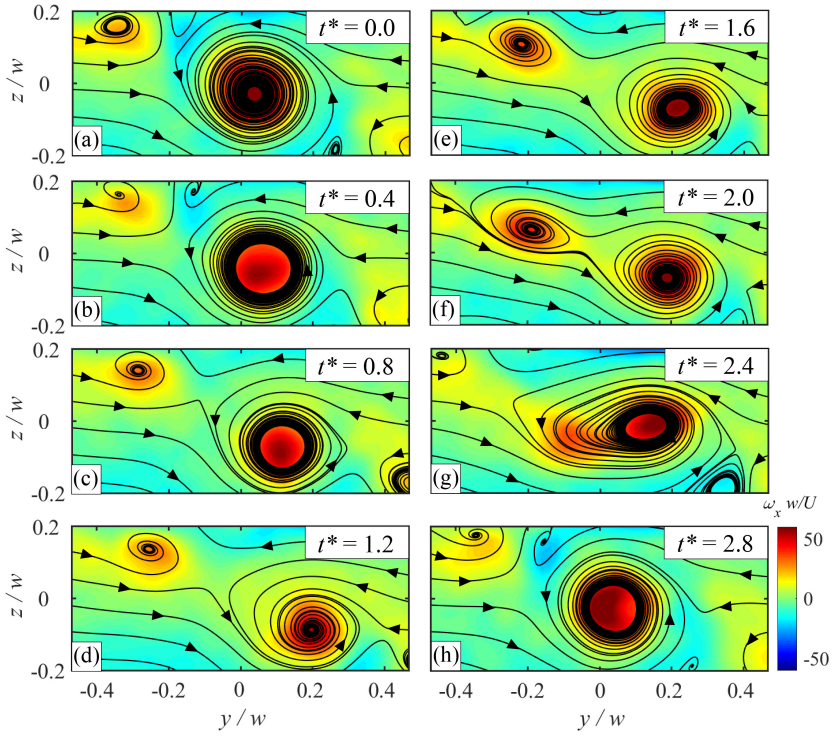

Figure 5.5: A cycle of periodic fluctuations seen for $\alpha = 0.45$, $\mathrm{Re} = 488$. Time is indicated in dimensionless form.

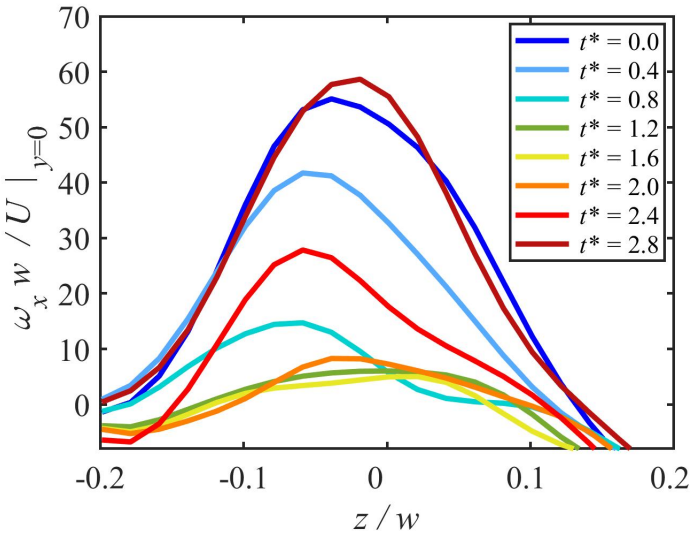

Figure 5.6: Vorticity distribution $\omega_x w/U$ along z/w of a single cycle of the periodic fluctuation for $\alpha = 0.45$ at Re = 488.

(Fig. 5.5 a). Additionally, two smaller, less intense CCW rotating vortices can be seen in the upper left ($y \simeq$ -0.35, $z \simeq 0.15$) and lower right ($y \simeq 0.4$, $z \simeq$ -0.15) corners of the $y-z$ plane.

From $t^* = 0$ to $t^* = 2.0$ the upper left corner vortex gradually intensifies as it migrates towards the center of the $y-z$ plane, simultaneously, the central vortex loses intensity and migrates towards the bottom right corner of the $y-z$ plane plane (Fig. 5.5 a-f). At $t^* = 2.0$ the two vortices begin a merging process as they share their filaments and rapidly move towards each other (Fig. 5.5 g). At $t^* = 2.8$, the final stage of the cycle, the vortices have completed the merging process as they form a single vortex at the center of the $y-z$ plane (Fig. 5.5 h). A new small vortex forms at the upper right corner of the plane.

In Fig. 5.6, the vorticity distribution $\omega_x w/U$ from the time series shown in Fig. 5.5 is plotted as a function of z/w. The cycle starts at $t^* = 0$ with a large peak at $z/w = 0$ where $\omega_x w/U > 50$ and the vortex is at the center of the $y-z$ plane. The peak intensity is gradually reduced to $\omega_x w/U < 10$, where the central vortex is at the farthest point from the center at $t^* = 1.6$. At $t^* = 2.0$, $\omega_x w/U$ along z/w rapidly increases as the vortices merge at the center of the $y-z$ plane.

For the characterization of the periodic cycles, v_y/U is extracted from the coordinates where the velocity reaches its maximal value $v_y/U{=}v_{y,max}/U$ at the point $y = 0$, $z = 0.1$ (see Fig. 5.2). At this point, the fluctuations in the flow are the strongest and the detected signal is particularly clear. A time series of v_y/U is collected from several measurements where Re is kept constant at each measurement. A range of $445 <$ Re < 543 is studied. Due to limitations of the experimental set-up we could not investigate higher Re, as our system is limited by the volume of the syringe pumps and the capabilities of the μ-PIV system (maximal frame rate of the camera is 1600 fps and the shortest time gap between laser pulses can be set to 1 μs). To experimen-

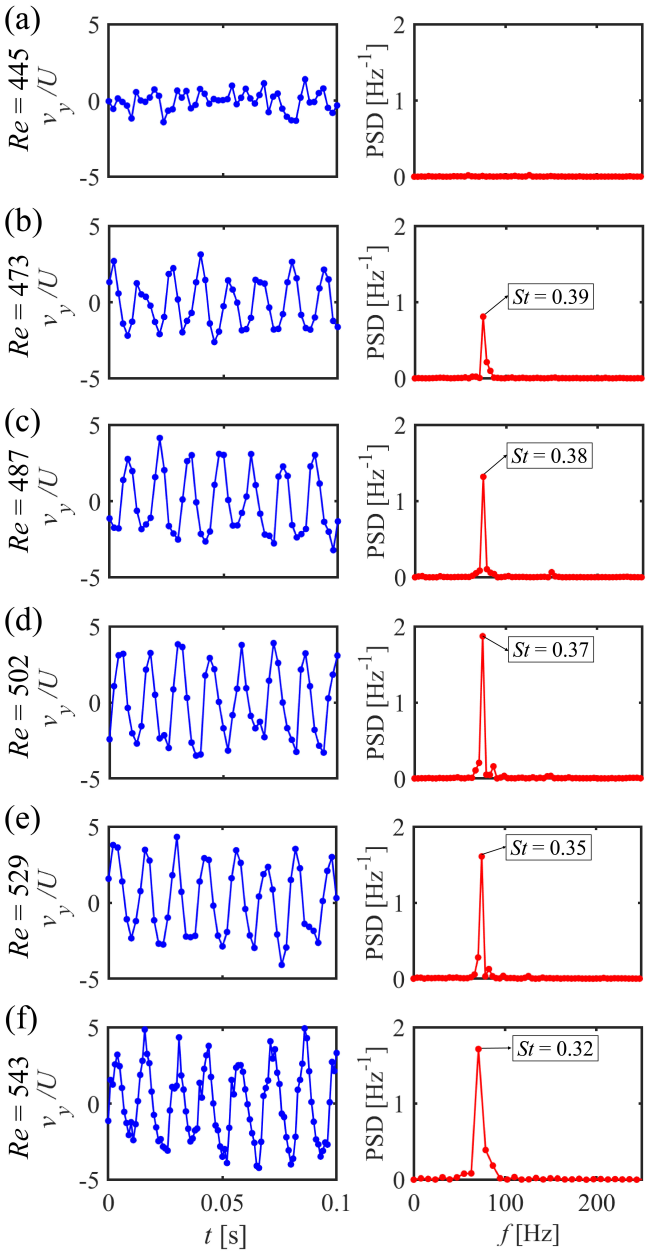

Figure 5.7: Velocity fluctuation and power spectral density are extracted for various Re from the point $v_{y,max}/U$ ($\alpha = 0.45$). v_y/U is plotted as a function of t on the left column and PSD is plotted as a function of the frequency, f on the right column for (a) Re = 445; (b) Re = 473; (c) Re = 487; (d) Re = 502; (e) Re = 529; (f) Re = 543. St is indicated in the labels.

tally study higher Re, modifications of the experimental set-up are needed (i.e., laser pulsing, camera properties, objective lens and/or channel dimensions).

In the left column of Fig. 5.7, the normalized velocity, v_y/U is plotted as a function of time, t. In order to extract the characteristic frequencies of the fluctuations, the power spectral density (PSD) is found through a Fast Fourier Transform (FFT) analysis for

v_y/U data points (plotted on the left column of Fig. 5.7). PSD is plotted as a function of the frequency f, the non-dimensional frequency, Strouhal number (St $= fw/U$) is indicated as well (plotted on the right column of Fig. 5.7). The frequency of the fluctuations remains constant at $f = 75$ Hz, so St decreases with increasing Re. The PSD, increases non-linearly with an increase in Re. However the resolution of the data might not be sufficient for further analysis of the PSD amplitude (which is indicated by a single data point).

5.2.5 Periodic fluctuations at a moderately confined flow

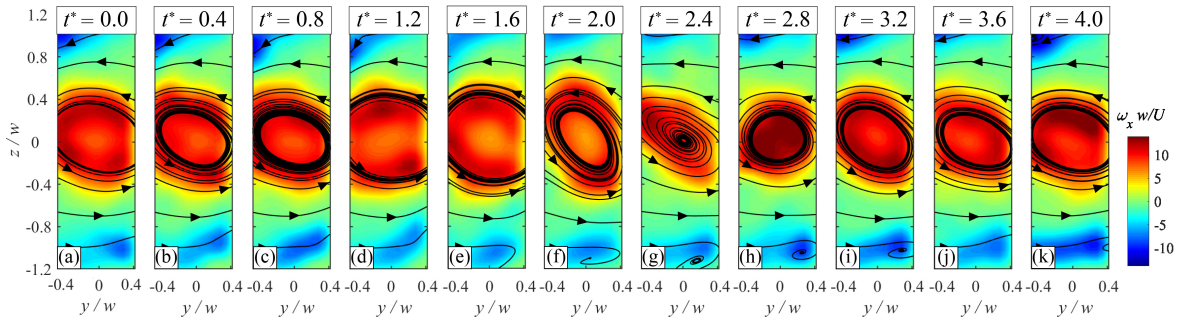

Figure 5.8: Instantaneous contour plots of $\omega_x w/U$ showing a cycle of the periodic fluctuation for $\alpha = 2.4$ and Re $= 87$. Time is indicated in dimensionless form.

Periodic fluctuations begin to emerge in the $\alpha = 2.4$ cross-slot device when Re is increased above Re $= 69$. The nature of these fluctuations is fundamentally different from those described for the case of $\alpha = 0.45$. A time series of instantaneous contour plots of $\omega_x w/U$ is shown in Fig. 5.8. Here too, the experiments are conducted at 500 Hz, with a time step of 0.002 s between two images, a full cycle of the fluctuation at Re $= 87$ is completed within 0.022 s. Time, t^* in Fig. 5.8 is indicated in dimensionless form.

The nature of the fluctuation can be described as follows; from $t^* = 0$ to $t^* = 1.6$ the central vortex maintain a large core with a distinct ring of intense vorticity around the core, the core of the vortex slightly grows (Fig. 5.8 a-e). At $t^* = 2.0$, the core structure begins to deform (Fig. 5.8 f). At $t^* = 2.4$ and $t^* = 2.8$, the vortex core shrinks to a smaller structure with an intense vorticity at its center (Fig. 5.8 g and h). At $t^* = 3.2$ the core of the vortex is reformed, the vorticity at the center of the vortex is less intense from its surrounding ring (Fig. 5.8 i). At $t^* = 3.6$ and $t^* = 4.0$ the vortex core begins to grow (Fig. 5.8 j and k).

In Fig. 5.9, the vorticity distribution along the center line (z/w) are plotted. These are taken from the contour plots shown in Fig. 5.8. From $t^* = 0$ to $t^* = 2.0$ a double-peak is seen, indicating an intense vorticity ring surrounding the core of the vortex. At $t^* = 2.4$ the double-peak is replaced by a single peak, indicating that the vortex core has lost its structure. At $t^* = 2.8$ a single peak is seen in the vorticity distribution and at $t = 3.2$ the double-peak appears, indicating that the vortex core and the surrounding ring of intense vorticity region has been re-formed.

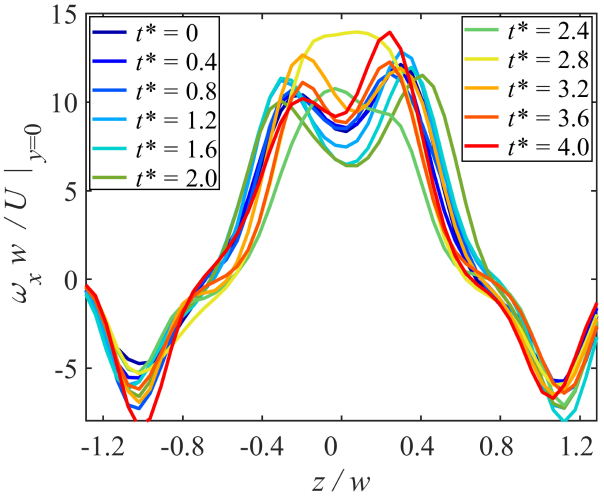

Figure 5.9: Vorticity distribution $\omega_x w/U$ of a single cycle of the periodic fluctuation for $\alpha = 2.4$ at Re = 87. Time is indicated in dimensionless form.

The left column in Fig. 5.10 shows v_y/U at the coordinate $y/w = 0$, $z/w = 0.6$, where $v_y/U = v_{y,max}/U$ and the fluctuations of the flow are the strongest (see Fig. 5.3 a). A time series of v_y/U is collected from several experiments in each of the experiments, while Re is kept as a constant. The experiments are performed for a range of $50 < \mathrm{Re} < 249$. The results are plotted as a function of time, t in the left column of Fig. 5.10. FFT analysis is conducted for the v_y/U data points presented in Fig. 5.10. *PSD* is found through FFT analysis and plotted as a function the frequency f Hz, in the right column of Fig. 5.10. The main peak that is found for each Re is indicated with the St number. Clear equally spaced harmonics peaks are also seen in the plots. The peaks in the frequency f and St are not constant and change non-linearly with increasing Re. These are plotted and further discussed in the following section.

5.2.6 Phase diagrams

Re is plotted as a function of α in Fig. 5.11 showing the onset of steady vortex flow (at $\mathrm{Re} = \mathrm{Re}_c$) and the onset of periodic vortex flow (at $\mathrm{Re} = \mathrm{Re}_p$) as found in this work and previous work. For comparison, the results from a recently reported work where the transition to unsteady flow was studied in a cross-slot channel with $\alpha = 1$ are also presented [124]. All of the studies show that the onset of periodic flows is α dependent. Due to the stabilization of the flow at low α the flow becomes unsteady only at relatively high Re_p ($\mathrm{Re}_p = 473$ for $\alpha = 0.45$ and $\mathrm{Re}_p = 300$ for $\alpha = 1$), while for high α, the flow becomes unsteady at relatively low Re_p (for $\alpha = 0.45$, $\mathrm{Re}_p = 69$). Additional data is needed for different α in order to determine what is the nature of the relation between Re_p and α.

The nature of the fluctuations that are detected for $\alpha = 0.45$ and $\alpha = 2.4$ are fundamentally different due to the initial flow field that is dictated by the confinement. For $\alpha = 0.45$ (supercritical transition to unstable flow) the flow field before the onset

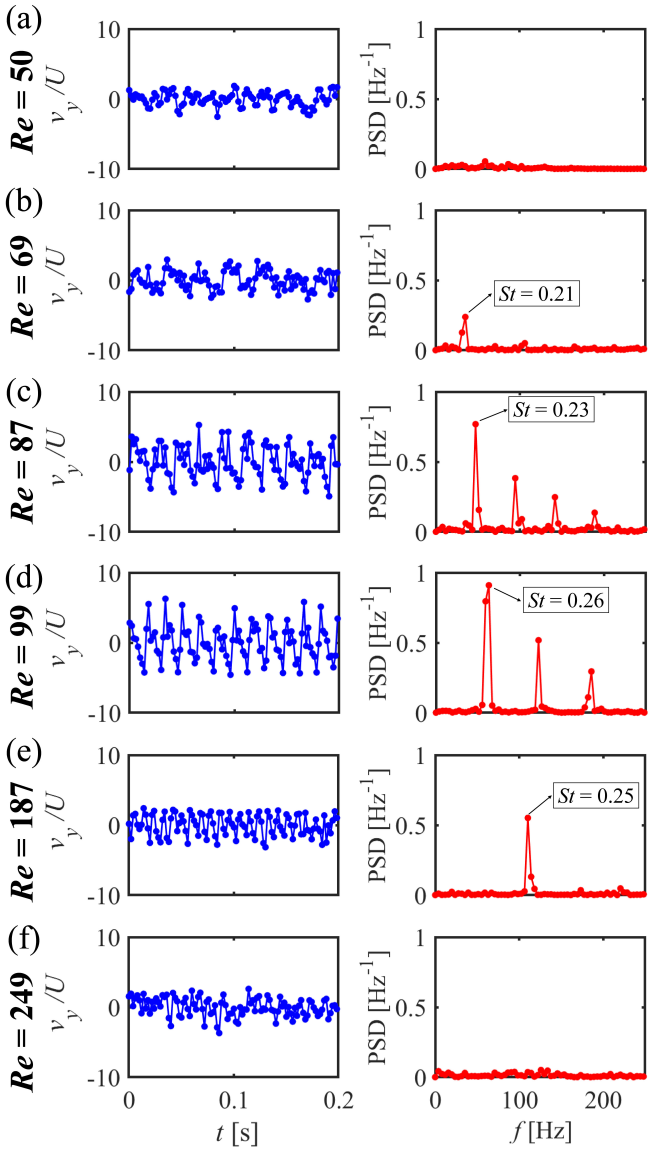

Figure 5.10: Velocity fluctuation and power spectral density are extracted for various Re from the point $v_{y,max}/U$ ($\alpha = 2.4$). v_y/U is plotted as a function of t on the left column and PSD is plotted as a function of the frequency, f in Hz on the right column for (a) Re = 50; (b) Re = 69; (c) Re = 87; (d) Re = 99; (e) Re = 187; (f) Re = 249. St is indicated.

of unsteady flow, contains a central vortex and two co-rotating side vortices (between the co-rotating vortices there are regions of counter-rotating vorticity). The flow is dominated by co-rotating vortices (this can also be seen in the high values of the order parameter plots of ψ as a function of ε that were presented in Chapter 3, Fig. 5.2 a).

For $\alpha = 0.45$ the periodic cycles include migration of the central vortex from the center to the side of the $y - z$ plane and then a merging event of the central vortex with a co-rotating side vortex that initially formed in the corner of the plane.

Interestingly, this fluctuation pattern resembles a similar periodic flow pattern that was recently reported to occur in a T-channel [119]. In their work they showed that for a T-channel with inlet aspect ratio of 1 and outlet aspect ratio of 0.5, unsteady periodic flow has emerged at $\mathrm{Re}_p = 190$. At the T-channel, the initial flow field at the plane where the outlet begins (in their work it was defined as $z/h = 1$ where h is the height of the channel and z is the coordinate along the height) has two central vortices that formed at the steady flow state. At $\mathrm{Re}_p = 190$, the central vortices migrated towards the corners of the plane and a merging of two co-rotating vortices occurred, similar to the one that is seen here for $\alpha = 0.45$. The St numbers that was found through their experiments ($0.15 < \mathrm{St} < 0.22$), and the frequency of the fluctuations are compared to the results from this Chapter in Fig. 5.12.

The same authors performed a similar investigation of the flow in a cross-slot geometry with dimensions of $w = d = 10$ mm and $\alpha = 1$ [124]. In their study they found that periodic fluctuations emerged for $\mathrm{Re} > 300$, the fluctuations were described as events of continuous merging of two co-rotating Dean vortices and splitting of the central vortex. They constructed a time series of the normalized distance between vortices l/l_{max}. However, it was not specified how this distance was measured. In their analysis, they found that the period time of the fluctuation increased with an increase in Re due to a slow down in the stage of the vortex merging. They reported that the phase in which the flow exhibited a merged central vortex remained nearly constant with a value of $\simeq 0.5$ s. It seems that the Dean vortices, in their study, were struggling to re-intensify as Re was increased, which gives a possible explanation to the slow down in the merging process that was observed. Additionally, their visualization technique, using fluorescent dye from one inlet and non-dyed fluid from the other, does not allow to capture the full complexity of the flow. Using such method allows only to resolve the flow patterns at the interface where the two inflows meet and it is not possible to resolve side vortices that are formed with the fluid from a single inlet. Therefore, they were not able to visualize the Dean vortices at the stable state. The St number that was found through their experiments ($0.06 < \mathrm{St} < 0.17$) is compared to the results

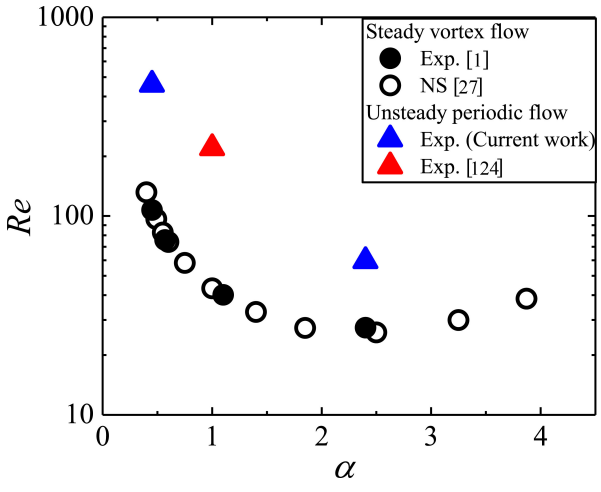

Figure 5.11: Re - α phase diagram. Re_c and Re_p are plotted as a function of α.

from this chapter in Fig. 5.12.

For $\alpha = 1$ (subcritical transition to unstable flow) the flow field before the onset of unsteady flow, also contains a central vortex and two side vortices. However, the important difference between this flow field ($\alpha = 1$) and the the flow field observed for $\alpha = 0.45$ is that the observed side vortices, at the steady state, seen for $\alpha = 1$ are counter rotating in relation to the rotation of the central vortex (the steady flow field contains CW rotating vortex and two CCW rotating side vortices). While for the case of $\alpha = 0.45$ the side vortices at the steady state are co-rotating in relation to the central vortex (the steady flow field contains three CCW rotating vortices). This difference strongly affects the nature of the fluctuations and can explain the different nature and dynamics of the periodic fluctuations.

When considering the high aspect ratio channel, $\alpha = 2.4$, the vortex maintains the initial position at the center of the geometry ($y = z = 0$) during the fluctuation cycle. The fluctuation does not exhibit vortex merging or splitting, instead, the central vortex core structure collapses and reforms.

In Fig. 5.12 a, f is plotted as a function of Re for $\alpha = 0.45$, $\alpha = 2.4$ (open symbols) and for comparison, the data for cross-slot channel with $\alpha = 1$ and a T-channel taken from [124] and [119], respectively, are also plotted (closed symbols). The data for $\alpha = 1$ and the T-channel are collected from geometries with larger characteristic length scales than the ones used here. Both cross-slot and T-shape channels have dimensions of $w = d = 10$ mm which are $\sim 10\times$ larger than the dimensions of our microfluidic channels, thus the fluctuation frequency is significantly lower [119, 124]. In order to compare with their results, the frequency found in their experiment is plotted on a secondary y axis (Fig. 5.12 a).

Figure 5.12 b, shows the non-dimensional St number plotted as a function of Re. Here the results from $\alpha = 1$ and the T-channel [119, 124] are scaled similarly to the results from the current experiments.

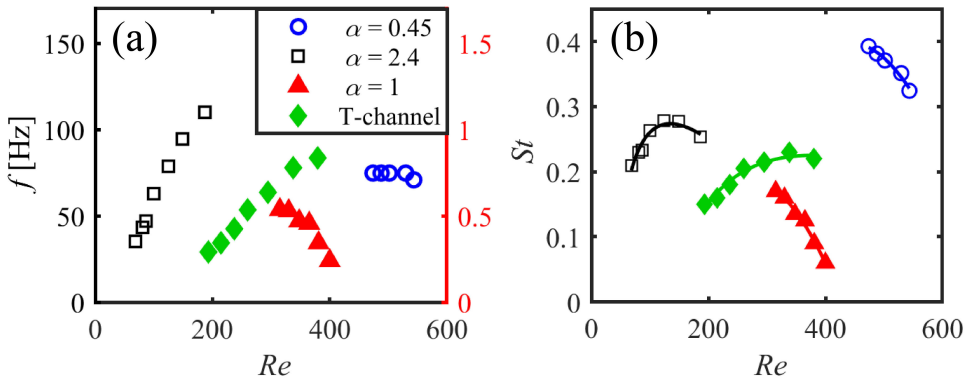

Figure 5.12: Comparison between the periodic fluctuations in cross-slot channels with different α and a T-channel. (a) f as a function of Re, the right-hand side y axis corresponds to $\alpha = 1$ and the T-channel; (b) St as a function of Re, the lines are fits to the data with Eq. 5.4; Data for $\alpha = 1$ and T-channel (closed symbols) are taken from [124] and [119], respectively.

The lines in Fig. 5.12 b are a fit with Eq. 5.4 that was previously used to describe the relation between Re and St in studies of transition to turbulence for flows around circular cylinders with different curvatures, aspect ratios and angled end plates [117, 222, 223],

$$St = x_1/Re + x_2 + x_3\ Re \tag{5.4}$$

where x_1, x_2 and x_3 are free parameters. The parameters are extracted from the fit and are listed in Table 5.2.

Table 5.2: St - Re relation, parameters extracted from fitting of Eq. 5.4

.

α	x_1	x_2	x_3
0.45	-854	4.2	-0.004
1	-340	2.5	-0.004
2.4	-20	0.6	-0.001
T-channel	-65	0.6	-0.0004

As discussed in the Introduction, Chapter 1, Section 1.2.4 (Fig. 1.3), the quadratic relation in Eq. 5.2 is used to distinguish between modes of vortex shedding in flows around circular cylinders. Periodic vortex flows at the wakes of circular cylinders are characterized by the formation of spanwise vortices, while at intersecting geometries, the flow field consists of streamwise vortices. Even-though vortex properties (i.e., spanwise or streamwise with different core structure) are strongly affected by the flow geometry, we show that the same quadratic relation can be also used for characterizing periodic flows at intersections.

Since the nature of the fluctuations is dictated by the steady flow field, the relation between Re - St are expected to be different between geometries. Describing the relation between Re and St with a quadratic equation (and retrieving the parameters from the fit) gives an initial indication that periodic flows at intersecting geometries have different modes when flow parameters are changed. Due to experimental limitation we are not able to study a larger range of Re, but even with our narrow parameter range studied, we are able to characterize our flows and to reveal the similarities between flows around cylinders and intersecting flows. Further experiments in improved spatial and temporal resolution are needed in order to find if there are different modes for the instability at each of the geometries and also in order to understand the physical significance of the parameters found by fitting Eq. 5.4 to the data.

5.3 Summary

In this chapter, vortex structure and dynamics are studied with two microfluidic cross-slot devices. The first device has a low aspect ratio ($\alpha = 0.45$) representing a highly confined vortex flow field, and the second device has a high aspect ratio ($\alpha = 2.4$) representing a moderately confined vortex flow. The same devices were used in Chap-

ter 4 where the symmetry breaking transition and vortex formation were thoroughly studied.

Our analysis shows that the vortex in the cross-slot device is similar to a Burgers vortex (stretched streamwise vortex) with an additional confinement component that was only previously reported in pancake like vortices (which are confined in both streamwise and spanwise directions).

We find that vortex confinement changes the properties of streamwise vortices at the steady state. Above Re_c, a highly confined flow field ($\alpha = 0.45$) consists of a central vortex and two, less intense, co-rotating side vortices. At this stage, the vorticity across the centerline of the vortex core, shows a single Gaussian peak that can be described by a simple pancake-like vortex model.

For a vortex that is moderately confined (in a higher aspect ratio channel, $\alpha = 2.4$) the flow field contains a single streamwise vortex (above Re_c) surrounded by a counter rotating vorticity field. At $\mathrm{Re} > \mathrm{Re}_c$, the central vortex will have a characteristic single peak in the vorticity across the core centerline (similar to the highly confined vortex at $\alpha = 0.45$). However, increasing Re (while the flow is still steady) will result in the development of a double peak in the vorticity across the core centerline, indicating on the development of an "eye" or a vorticity center surrounded by a ring of higher intensity vorticity. In order to describe this vortex we slightly modified the pancake-like vortex model to capture the complexity of the vorticity distribution at the vortex core.

Further increase of the Re, to a critical value, Re_p, will result in the onset of a periodic flow cycle. The nature of the periodic cycle depends on the vortex characteristics in the steady state. At high flow confinement ($\alpha = 0.45$) upon Re_p, the central vortex will migrate away from the center of the plane (where it was initially formed), where it will merge with one of the co-rotating side vortices in the flow field. The merged vortex will migrate back to the center of the plane and the periodic cycle will start again. At moderate flow confinement ($\alpha = 2.4$), upon Re_p, the periodic fluctuations will appear as a collapse and reformation of the vortex core, throughout the periodic cycle the position of the vortex will remain at the center of the geometry.

The characteristic frequencies of the fluctuations are found by applying FFT analysis on a velocity point in the flow field and are compared to other studies that investigated similar fluctuations in the cross-slot geometry with $\alpha = 1$ and in a T-channel. We find that the relation between St and Re is quadratic as was previously described for similar stagnation point fluctuations around circular cylinders [117, 222, 223]. We find that the relation between St and Re is non-linear and dependent on the geometry studied.

The findings of this chapter indicate on a rich periodic flow regime at cross-slot flows that can be precisely tuned by changing the parameter space (i.e., Re and α). These findings are valuable for improving the control over periodic vortex motion at stagnation points that may induce harmful vortex vibrations on structures such as bridges, pipes and buildings. Additionally, our findings can initiate new ways to increase the efficiency of energy harvesting from vortex induced vibrations as a source of renewable energy.

Chapter 6

Inertioelastic flow instability at a stagnation point

In this chapter (adapted from our publication [3]), the effects of weak elasticity on the flow instability and vortex formation in the cross-slot geometry with $\alpha = 1$ are studied. We show how small changes in fluid elasticity strongly effect the onset of symmetry breaking and vortex formation in the cross-slot geometry. We compare our findings to numerical simulations conducted by our collaborators described in Appendix A [3, 4].

6.1 Introduction

By adding polymers to a Newtonian fluid it is possible to tune the elasticity of the fluid. This affect has been well known and is used for various applications such as drag reduction in turbulent flows [43, 153–157], pressure drop enhancement in porous media flows [158] and inhibiting jet breakup and atomization of sprays [159, 160].

Under flow, polymer additives are known to generate local anisotropic elastic stresses due to stretching and orientation in certain regions of the flow field. These elastic stress can be evaluated in relation to the viscous stresses with the Wiessenberg number (Wi). The interaction between flows and polymers and how this interaction leads to the suppression of inertial instabilities and gives rise to elastic instabilities is not very well understood.

In this chapter we will use the cross-slot geometry to generate a streamwise vortex in order to study the effects of weak elasticity on vortex flows. Since streamwise vortices are a major element in turbulent flows, findings from this chapter can help to explain the phenomena of drag reduction by polymer additives in turbulent flows.

Apart from Wi and Re, a useful dimensionless parameter for characterizing polymeric flows is the elasticity number ($El \approx Wi/\mathrm{Re}$, which quantifies the ratio of elastic to inertial forces in the flow). For Newtonian flows, $El \equiv 0$ and instabilities are "purely inertial", depending only on the magnitude of Re. Flows of highly elastic fluids ($El \gg 1$) present distinct "purely elastic" instabilities that can arise even for negligible inertia. As discussed in the Chapter 1, Section 1.3.2, there is increasing evidence about the generality of these instabilities.

In flows of highly dilute polymer solutions in low viscosity solvents in larger length

scale flow configurations, typical of drag-reduced flows, inertia is not negligible ($0 < El \lesssim 1$) and the flow can be termed "elasto-inertial". In this case there is a complex interaction and competition between inertial and elastic effects that remains to be fully described and understood.

By using the cross-slot device to make direct measurements of the axial vorticity by systematically varying both Re and El, we shed insights on possible mechanisms for the vortex suppression observed in the drag-reduced state of elasto-inertial turbulence (EIT) at the scale of a single streamwise vortex. Changing El by controlling the polymer concentration and solvent viscosity and by characterizing our model fluids in a non-dimensional manner with Wi and El numbers (rather than simply using polymer concentration) we are able to collapse data for the critical Re and Wi conditions in a highly generalized form. Complementary numerical simulations using a finitely extensible non-linear elastic (FENE) dumbbell model provide near-quantitative agreement with our experiments and add important information that is otherwise not attainable from the experiment on the spatial distribution of the elastic stress due to polymer stretching in the complex 3D flow field. We are able to strengthen the links between inertio-elastic instabilities and the suppression of streamwise vorticity observed in drag-reduced flows.

The results presented in this chapter fill a significant gap in the literature between the purely-inertial [27] and purely-elastic regimes (e.g. [44]) and link the two by showing how the instability is transformed from an inertia-dominated to an elasticity-dominated mode as El is increased. The flow in the cross-slot device is characterized by a stagnation point and as demonstrated in the previous chapters, there are many elements of the flow in the cross-slot geometry that resemble other flows (i.e. elongation flow field, stagnation point, curving streamlines). Hence, these results are expected to be relevant in many other geometries with similar characteristics (e.g. [22, 23, 26, 28, 224]).

For this chapter we use a microfluidic device with dimensions of $w = d = 440$ μm and $\alpha = 1$, for further details about the device see Methods, Chapter 2 Section 2.1.2. For details about the experimental protocol see Section 2.4.1. Characterization of the test fluids is detailed in Section 2.5.

Dimensionless numbers are defined in order to characterize the inertial, viscous and elastic forces in both the experiments and numerical simulations. Since some of our polymeric test fluids are shear thinning (see Methods, Chapter 2, Fig. 2.6), the Reynolds number Re is now $\dot{\gamma}$ dependent and defined as:

$$Re = \frac{\rho U w}{\eta(\dot{\gamma})}, \tag{6.1}$$

where $\eta(\dot{\gamma})$ is the shear rate-dependent shear viscosity, and ρ is the fluid (solvent) density.

The Weissenberg number describes the relative importance of elastic to viscous forces in the flow and (in the absence of a solvent viscosity) can be expressed as $Wi = N_1/\tau_{xy} = \lambda\dot{\gamma}$. Here, $N_1 = (\tau_{xx} - \tau_{yy})$ is the first normal stress difference, τ_{xy} is the shear stress, and $\dot{\gamma} = U/w$ is the characteristic shear rate within the flow channel [225]. We define the "effective" Weissenberg number Wi_{eff} which is scaled using the solvent-to-total viscosity ratio $\beta = \eta_s/\eta_0$, where η_s is the solvent viscosity and η_0 is the zero

shear viscosity (see methods Chapter 2, Fig. 2.6), in order to account for the solvent contribution to τ_{xy}, but not to N_1:

$$Wi_{eff} = \lambda\dot{\gamma}(1-\beta). \tag{6.2}$$

The elasticity number is given by the ratio between Wi_{eff} and Re and therefore describes the relative importance of elastic to inertial forces:

$$El = \frac{\lambda\eta(\dot{\gamma})}{\rho w^2}(1-\beta). \tag{6.3}$$

For constant viscosity fluids (such as the majority of our test solutions and the simulations), El is independent of the applied shear rate. Values of El for our test fluids in the microfluidic cross-slot device are provided in Table 2.3.

6.2 Results and discussion

6.2.1 Initial experimental observations of inertial and elastic instabilities

For an initial overview of the parameter space, flow visualizations of dye advection patterns are performed in the $x-y$ centerplane of the cross-slot at $z=0$. For this we

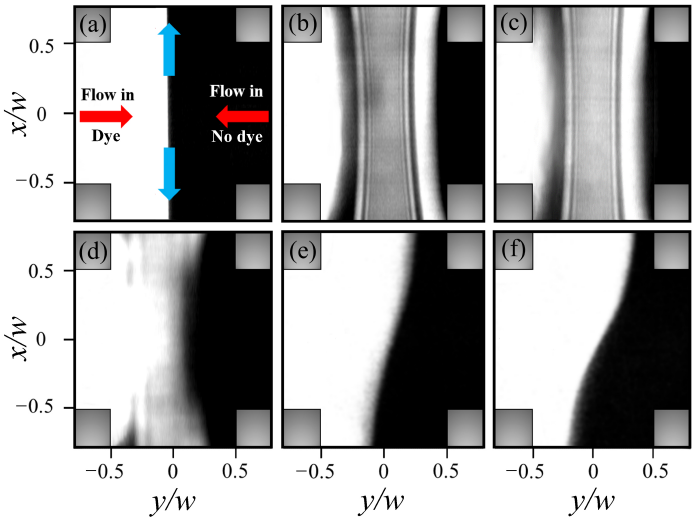

Figure 6.1: Confocal microscope images of dye-advection patterns taken in the $x-y$ centerplane ($z=0$ plane) of the cross-slot device for aqueous PEO solutions of various El. Fluid dyed with rhodamine B enters from the left-hand inlet channel and undyed fluid enters through the right-hand inlet channel [3]. (a) Stable flow with a symmetric interface (Newtonian or viscoelastic, Re < 10); (b) Inertial instability of Newtonian fluid ($El = 0$, Re $= 80$); (c) Inertio-elastic instability with 0.001 wt% PEO solution ($El = 0.00018$, Re $= 79$); (d) Inertio-elastic instability with 0.01 wt% PEO solution ($El = 0.011$, Re $= 33$); (e) Elastic instability with 0.1 wt% PEO solution ($El = 0.68$, Re $= 49$); (f) Elastic instability with 0.3 wt% PEO solution ($El = 10.4$, Re $= 15$).

employed a differential spinning disk (DSD2) confocal microscope (Andor Technology Ltd, Belfast, UK) and a range of aqueous PEO solutions with various El. Solution containing the fluorescent dye rhodamine B (10 μM) is introduced through one inlet of the channel while through the other inlet an undyed solution is introduced. We confirmed that the addition of dye at this concentration had a negligible effect on the physical properties of the fluids.

As shown in Fig. 6.1 a, at low Re $<$ 10 a straight and symmetric interface is observed between the dyed and undyed fluid streams entering the cross-slot. Similar symmetric flow patterns are observed for all the fluids (Newtonian and polymeric) at this low Re. Fig. 6.1 b shows what is observed for the Newtonian fluid (water) when a Reynolds number of Re = 80 is imposed. Here, a distinctive banded structure of alternating bright (dyed) and dark (undyed) regions is observed. This pattern is a slice taken along the $z = 0$ plane through the spiral vortex that has formed, as was similarly shown by Ait Mouheb *et al* [64]. For a PEO solution of $c = 0.001$ wt% and $El = 0.00018$ at Re = 79 (Fig. 6.1 c), the dye advection pattern is similar to that of water at Re = 80 (Fig. 6.1 b). As the PEO concentration is increased to $c = 0.01$ wt% ($El = 0.011$) the structure observed at Re = 33 (Fig. 6.1 d) is blurry when compared with Figs. 6.1 b, c. This is an indication that the flow has become unsteady under these conditions, varying spatio-temporally on a timescale shorter than the image acquisition. At higher polymer concentrations, $c = 0.1$ wt% ($El = 0.68$, Fig. 6.1 e) and $c = 0.3$ wt% ($El = 10.4$, Fig. 6.1 f), the banded pattern indicative of the vortex formation is not observed at all, and instead a different mode of instability emerges. In these images it is seen that most of the dyed fluid flows out through the upper exit channel, while most of the undyed fluid flows out through the lower exit channel. This flow asymmetry has been reported before and described in Chapter 1, Section 1.3.2 and it is considered to be an elasticity-dominated flow instability [44, 77, 144, 145, 148]. We note that the elastic mode observed in this case is unsteady in time.

6.2.2 Experimental and numerical vorticity fields

Aqueous PEO solutions of different polymer concentrations with different El are tested. Our measurements focus on the Re range that is slightly below and slightly above the flow transition from stable symmetric to asymmetric flow and the formation of a central vortex. Fig. 6.2 a-c shows a series of images for fluids of progressively increasing El taken at a specific value of the dimensionless control parameter $\varepsilon = (\mathrm{Re}-\mathrm{Re}_c)/\mathrm{Re}_c = 0.15$. From the images, it is seen that, under comparable flow conditions beyond the onset of instability, the induced vorticity decreases significantly as the fluid elasticity is increased. In Fig. 6.2 d-f, we present vorticity fields resulting from numerical simulations with the FENE-MCR model under conditions of constant El corresponding to Fig. 6.2 a-c, respectively. There is a remarkably good, near quantitative, agreement between the experiment and the numerical simulations. L^2 is the extensibility parameter relating the maximum length of a fully-extended dumbbell to its equilibrium length, and here is set to $L^2 = 5000$ to match the molecular weight of the polymer used in the experiments, as explained in the Methods, Chapter 2, Section 2.5.2, for further details about the numerical simulations see Appen. A.

In Fig. 6.3, we present experimental vorticity fields obtained at $\varepsilon = 0.15$ for two

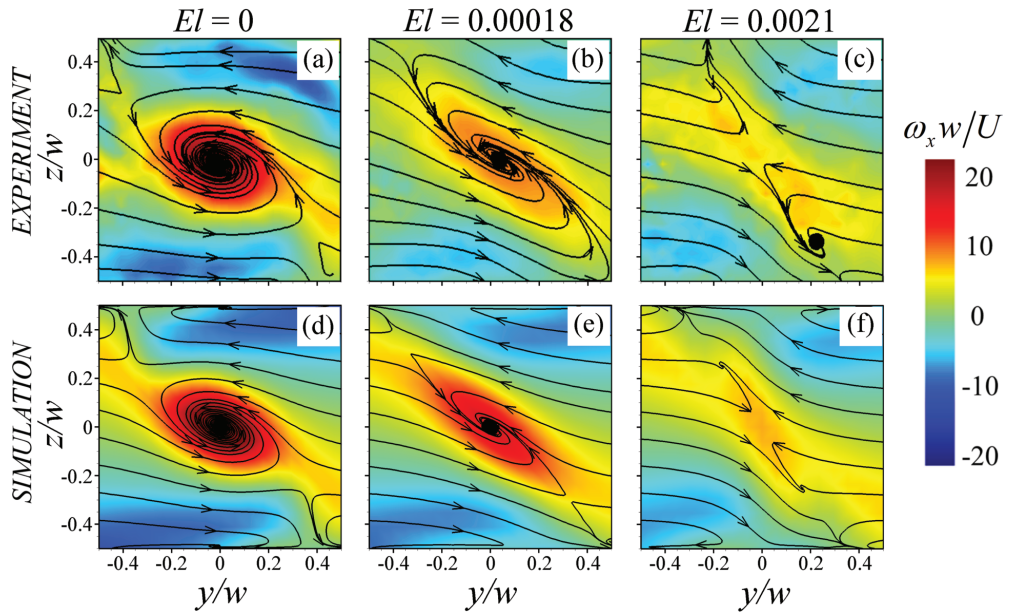

Figure 6.2: A comparison between experimental measurements and numerical simulations of the dimensionless vorticity ($\omega_x d/U$) over the $x = 0$ plane for fluids of various elasticity number El. Top panel shows experimental μ-PIV images obtained at the same value of the dimensionless order parameter $\varepsilon = 0.15$ (Eq. 3.3): (a) $c = 0$ wt% PEO, Re = 47.2; (b) $c = 0.001$ wt% PEO, Re = 37.0; (c) $c = 0.003$ wt% PEO, Re = 28.3. Bottom panel shows converged solutions obtained from constant-El numerical simulations with the FENE-MCR model and $L^2 = 5000$ at similar Reynolds numbers to the experiments: (d) $\beta = 1$ (Newtonian), Re = 47.0; (e) $\beta = 0.99$, Re = 40.0; (f) $\beta = 0.95$, Re = 26.2. The color scale indicates the dimensionless vorticity. Superimposed streamline projections exhibit the directionality of the secondary flow in the cross-section [3].

additional aqueous PEO solutions of higher polymer concentration and elasticity ($c =$ 0.01 wt%, $El = 0.011$ and $c = 0.03$ wt%, $El = 0.078$). Under these conditions there was unsteadiness in the flow; the position of the vortex and the magnitude of the vorticity fluctuates slightly in time. Since numerical simulations are restricted to steady-state solutions (see Appen. A), comparable numerical results at these elasticity numbers are not available. The images shown in Fig. 6.3 are in fact averages made of 15 individual vector fields captured at a rate of 5 Hz over a 3 s time interval. Note that the spatio-temporal fluctuations we report in these two fluids with $El \ll 1$ are completely absent in a Newtonian fluid at an equivalent value of $\varepsilon = 0.15$, for which both experiments and simulations clearly show the flow remains steady and laminar.

Velocity fields obtained in the $x = 0$ plane of the cross-slot device using μ-PIV are used to locally evaluate the vorticity in the axial direction $\omega_x = (\partial v_z/\partial y) - (\partial v_y/\partial z)$. Although other possible parameters can be considered [1, 27], in this chapter we use the measurement of an increase in the value of the center point axial vorticity, $\omega_x|_{x=y=z=0}$ as an indication of the onset of the inertia-dominated mode of instability. The dimensionless order parameter ψ is defined as described in Chapter 3, Eq. 3.6

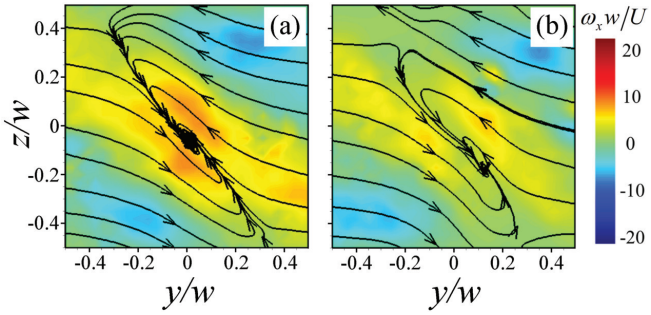

Figure 6.3: Experimental dimensionless vorticity fields in the $x = 0$ plane at $\varepsilon = 0.15$ for (a) $c = 0.01$ wt% PEO in water ($El = 0.011$, Re $= 19.7$), and (b) $c = 0.03$ wt% PEO in water ($El = 0.078$, Re $= 17.2$). Under these conditions the flow exhibited mild unsteadiness and the images shown are averaged over 15 individual fields. The color scale indicates the dimensionless vorticity ($\omega_x d/U$). Superimposed streamlines exhibit the directionality of the flow [3].

($\psi = sgn(\omega_x\ |_{y=z=0})\omega_x\ |_{x=y=z=0}$.)

In Fig. 6.4 the order parameter ψ (Eq. 3.6) is plotted as a function of the applied Reynolds number for a range of aqueous PEO solutions with elasticity numbers $0 \leq El \leq 0.68$. Here, closed symbols represent data obtained by applying quasistatic increases in Re, while open symbols represent data obtained from a subsequent quasistatic decreasing ramp in Re. For each fluid, as Re is progressively increased starting

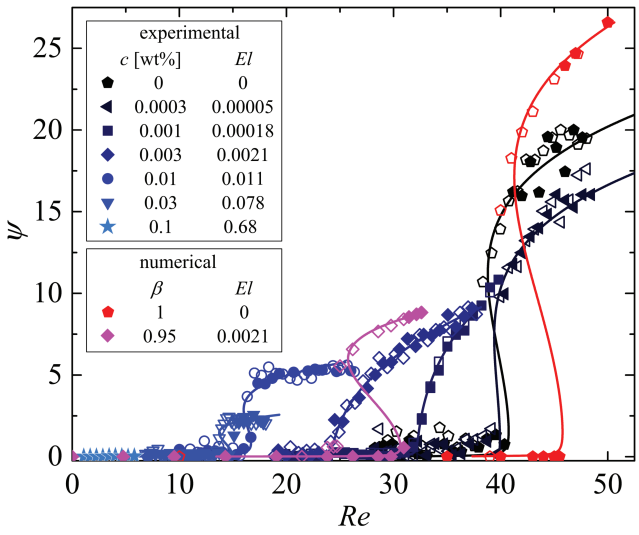

Figure 6.4: Order parameter ψ as a function of Re for solutions of PEO in water, with the viscosity ratio spanning $0.24 < \beta < 1$ for the experimental fluids. Closed symbols indicate data obtained with increasing flow rates and open symbols indicate data obtained with decreasing flow rates. Data is fitted with the Landau model (Eq. 3.3, solid lines). Numerical data is obtained with the FENE-MCR model with $L^2 = 5000$ and constant El [3].

from a low value, ψ initially adopts a value close to zero indicating that the flow field is symmetric. As a fluid-dependent critical value Re_c is reached, the flow field adopts an asymmetric state, resulting in the measurement of a non-zero axial vorticity ω_x at the centerpoint ($y = z = 0$) and hence a non-zero value of the order parameter ψ. For subsequent further increases in Re above Re_c, the measured centerpoint vorticity continues to increase towards a plateau value as the central spiral vortex develops. For subsequent quasistatic reductions in Re starting from a high value (i.e. $\mathrm{Re} > \mathrm{Re}_c$), the centerpoint vorticity also reduces, following the same curve defined by the data for quasistatic increases in Re. For some of the experimental cases (though not all), there is hysteresis in the transition and Re must be reduced to a value $\mathrm{Re}_c^* < \mathrm{Re}_c$ before the flow field recovers symmetry.

The occurrence (or otherwise) of hysteresis appears to have a complex nonmonotonic dependence on the concentration of PEO in the polymer solution, or on the elasticity number of the experiment. We will return to this point in more detail in a subsequent section of the discussion. We note that in the numerical simulations hysteresis is always observed in the transition, and that the value of Re_c tends to be slightly higher than what is observed in the experiments. We have found that the flow transition from symmetric to an asymmetric state in the simulations for increasing Re depends on the level of numerical noise (e.g. mesh size, times step). However, for decreasing Re ramps, the value obtained for Re_c^* is more reliable numerically and more consistent with the experiments, as was also found in previous work [27]. For this reason, further comparison between the experimental and the numerical results will

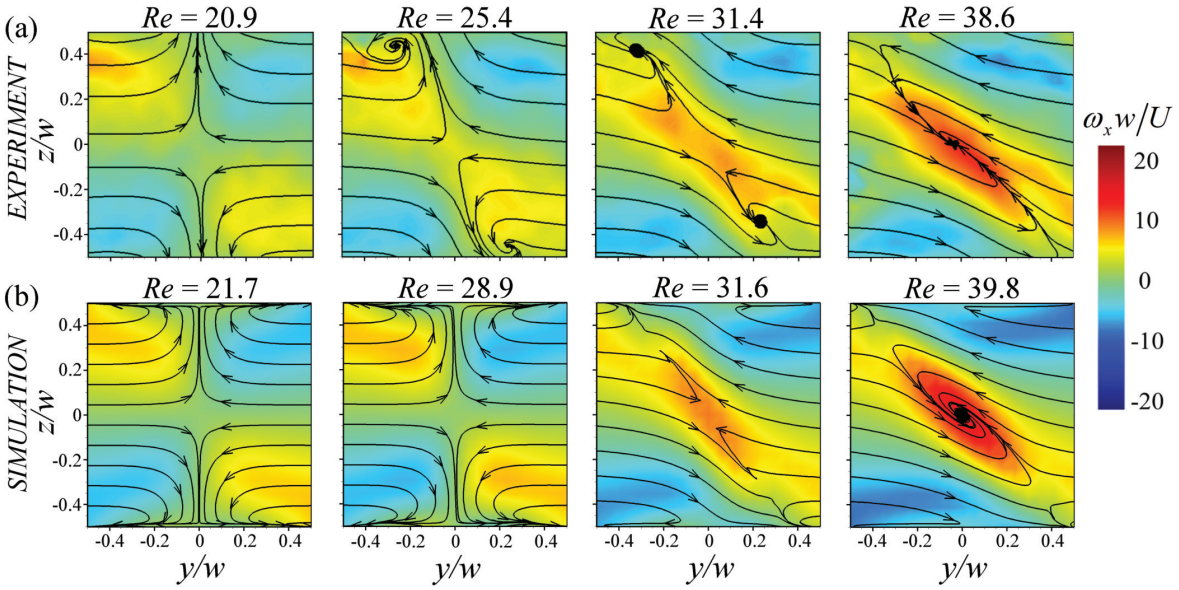

Figure 6.5: A comparison between (a) experimental measurements with a $c = 0.0001$ wt% solution of PEO in 8 wt% PEG ($\beta = 0.97$, $El = 0.00083$) and (b) numerical simulations with $L^2 = 5000$ and $\beta = 0.97$ at constant $El = 0.00083$. The color scale indicates the dimensionless vorticity $\omega_x w/U$ in the $x = 0$ plane. Projected streamlines show the directionality of the secondary flow in the cross-section [3].

be made on the basis of decreasing Re ramps. Despite the minor differences, there is clearly a good general consistency between the experimental and the numerical data presented in Fig. 6.4. It is immediately obvious from both data sets that as El is increased the value of Re_c is decreased. In addition, the normalized centerpoint vorticity tends to approach a reduced plateau value with increasing El. In our experiments with a $c = 0.1$ wt% PEO solution ($El = 0.68$) we did not observe any increase in the centerpoint vorticity before the onset of the elasticity-dominated flow asymmetry, (as illustrated by Fig. 6.1 e). Curve fitting of the data in Fig. 6.4 at each fixed value of El is performed using the Landau model (Eq. 3.3).

Additional μ-PIV measurements are performed using solutions of PEO in the more viscous solvent composed of 8 wt% aqueous PEG. This allows us to formulate fluids with relatively long relaxation times while avoiding the effects of shear-thinning, which occur in the purely aqueous PEO solutions at higher concentrations. Thus we are able to clearly isolate the importance of fluid elasticity from shear-thinning in the polymer solutions. Fig. 6.5 a shows a sequence of four images taken over a range of Re spanning the onset of the transition for the flow of a $c = 0.0001$ wt% solution of PEO in the 8 wt% PEG Newtonian solvent. Here we only show data obtained for quasistatic decreases in Re. This sequence can be compared with Fig. 4.3 e-h that was presented in Chapter 4 for the flow of a Newtonian fluid, revealing marked differences even at this low polymer concentration (only 1 part per million). The flow field in the PEO solution remains asymmetric down to a significantly lower Reynolds number than for the Newtonian fluid, and the vorticity intensification at higher Re is noticeably perturbed in the weakly elastic fluid. Fig. 6.5 b shows a sequence of images obtained

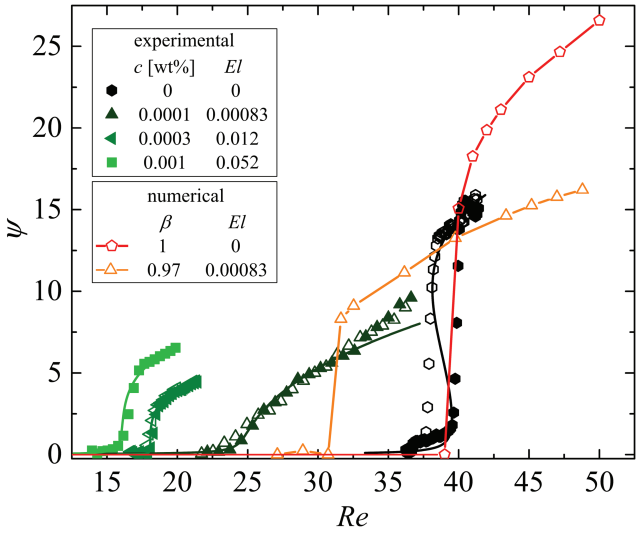

Figure 6.6: Order parameter ψ as a function of Re for solutions of PEO in 8 wt% PEG, with the viscosity ratio spanning $0.91 < \beta < 1$ for the experimental fluids. Closed symbols indicate data obtained with increasing flow rates and open symbols indicate data obtained with decreasing flow rates. Data is fitted with the Landau model (Eq. 3.3, solid lines). Numerical data (decreasing Re ramp only) is obtained with the FENE-MCR model with $L^2 = 5000$ and constant El [3].

from a numerical simulation designed to mimic the experiment shown in Fig. 6.5 a and, once again, the results are in generally good qualitative agreement.

Differences between the low concentration PEO solutions and the 8 wt% PEG Newtonian solvent are clearer to see in Fig. 6.6, which shows the order parameter ψ measured for increasing and decreasing Re and fitted using the Landau model given in Eq. 3.3. The 8 wt% PEG solvent behaves quite similarly to the pure water (Fig. 6.4), showing subcritical behavior with a characteristic hysteresis in the bifurcation. The critical Reynolds number for quasistatic increases in Re is $\mathrm{Re}_c = 40.0$, while for decreasing Re the transition occurs for $\mathrm{Re}_c^* = 38.0$. Further, for $\mathrm{Re} > \mathrm{Re}_c$ the dimensionless vorticity for both water and 8 wt% aqueous PEG approach similar values. The encouraging self-similar behavior displayed by the two Newtonian fluids gives good confidence that we are correctly non-dimensionalizing our order and control parameters. Also (similarly to the experiments performed using PEO solutions prepared in pure water), as the elasticity number increases the bifurcation occurs at a progressively lower value of Re and a general reduction in the maximum centerpoint vorticity occurs. At the highest concentration of PEO in the aqueous 8 wt% PEG solvent that we measured (0.003 wt%, $El = 0.34$), we observed no clear increase in the value of ψ over the range of Re we tested. Instead, we observed the elasticity-dominated mode of instability characterized by the asymmetric flow state, as illustrated by Fig. 6.1 e,f.

6.2.3 Appearance of hysteresis in the flow transition.

As mentioned in Sec. 6.2.2 in the discussion of Figs. 6.4 and 6.6, the Newtonian solvents and some of the polymeric test fluids show hysteretic behavior with a critical Reynolds number that depends on whether the flow rate is ramped up or down quasistatically. Fig. 6.7 summarizes the appearance of hysteresis in the transition for all the experimental test fluids as a function of the elasticity number. Here we examine

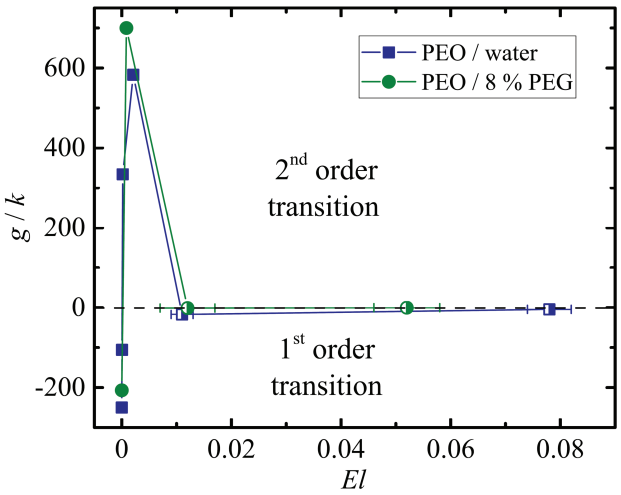

Figure 6.7: The ratio of the parameters g and k as a function of El. The dashed line indicates $g = 0$ where the transition would be tricritical. Above the line the transition is supercritical, below the line the transition is subcritical with hysteresis [3].

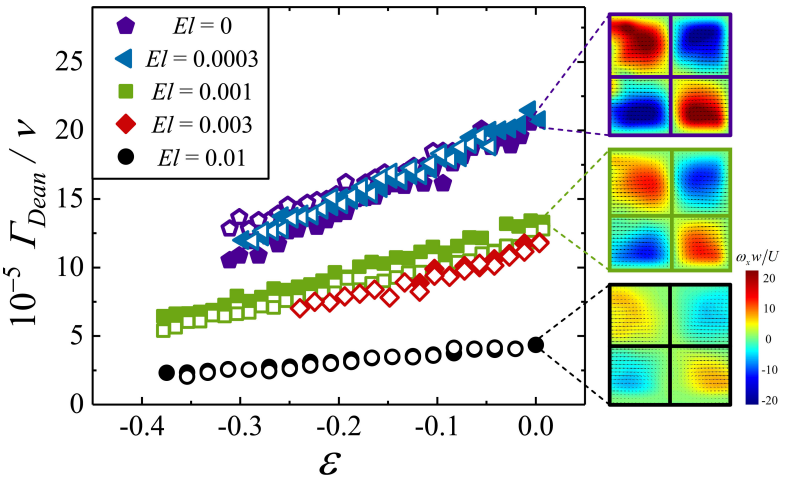

Figure 6.8: The nondimensional circulation Γ_{Dean}/ν of a quadrant from the cross section at $x = 0$ is plotted as a function of ε. Closed and open symbols correspond to increasing and decreasing increments in Re. Insets are μ-PIV images of the vorticity at $x = 0$ for $\varepsilon = 0$. Solid lines in the insets divide the flow field into the defined quadrants [3].

the ratio of the parameters g and k obtained by fitting the Landau model to the experimental data. The ratio g/k has a negative value for Newtonian fluids ($El = 0$), indicating a subcritical transition with hysteresis. As El increases, the size of the hysteresis loop decreases and the transition turns apparently supercritical. For a specific intermediate value of El where $g/k = 0$ the transition would be tricritical. The transition remains supercritical up to values of $El \approx 0.01$. For fluids with elasticity values between $0.01 < El < 0.09$ certain fluids have slightly negative values of g/k and show small hysteresis loops (see e.g. Fig. 6.4), but the general tendency is towards tricritical behavior. Of course the sensitivity of the experiment to noise at different El levels may be masking any underlying hysteretic behavior. In contrast, the numerical simulations with the FENE-MCR model demonstrated hysteretic transitions for all elasticity numbers and β values tested.

Changes in the order of the transition through a tricritical point have been reported in previous work with Newtonian fluids in the cross-slot geometry when the parameter space was changed geometrically by changing the aspect ratio α [27]. Tricritical phenomena in Newtonian fluid mechanics have also been reported for flow in low aspect ratio Taylor-Couette flow cells [49, 50, 196].

In Chapter 4 we showed that the appearance of hysteresis is dependent on the level of vortex confinement which determines vortex intensity and the dynamics of merging and splitting of vortices. Here too, we perform similar analysis in order to have a better understanding of the appearance of hysteresis.

In Fig. 6.8, non-dimensionalized average circulation of the two merging Dean vortices Γ_{Dean} is plotted as a function of ε for $\varepsilon < 0$, prior to symmetry breaking (this figure can be compared to the Newtonian fluid cases presented in Chapter 4, Fig. 4.7). It is apparent that the normalized Γ_{Dean}, is higher for fluids with low elasticity. Increasing El reduces vortex intensity, similarly to the effect that flow confinement has

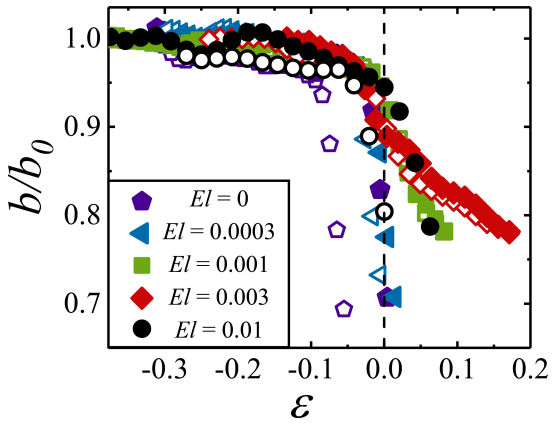

Figure 6.9: (a) Normalized distance between Dean vortex pairs prior to merging, b/b_0 as a function of ε. Closed/open symbols represent increasing/decreasing Re steps [3].

on vortex intensity. The insets of Fig. 6.8, show the vorticity of the flow field at $x = 0$ for $\varepsilon = 0$ at the onset of symmetry breaking. The insets reveal that the vorticity is significantly more intense for low elasticity than higher elasticity fluids.

In order to study the relation between symmetry breaking in weakly elastic fluids and the formation of the central vortex we follow the distance between the cores of the merging vortices, b, normalized by the maximal distance between the cores b_0 [102].

The parameter b/b_0 is plotted as a function of ε in Fig. 6.9, closed and open symbols refer to vortex merging (increasing ε) and splitting (decreasing ε), respectively. This figure can be compared to Fig. 4.8 (a) in Chapter 4.

For $El = 0$, we observe that the onset of symmetry breaking and completion of Dean vortex merging are simultaneous at $\varepsilon = 0$. The splitting of the central vortex (and regaining of symmetry) occurs at $\varepsilon = -0.05$ which confirms the expected hysteresis in the transition. A minor increase in elasticity to $El = 0.0003$ results in a slight, yet measurable prolongation of vortex merging process above the critical value for symmetry breaking at $\varepsilon \simeq 0.02$, symmetry breaking and vortex merging are no longer simultaneous (similar behavior is seen for $\alpha \leq 0.57$ in Chapter 4 Section 4.2.3). When El is further increased, ($El \geq 0.001$), the approach of the dominant Dean vortex pair with increasing ε is gradual and continues well beyond the onset of symmetry breaking. At $El = 0.01$, we again detect hysteresis, however, as we shown in Fig. 6.3, although we can still observe a central vortex formation at this value of El, it is very small in comparison to the vortex formed at $El = 0$ and also, it is slightly unsteady.

As demonstrated in Chapter 4 Section 4.2.3, changing the aspect ratio of the geometry has two effects on merging and splitting process, the first is that Dean vortices that are formed at low α are weaker in intensity when compared to Dean vortices that are formed in higher α. Additionally, the distance between the Dean vortices at low α is relatively smaller than the distance between the Dean vortices at high α. In the experiments done in the current chapter, we decouple the effect of the changing distance between the merging Dean vortices by keeping α constant. In this way it is possible to isolate the effects of Dean vortex intensity on vortex merging process. When compering the findings from Section 4.2.3 Figs. 4.7 and 4.8 (a) and the current

section Figs. 6.8 and 6.9 we demonstrate how changing different parameters have a similar effect on vortex merging and splitting processes and give further confirmation that these processes, at confined intersecting flows, are ruled by vortex intensity.

6.2.4 Detailed analysis and phase diagrams

In this section we summarize the results obtained from both our experiments and our numerical simulations in the form of phase diagrams in dimensionless parameter space. In Fig. 6.10 we present the values of the lower critical Reynolds numbers Re_c^* for the inertial flow transition as a function of the elasticity number El. Over the full range of El for which inertia-dominated transitions occur, the values of Re_c^* obtained from both experimental fluid systems (water and 8 wt% PEG solvents) collapse well onto a single curve described by a strongly decaying exponential function of El: $\mathrm{Re}_c^* = 25\exp(-250El) + 15$. Furthermore, at the low values of $El < 0.01$ which give rise to a steady flow bifurcation, the critical Reynolds numbers obtained from the numerical simulations also collapse onto the same curve.

The exponential decay of Re_c^* with increasing El indicates a system in which the sensitivity to elasticity increases exponentially as El is reduced. This suggests the potential utility of the system as a novel rheometer for weakly elastic fluids. The concept has some analogy with the microfluidic serpentine channel rheometer of Zilz *et al.*, [226] but here exploiting an inertia-dominated as opposed to a purely-elastic instability.

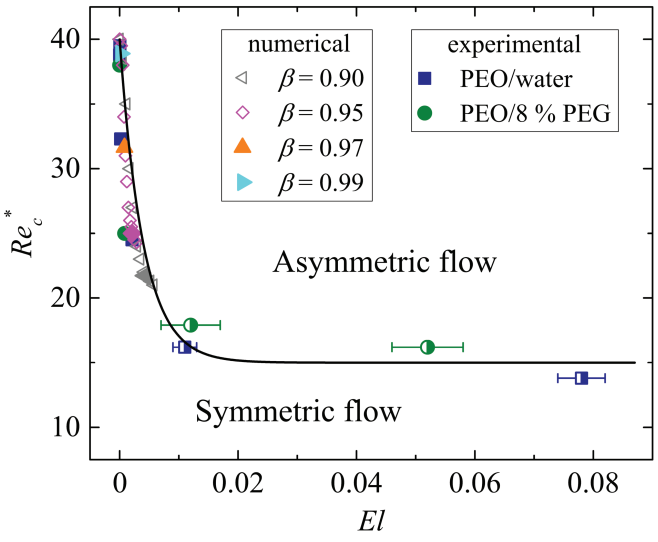

Figure 6.10: Lower critical Reynolds number Re_c^* as a function of the elasticity number El for inertia-dominated flow instabilities of low concentration PEO solutions in a cross-slot device with $\alpha = 1$. For experimental data, closed symbols represent steady instabilities, while half-closed symbols represent unsteady instabilities. For numerical results, open symbols represent constant Wi_{eff}, while closed symbols represent constant El simulations. The solid black line is a decaying exponential fit described in the text [3].

We remark on the similarity between the form of Fig. 6.10 and the reduction in critical Reynolds number with increasing polymer concentration reported for the onset of elasto-inertial turbulence (EIT) by Samanta *et al* [155], although the onset Reynolds number for vortex formation in the cross-slot is around 2 orders of magnitude smaller than that for EIT.

Samanta *et al* showed that following the onset of EIT, the friction factor of the flow directly approaches the maximum drag reduction asymptote [153] as Re is increased. Here, by observing and measuring the vorticity in a single vortex as Re is increased beyond the onset of inertio-elastic instability, the drag reduction reported by Samanta *et al* can clearly be rationalized in terms of the suppression of vortex formation and vorticity growth. However, we interpret the effect of the polymer as causing modification to the inertial (Newtonian) flow state, and not necessarily as driving the formation of a distinct new flow state, as found by Samanta *et al* for fully turbulent flows [155].

The critical Reynolds number for the onset of inertio-elastic flow instabilities in T-shaped intersecting channels with two inlets of aspect ratio $\alpha = 1$ and one outlet of $\alpha = 2$ has also been found to be dependent on El [227]. In the Newtonian case, flow in such channels becomes unstable resulting in the formation of vortices extending along the outlet channel when the Reynolds number exceeds a critical value $\mathrm{Re}_c \approx 100$ [22, 224, 228]. There are rather few numerical and/or experimental studies of non-Newtonian flows in T-channels [76, 227, 229, 230]. However, using the upper-convected Maxwell model, Poole *et al* showed numerically that low levels of fluid elasticity could cause a reduction in Re_c [227]. With highly elastic fluids ($El = 861$), Soulages *et al*

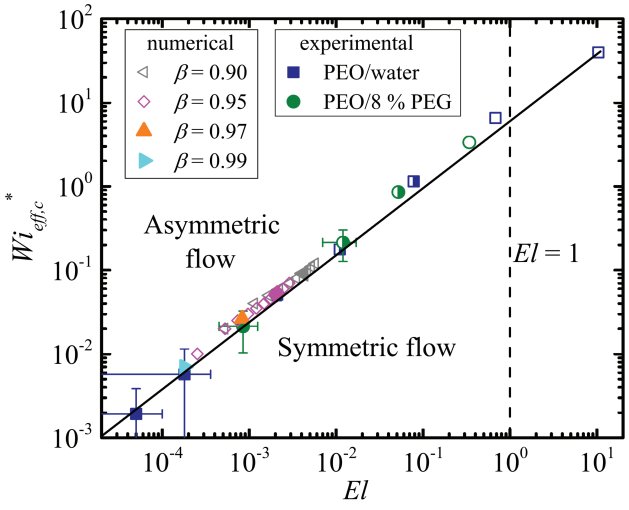

Figure 6.11: $Wi^*_{eff,c}$ as a function of El. For experiments, closed symbols represent steady spiral instabilities, half-closed symbols represent unsteady spiral vortex instabilities, and open symbols represent elasticity-dominated asymmetries. For numerical results, open symbols represent constant Wi_{eff}, while closed symbols represent constant El simulations. The dashed line marks $El = 1$. Power law fit through the data is $Wi^*_{eff,c} = 6El^{0.8}$, (note that error bars on the two lowest El experimental data points extend beyond the boundaries of the plot) [3].

[76] reported flow asymmetries in microfluidic T-channels that appear closely related to the purely-elastic asymmetries seen in cross-slot devices [144, 145]. These limited reports suggest that the effects of increasing fluid elasticity may be similar in various different types of intersecting geometries containing stagnation points.

Studying flow transitions in non-Newtonian fluids is more complex compared with Newtonian fluids due to the additional dimensions of the parameter space [231]. Non-Newtonian transitions in the cross-slot depend not only on Re and α but also on Wi and β (and potentially other groups such as the ratio between first and second normal stress coefficients). This additional parameter space is accessed and explored by changing the El of the fluid. Here this is achieved through manipulation of the polymer concentration and the solvent viscosity, but similar variations could be made via control of, e.g. the polymer molecular weight, polymer flexibility or solvent quality.

In this work, elastic effects in the fluids are characterized using the effective Weissenberg number Wi_{eff}, Eq. 6.2 (which factors out both λ and β) and the elasticity number El, Eq. 6.3 (which additionally factors out Re, i.e. lengthscale, viscosity and density). In Fig. 6.11 we show the values of the lower critical effective Weissenberg number $Wi^*_{\mathit{eff},c}$ as a function of El for all the polymeric test fluids listed in Table 2.3. For fluids that display inertia-dominated (or inertio-elastic) instabilites, the lower critical effective Weissenberg number is computed as $Wi^*_{\mathit{eff},c} = \mathrm{Re}^*_c \times El$. For the fluids that show elasticity-dominated flow asymmetries, $Wi^*_{\mathit{eff},c}$ is estimated from the results of the coarse dye-advection experiments illustrated in Fig. 6.1. All of the data collapses onto a power law with exponent 0.8, as shown by the straight line through the experimental and numerical data points on the log-log plot. We observe clearly that the elastic mode of instability dominates as the elasticity number approaches the value $El = 1$, as might be expected [232].

Increasing El influences the inertial instability by increasing the $Wi_{\mathit{eff},c}$ at which the transition occurs. Higher El further reduces the relative importance of inertial forces and as El approaches the value 1, the inertial instability is completely suppressed, giving rise instead to the purely-elastic time-dependent flow instability as demonstrated in Fig. 6.1 e, f.

In Fig. 6.12 we plot the critical conditions determined for all the non-Newtonian test fluids in the form of a stability diagram in Wi_{eff} - Re dimensionless state space. Here we represent three flow regimes: (1) a region of stable symmetric flow at lower values of Wi_{eff} and Re; (2) a region of inertially-dominated spiral vortex type instabilities, which dominate at higher Re but for $El \lesssim 1$; (3) a region at lower Re and higher Wi_{eff} where elastic asymmetries dominate at $El \gtrsim 1$. The results of numerical simulations deviate somewhat from the experiments at high Re and low Wi_{eff} (i.e. low El), but interestingly approach the experimental trend for lower Re and higher Wi_{eff} (i.e. as El increases). We note some similarity of the stability diagram presented in Fig. 6.12 with those presented by Joo and Shaqfeh [233], who demonstrated by linear stability analysis on Dean and Taylor-Couette flows the destabilization of inertial instability modes by increasing the elasticity, and conversely the destabilization of elastic instability modes by the increase of inertia. We point out that the ranges of $\mathrm{Re} \lesssim 50$ and $Wi_{\mathit{eff}} \lesssim 50$ covered in Fig. 6.4 can be routinely achieved with low viscosity aqueous viscoelastic fluids, even in microfluidic channels. For the validity of such experiments (e.g. cell sorting, immunoassays, DNA analysis), it is clearly of great importance to be aware

of the likelyhood of flow instabilty onset beyond critical conditions and to limit the dimensionless flow parameters within bounds where the flow field remains stable and well-defined.

In the cross-slot, it was shown that the instability of Newtonian flows is a consequence of the introduction of a centerpoint axial vorticity due to imbalances between four cells of Dean vortices that form due to centrifugal forces around the corners of the cross-slot as inertia becomes significant [27]. For $\mathrm{Re} > \mathrm{Re}_{c,Newt} \approx 40$ ($\alpha = 1$), vortex stretching drives the growth of the centerpoint vorticity until a steady state is reached. For the weakly elastic fluids examined here, our numerical simulations give insight into how the presence of the polymeric additive modifies the Newtonian instability mechanism by showing the regions of the flow field where the localized orientation of polymer gives rise to increases in the first normal stress difference $N_1 = (\tau_{xx} - \tau_{yy})$. Such an *in-situ* measurement is not possible using currently available experimental techniques, so the use of complementary simulations here provides a great advantage. Fig. 6.13 shows contours of N_1 for the case $El = 0.0042$, $\beta = 0.90$. At relatively low Re (Fig. 6.13 a, $Wi_{eff} = 0.02$, $\mathrm{Re} = 4.76$), the first normal stress-difference exhibits the anticipated behavior of an extension-dominated flow, where a thin strand of high stress is formed along the flow centreline emanating from the stagnation point [132, 145, 148, 234]. This indicates that significant stretching and orientation occurs at the region close to the stagnation point, which has been demonstrated in previous experiments by the observation of "birefringent strands" [232]. As Wi_{eff} and consequently Re are increased, the flow field is modified and the highest values of the first normal stress difference are no longer located near the stagnation point, but rather are shifted along the vertical

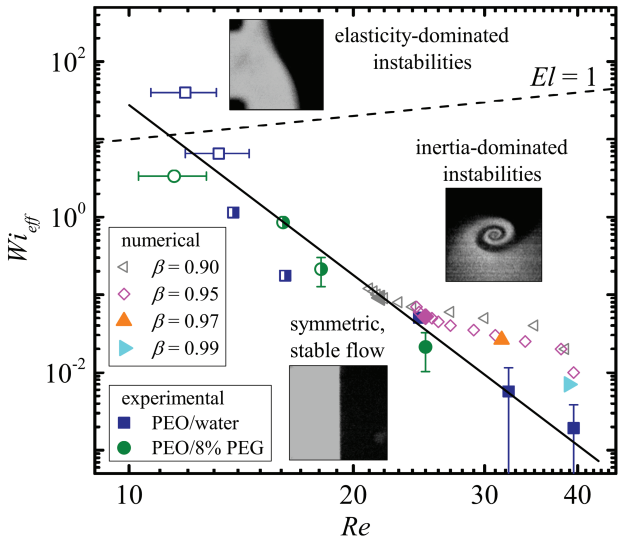

Figure 6.12: Stability diagram in dimensionless Wi_{eff} - Re parameter space. A stable region is indicated below the solid line, drawn through the experimental data as a guide to the eye. For experiments, closed symbols represent steady spiral vortex instabilities, half-closed symbols represent unsteady spiral vortex instabilities, and open symbols represent elasticity-dominated asymmetries. For numerical results, open symbols represent constant Wi_{eff}, while closed symbols represent constant El simulations [3].

direction (z) forming two peaks close to the top and bottom walls of the channel, as shown in Fig. 6.13 b. Although in both Fig. 6.13 a and Fig. 6.13 b, the flow field remains symmetric, the difference is that when $Wi_{eff} = 0.08$ there are Dean vortices present due to inertia. Examining the superimposed streamlines in Fig. 6.13 a, it can be seen that for $Wi_{eff} = 0.02$ the fluid elements that pass close to the stagnation point, which consequently exhibit the higher stretching, are then almost immediately oriented along the outlet streamwise direction. Thus, as they flow far from the high stretching region they gradually relax and the intensity of the birefringent strand slowly decays. In contrast, for $Wi_{eff} = 0.08$ the fluid elements along the inlet flow centreline that pass close to the stagnation point are initially stretched and are then oriented to flow towards the z-direction of the configuration.

When flowing along this path, the already stretched fluid elements experience some additional stretching from the incoming streams, which results in an accumulation of stress from the stagnation point region towards the z-direction and generates high-stress peaks located precisely between the pairs of counter-rotating Dean vortices. Flow feedback in the region of the Dean vortices by these localized peaks in N_1 is the likely cause of the destabilization of the flow for $\mathrm{Re}_c < \mathrm{Re}_{c,Newt}$, as observed both experimentally and numerically. Finally, once the central spiral vortex has formed, the region of the highest N_1 relocates to the vortex core (see Fig. 6.13 c). It is already well-known that the polymer torque resulting in such a situation acts counter to the vorticity [235–239], which explains why the vorticity growth is suppressed in the weakly elastic fluids compared with the Newtonian case as Re is increased above Re_c. Such a mechanism is thought to be responsible for suppression of streamwise and hairpin vortices in polymer drag-reduced flows [235, 236]. These numerical results reveal a complex interplay between inertia and elasticity, suggesting El alone is insufficient to fully capture the observed phenomena, and highlighting that both Wi and Re or (Wi and El) remain important.

For pipe flows at high Re > 1000, Samanta *et al* showed that the criticial Re for the onset of elasto-inertial turbulence (EIT) decreased as the polymer concentration

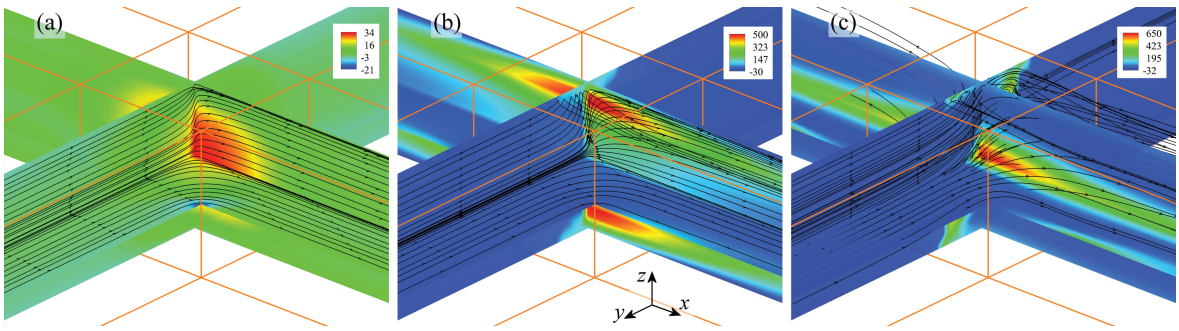

Figure 6.13: Contours of the normalized first normal stress difference $N_1/(\eta_0 U/w)$ (indicated by the color scale) with superimposed streamlines along the centreplanes of the cross-slot. Constant elasticity number simulations using the FENE-MCR model with $El = 0.0042$, $\beta = 0.90$ and (a) $Wi_{eff} = 0.02$, Re = 4.76 (symmetric), (b) $Wi_{eff} = 0.08$, Re = 19.05 (symmetric), and (c) $Wi_{eff} = 0.125$, Re = 29.76 (asymmetric) [3].

was increased [155]. Using pipes of various diameters, they also showed collapse of the critical deformation rate for the onset EIT at different polymer concentrations. The latter observation suggests the importance of polymer deformation and elastic stresses on driving the onset of instability. As Re was increased beyond the onset of EIT, Samanta *et al* showed the friction factor directly approached the maximum drag reduction asymptote while streamwise vortices characteristic of Newtonian turbulence were suppressed. Here, in a very different flow configuration, we make highly analogous observations in a single streamwise vortex as Re is increased beyond the onset of inertio-elastic instability: i.e. a critical Re that decreases with increasing El, a critical Wi that scales with El and a suppression of vorticity growth as the flow is driven beyond the onset of instability. Combined with simulations that provide details of the elastic stresses within the vortex, we can clearly rationalize the drag reduction reported by Samanta *et al* in terms of the action of the polymer. By using a range of fluids with well-characterized elasticity numbers, the collapsed data we obtain for the critical values of Re and Wi_{eff} show that these effects have significant generality.

In the cross-slot device, following the onset of inertio-elastic instability, the resulting flow structures for very low elasticity fluids appear qualitatively similar to those obtained in unstable Newtonian flows (see e.g. Fig. 6.1 b, c and Fig. 6.2 a, b). In this case, the effect of the polymer may be interpreted as causing modification to the inertial (Newtonian) flow state. However, as the elasticity is increased, spatio-temporal fluctuations of the flow structures (which are absent in Newtonian fluids) are observed (see Fig. 6.1 d and Fig. 6.3). As $El \to 1$ we see the emergence of a distinct elasticity-dominated flow state (see Fig. 6.1 e, f). The fluctuating inertio-elastic state shown in Fig. 6.1 d and Fig. 6.3 may well be connected to the distinct nature of the fluctuations observed in EIT compared with traditional Newtonian turbulence, reported by Samanta *et al* [155]. However, further time-resolved investigations of fluctuations arising at higher Re in Newtonian and inertio-elastic flows in the cross-slot geometry will be required in order to confirm this likelihood.

6.3 Summary

In this chapter we study the interactions between an inertial flow instability (that results in the formation of streamwise vortex along the outlet channel) and the elasticity introduced by adding small quantities of a high molecular weight polymer at concentrations relevant to polymer drag reduction. For small increasing values of the elasticity number El, the flow is destabilized at a lower critical Reynolds number than in the Newtonian case. However, following the onset of instability, the growth of the axial vorticity with increasing Re is significantly suppressed by the increase of El. In this regime of low El, our experimental data is well matched by numerical simulations using the constant viscosity FENE-MCR model, which further allows us to locate the regions in the flow domain where high polymer stretch and stress occur. Feedback between localized regions of high polymeric stresses and the flow field are shown to be responsible for the destabilization of the flow at a lower critical Reynolds number than seen in the Newtonian case. Suppression of the subsequent vortex formation is most likely through the action of polymer torque. These quantitative measurements at the scale of

a single vortex provide clear mechanisms for (and a clear visual demonstration of) how polymer additives potentially act to reduce drag in turbulent flows. As the elasticity is increased towards $El \sim 1$, our experimental results show how an inertia-dominated instability is transformed into an elasticity-dominated mode as the vorticity becomes completely suppressed by the action of the polymer additive.

Our data significantly add to the literature on the stability of inertio-elastic flows, which are relevant to understanding a number of important practical applications (e.g. jet breakup, drag reduction, enhanced oil recovery). Our results are anticipated to provide insight into the stability of weakly-elastic fluid flows through intersections and near stagnation points in general.

Summary and Conclusions

A 4-way intersecting flow, offers a unique combination of a planar elongation flow field with curving streamlines and a free stagnation point and is highly sensitive to mild changes of the experimental parameters (i.e., geometric aspect ratio, fluid properties and flow rates). By tuning the parameters of the experiments it is possible to initiate symmetry breaking at relatively low inertial condition (in comparison to other geometries) and form a streamwise vortex. The vortex properties can be controlled in terms of vortex intensity, vortex core structure and the nature of periodic fluctuations that arise in the system.

At low Reynlods number (Re), the flow field at the cross-section of the intersecting region is symmetric, steady and stable. When Re approaches the critical value for symmetry breaking, four cells of Dean vortices form due to the curving streamlines in the flow field. As Re is increased above the critical value, the symmetry between Dean vortices cells breaks as two of the Dean vortices (diagonally opposed and co-rotating) intensify. A merging process is then initiated for the intensified vortices, resulting in the formation of a single, steady, streamwise vortex. Once a central vortex is formed, a reduction in Re can be induced in order to initiate the opposite process, vortex splitting and regaining of symmetry.

By using microfluidic channels fabricated with the Lightfab 3D printing technique, it is possible to perform quantitative measurements of the intersecting region of the cross-slot geometry using micro-particle imaging velocimetry. With this method we experimentally reveal the hysteresis that appears in the flow transition when the aspect ratio of the flow channels is modified. By increasing the aspect ratio (α, the ratio of depth over width of the cross-section) of the channel to $\alpha > 0.55$ it is possible to switch the transition type from supercritical to subcritical. The appearance of hysteresis in the flow transition is found to be dictated by Dean vortex intensity. When the intensity of the Dean vortices is increased (for high α), merging rates are faster, leading to a discontinuous jump in ψ as Re is increased, from the symmetric to the asymmetric branch, resulting in hysteresis. Additionally we find a strong link between the type of the transition and the process of vortex merging in both quasistatic and dynamic experiments. Moreover, we show that the basic principles of vortex merging mechanism in the cross-slot geometry resembles higher Re flows such as the ones seen at the wake of airplane wings.

By adjusting the flow confinement (through a variation of α) and increasing Re to values that are well beyond symmetry breaking, we can control the vortex core structure. For flows that are highly confined (in channels that show supercritical flow transitions) the vorticity profile at the vortex core is represented by a single Gaussian

peak. This structure remains stable until periodic fluctuations emerge upon further increase in Re. For decreased flow confinement (channels that show subcritical flow transitions), the vortex core structure changes upon an increase in Re, developing an area of lower intensity vorticity surrounded by a higher intensity vorticity ring, similar to the structure of an "eye" that appears in tropical storms. Confinement conditions are found to strongly influence the vortex structure and the nature of periodic fluctuations that emerge when Re is further increased. Slight changes in the aspect ratio of the channel results in flow fields that are inherently different from each other and may contain; (1) a single central vortex surrounded by a counter rotating vorticity field ($\alpha = 2.4$), or a flow field that contains side vortices that are either (2) co-rotating ($\alpha = 0.45$), or (3) counter rotating ($\alpha = 1$) with respect to the central vortex. Under high flow confinement conditions, where side vortices exist in the flow field, the periodic fluctuations are dominated by the interaction of the central vortex with the side vortices. In contrast, under lower confinement conditions, where there is only a single well-defined vortex in the flow field, the periodic fluctuations are dominated by a collapse and reformation of the vortex core.

From the fundamental aspect, this thesis demonstrates that experimental microfluidic methods can be used to study inertial fluid dynamics problems such as vortex formation, interactions between vortices and vortex dynamics in a controlled environment. The methods that were used here can be applied for other stagnation point flows that exhibit 3D and time dependent flows. Our findings can assist the improvement of applicable technologies in which vortex suppression is required to stabilize structures. Alternatively, when vortex induced motion is a desired feature (e.g., for energy harvesting purposes), our findings can give guidance on how to modify the geometry in order to control the nature of vortex fluctuations.

The response of the flow to the presence of polymers in low concentrations is also studied with a cross-slot geometry of $\alpha = 1$. By adding polymers to the fluids and applying an extensional flow field we induce local stretching of the polymer. The elastic response of the polymer results in local high stress regions in the flow field which destabilizes the flow and causes symmetry breaking at lower Re. When compared to the Newtonian case, symmetry breaking occurs at progressively lower Re as elasticity is increased by increasing the polymer concentration. Even at extremely low elasticity (parts-per-million of polymer), we observe a significant reduction in the growth of vortex intensity. Numerical simulations identify that the reduction in vortex intensity is related to the torque that a stretched polymer exerts on the flow field. In these inertio-elastic flows we also detect a disappearance of hysteresis from the flow transition due to an increase in elasticity which results in relatively weaker Dean vortices. Similar to the Newtonian case, weaker Dean vortices will lead to a smooth symmetry breaking transition with no hysteresis, as expressed by the growth of ψ when Re is increased. These measurements, that are conducted on a single vortex, provide a clear explanation on how polymers act to reduce drag in turbulent flows. Not only vortex intensity is reduced but also the merging of two co-rotating Dean vortices is delayed far beyond symmetry breaking, indicating slower dynamics when elasticity is increased. Since this flow system shows such high sensitivity to elasticity it can potentially be applied for measurements of elasticity of polymer solutions. Our findings are specifically important for the improvement of applications such as drag reduction in pipe flows, jet breakup

and oil recovery.

There are additional interesting research directions that remain to be explored in future studies, such as using the steady vortex flow in the cross-slot and study the response of particles to the flow field. It has been shown with numerical simulations, that particles that are added to turbulent flows (Newtonian and non-Newtonian) tend to concentrate in regions of low vorticity intensity, yet experiments in 3D system have not been conducted. The experimental system used in this thesis can be applied to study an isolated single vortex and how particles (isotopic and anisotopic) respond to this simplified vortical flow field. Addition of polymers in low concentrations will add elastic forces to the system and are expected to effect particle distribution within and in the surrounding of the vortex.

Other possible directions for future investigations involving intersecting geometries are: (1) study the dynamics of inertio-elastic fluids at confined flow intersections, which may develop to time dependent flows with new unexplored dynamics. Such studies can be relevant to improving drag reduction in blood flows that is confined to narrow arteries. (2) Study the effect of drag-reducing surfactant solutions on vortex formation. (3) Develop a cross-slot device with optimal mixing conditions that can be integrated within automated lab-on-a-chip devices. (4) Study vortex-structure interactions and vortex induced vibrations by introducing posts (which can have circular, triangular or any other geometric shape of the cross section) at the stagnation point or at different locations downstream of the outlet channel. Such studies may contribute to optimize energy conversion from vortex induced motion.

Appendix A

Appendix - Numerical method

The numerical simulations were all done by our collaborators Prof. Rob J. Poole and Dr. Konstantinos Zografos from the university of Liverpool. Here we present them in comparison to the experimental results. The following section describes the numerical method used in this work, taken from our publications Burshtein et al., 2017 and Zografos et al., 2018 [3, 4].

The numerical investigation of the inertially-driven flow instability is achieved by performing three dimensional computational fluid dynamics simulations based on the finite-volume technique [240]. The flow is considered to be laminar, incompressible and isothermal and is governed by the equations of mass conservation and momentum:

$$\nabla \cdot \mathbf{u} = \mathbf{0}, \tag{A.1}$$

$$\rho \left(\frac{\partial \mathbf{u}}{\partial t} + \mathbf{u} \cdot \nabla \mathbf{u} \right) = -\nabla p + \nabla \cdot \boldsymbol{\tau}, \tag{A.2}$$

where $\mathbf{u}$ is the velocity vector, p is the pressure and $\boldsymbol{\tau}$ is the stress tensor which contains the solvent, $\boldsymbol{\tau}_s$, and polymer, $\boldsymbol{\tau}_p$, contributions. Therefore, the stress tensor in the momentum equation is defined as $\boldsymbol{\tau} = \boldsymbol{\tau}_s + \boldsymbol{\tau}_p$, where the solvent component is given by $\boldsymbol{\tau}_s = \eta_s(\nabla \mathbf{u} + \nabla \mathbf{u}^{\mathrm{T}})$. To account for the effects of elasticity, the set of governing equations is completed with an appropriate constitutive equation for $\boldsymbol{\tau}_p$. Here the modified Chilcott-Rallison model, FENE-MCR, is employed [241, 242]:

$$\boldsymbol{\tau}_p + \frac{\lambda}{g(\tau_p)} \overset{\triangledown}{\boldsymbol{\tau}}_p = \eta_p(\nabla \mathbf{u} + \nabla \mathbf{u}^{\mathrm{T}}), \tag{A.3}$$

where $\overset{\triangledown}{\boldsymbol{\tau}}_p$, is the upper-convected derivative of the polymeric component of the stress tensor and $g(\tau_p)$ is a function of the stress tensor, defined as

$$g(\tau_p) = \frac{L^2 + (\lambda/\eta_p)\mathrm{Tr}(\boldsymbol{\tau}_p)}{L^2 - 3}. \tag{A.4}$$

In the above equation, $\mathrm{Tr}(\boldsymbol{\tau}_p)$ refers to the trace operator of the polymeric stress tensor and L^2 is the extensibility parameter. The latter is employed to relate the maximum length of a fully-extended dumbbell to its equilibrium length, and here is set to

$L^2 = 5000$ to match the molecular weight of the polymer used in the experiments, as explained in Section 2.5.2. This viscoelastic model, valid for dilute polymer solutions, exhibits constant shear viscosity and predicts a non-zero, shear-thinning, first normal-stress coefficient which is controlled by the value of L^2 [242]. Moreover, in steady-state extensional flow, as occurs at the stagnation point in the cross-slot geometry which is examined here, the extensional viscosity predicted by the model exhibits a bounded behaviour [242, 243].

An in-house implicit, time marching, finite volume solver [244, 245] is employed in order to numerically solve the governing equations (Eq. A.1, A.2, A.3, A.4). The solver is appropriate for collocated numerical grids, with the convective terms in both the momentum and the polymeric constitutive equation discretised based on the CUBISTA high-resolution scheme [246]. The diffusive terms are discretised considering a central-difference scheme, while the transient terms are evaluated using a first-order implicit Euler scheme. It should be noted that, since we are interested only in the steady-state solution, the 1st order accuracy discretization of the transient term is not restrictive, since the time derivative vanishes when steady-state is reached.

The bulk of our simulations are performed at constant Wi_{eff} (fixed in the range $0.01 \leq Wi_{\mathit{eff}} \leq 0.12$) on two fluids described by high viscosity ratios ($\beta = 0.90$ and $\beta = 0.95$) representative of the experimental samples. By progressive reduction of the Reynolds number from an initially asymmetric solution, a value is obtained for the lower critical Reynolds number Re_c^* for which the flow regains symmetry. Since Wi_{eff} is fixed while Re is varied, these simulations involve a varying elasticity number El. In order to more closely mimic some of the experimental (i.e. fixed El) conditions, a few simulations are performed under conditions of constant elasticity number ($El = 0.00018$ with $\beta = 0.99$, $El = 0.00083$ with $\beta = 0.97$, $El = 0.0021$ with $\beta = 0.95$, and $El = 0.0042$ with $\beta = 0.90$). In these four cases, ramps are performed both up and down in Re in order to examine whether the hysteresis observed (or not) experimentally can be reproduced by the model. We reiterate for clarity that all of the flow fields solved numerically are *steady-state* solutions.

Bibliography

[1] Noa Burshtein, Amy Q Shen, and Simon J Haward. Controlled symmetry breaking and vortex dynamics in intersecting flows. *Physics of Fluids*, 31(3):034104, 2019.

[2] Noa Burshtein, San To Chan, Kazumi Toda-Peters, Amy Q Shen, and Simon J Haward. 3d-printed glass microfluidics for fluid dynamics and rheology. *Current opinion in colloid & interface science*, 2019.

[3] Noa Burshtein, Konstantinos Zografos, Amy Q Shen, Robert J Poole, and Simon J Haward. Inertioelastic flow instability at a stagnation point. *Physical Review X*, 7(4):041039, 2017.

[4] Konstantinos Zografos, Noa Burshtein, Amy Q Shen, Simon J Haward, and Robert J Poole. Elastic modifications of an inertial instability in a 3d cross-slot. *Journal of Non-Newtonian Fluid Mechanics*, 2018.

[5] Sep. 12, 2019, image by nasa.

[6] Cathal Cummins, Madeleine Seale, Alice Macente, Daniele Certini, Enrico Mastropaolo, Ignazio Maria Viola, and Naomi Nakayama. A separated vortex ring underlies the flight of the dandelion. *Nature*, 562(7727):414, 2018.

[7] www.flikr.com.

[8] www.lankhorst-offshore.com.

[9] Michael Bernitsas. Out of the vortex. *Mechanical Engineering Magazine Select Articles*, 132(04):22–27, 2010.

[10] Dieter Peters, Pawel Vargin, and Heiner Körnich. A study of the zonally asymmetric tropospheric forcing of the austral vortex splitting during september 2002. *Tellus A: Dynamic Meteorology and Oceanography*, 59(3):384–394, 2007.

[11] Adrian Simmons, Mariano Hortal, Graeme Kelly, Anthony McNally, Agathe Untch, and Sakari Uppala. ECMWF analyses and forecasts of stratospheric winter polar vortex breakup: September 2002 in the southern hemisphere and related events. *Journal of the Atmospheric Sciences*, 62(3):668–689, 2005.

[12] Allan O'Neill, CL Oatley, Andrew J Charlton-Perez, DM Mitchell, and Thomas Jung. Vortex splitting on a planetary scale in the stratosphere by cyclogenesis on a subplanetary scale in the troposphere. *Quarterly Journal of the Royal Meteorological Society*, 143(703):691–705, 2017.

[13] Claudia Pasquero, Antonello Provenzale, and Jeffrey B Weiss. Vortex statistics from eulerian and lagrangian time series. *Physical review letters*, 89(28):284501, 2002.

[14] David Lentink, Florian T Muijres, Frits J Donker-Duyvis, and Johan L van Leeuwen. Vortex-wake interactions of a flapping foil that models animal swimming and flight. *Journal of Experimental Biology*, 211(2):267–273, 2008.

[15] Ramiro Godoy-Diana and B Thiria. On the diverse roles of fluid dynamic drag in animal swimming and flying. *Journal of The Royal Society Interface*, 15(139):20170715, 2018.

[16] Pier Giuseppe Ledda, Lorenzo Siconolfi, Francesco Viola, Simone Camarri, and François Gallaire. Flow dynamics of a dandelion pappus: A linear stability approach. *Physical Review Fluids*, 4(7):071901, 2019.

[17] AL Chen, JD Jacob, and Ö Savaş. Dynamics of corotating vortex pairs in the wakes of flapped airfoils. *Journal of Fluid Mechanics*, 382:155–193, 1999.

[18] Philippe R Spalart. Airplane trailing vortices. *Annual Review of Fluid Mechanics*, 30(1):107–138, 1998.

[19] Charles HK Williamson. Vortex dynamics in the cylinder wake. *Annual review of fluid mechanics*, 28(1):477–539, 1996.

[20] CHK Williamson and R Govardhan. Vortex-induced vibrations. *Annu. Rev. Fluid Mech.*, 36:413–455, 2004.

[21] Ali Bakhshandeh Rostami and Mohammadmehdi Armandei. Renewable energy harvesting by vortex-induced motions: Review and benchmarking of technologies. *Renewable and Sustainable Energy Reviews*, 70:193–214, 2017.

[22] A. Fani, S. Camarri, and M. V. Salvetti. Investigation of the steady engulfment regime in a three-dimensional T-mixer. *Phys. Fluids*, 25(6):064102, 2013.

[23] D. Vigolo, S. Radl, and H. A. Stone. Unexpected trapping of particles at a T-junction. *Proc. Nat. Acad. Sci.*, 111:4770, 2014.

[24] J. T. Ault, K. K. Chen, and H. A. Stone. Downstream decay of fully developed Dean flow. *J. Fluid Mech.*, 777:219–244, 2015.

[25] K. K. Chen, C. W. Rowley, and H. A. Stone. Vortex dynamics in a pipe T-junction: Recirculation and sensitivity. *Phys. Fluids*, 27(3):034107, 2015.

[26] J. T. Ault, A. Fani, K. K. Chen, S. Shin, F. Gallaire, and H. A. Stone. Vortex-breakdown-induced particle capture in branching junctions. *Phys. Rev. Lett.*, 117:084501, 2016.

[27] S. J. Haward, R. J. Poole, M. A. Alves, P. J. Oliveira, N. Goldenfeld, and A. Q. Shen. Tricritical spiral vortex instability in cross-slot flow. *Phys. Rev. E*, 93:031101, 2016.

[28] K. K. Chen, C. W. Rowley, and H. A. Stone. Vortex breakdown, linear global instability and sensitivity of pipe bifurcation flows. *J. Fluid Mech.*, 815:257–294, 2017.

[29] San To Chan, Simon J Haward, and Amy Q Shen. Microscopic investigation of vortex breakdown in a dividing t-junction flow. *Physical Review Fluids*, 3(7):072201, 2018.

[30] David Oettinger, Jesse T Ault, Howard A Stone, and George Haller. Invisible anchors trap particles in branching junctions. *Physical review letters*, 121(5):054502, 2018.

[31] San To Chan, Jesse T Ault, Simon J Haward, E Meiburg, and Amy Q Shen. Coupling of vortex breakdown and stability in a swirling flow. *Physical Review Fluids*, 4(8):084701, 2019.

[32] Eli Sarid, Catalin Teodorescu, Philip S Marcus, and Joel Fajans. Breaking of rotational symmetry in cylindrically bounded 2d electron plasmas and 2d fluids. *Physical review letters*, 93(21):215002, 2004.

[33] Antoine J Cerfon. Vortex dynamics and shear-layer instability in high-intensity cyclotrons. *Physical review letters*, 116(17):174801, 2016.

[34] KS Fine, CF Driscoll, JH Malmberg, and TB Mitchell. Measurements of symmetric vortex merger. *Physical review letters*, 67(5):588, 1991.

[35] MT Reeves, TP Billam, Brian P Anderson, and AS Bradley. Identifying a superfluid reynolds number via dynamical similarity. *Physical review letters*, 114(15):155302, 2015.

[36] Woo Jin Kwon, Joon Hyun Kim, Sang Won Seo, and Yong-il Shin. Observation of von kármán vortex street in an atomic superfluid gas. *Physical review letters*, 117(24):245301, 2016.

[37] Philip Holmes, John L Lumley, Gahl Berkooz, and Clarence W Rowley. *Turbulence, coherent structures, dynamical systems and symmetry*. Cambridge university press, 2012.

[38] Luca Biferale, Fabio Bonaccorso, Irene M Mazzitelli, Michel AT van Hinsberg, Alessandra S Lanotte, Stefano Musacchio, Prasad Perlekar, and Federico Toschi. Coherent structures and extreme events in rotating multiphase turbulent flows. *Physical Review X*, 6(4):041036, 2016.

[39] James C McWilliams. The vortices of two-dimensional turbulence. *Journal of Fluid Mechanics*, 219:361–385, 1990.

[40] Javier Jimenez, HK Moffatt, and Carlos Vasco. The structure of the vortices in freely decaying two-dimensional turbulence. *Journal of Fluid Mechanics*, 313:209–222, 1996.

[41] R Benzi, M Colella, M Briscolini, and Paolo Santangelo. A simple point vortex model for two-dimensional decaying turbulence. *Physics of Fluids A: Fluid Dynamics*, 4(5):1036–1039, 1992.

[42] B. A. Toms. Some observations on the flow of linear polymer solutions through straight tubes at large reynolds numbers. *in Proceedings of the First International Congress on Rheology*, 2:135–141, 1948.

[43] P. S. Virk and H. Baher. The effect of polymer concentration on drag reduction. *Chem. Eng. Sci.*, 25:1183–1189, 1970.

[44] S. J. Haward, G. H. McKinley, and A. Q. Shen. Elastic instabilities in planar elongational flow of monodisperse polymer solutions. *Scientific Reports*, 6:33029, 2016.

[45] Flow visualization: a course in the physics and art of fluid flow by jean hertzberg and students at cu boulder www.flowvis.org.

[46] François Charru. *Hydrodynamic instabilities*, volume 37. Cambridge University Press, 2011.

[47] Geoffrey Ingram Taylor. Viii. stability of a viscous liquid contained between two rotating cylinders. *Philosophical Transactions of the Royal Society of London. Series A, Containing Papers of a Mathematical or Physical Character*, 223(605-615):289–343, 1923.

[48] Wo R Dean. Xvi. note on the motion of fluid in a curved pipe. *The London, Edinburgh, and Dublin Philosophical Magazine and Journal of Science*, 4(20):208–223, 1927.

[49] A. Aitta, G. Ahlers, and D. S. Cannell. Tricritical phenomena in rotating Couette-Taylor flow. *Phys. Rev. Lett.*, 54(7):673–676, 1985.

[50] A. Aitta. Quantitative Landau model for bifurcations near a tricritical point in Couette-Taylor flow. *Phys. Rev. A*, 34(3):2086–2092, 1986.

[51] J. M. Burgers. A mathematical model illustrating the theory of turbulence. *Adv. Appl. Mech.*, 1:171–199, 1948.

[52] R. R. Lagnado and L. G. Leal. Visualization of three-dimensional flow in a four-roll mill. *Exp. Fluids*, 9:25–32, 1990.

[53] Geoffrey Ingram Taylor. Viii. stability of a viscous liquid contained between two rotating cylinders. *Philosophical Transactions of the Royal Society of London. Series A, Containing Papers of a Mathematical or Physical Character*, 223(605-615):289–343, 1923.

[54] Y. A. Aryshev, V. A. Golovin, and S. A. Ershin. Stability of colliding flows. *Fluid Dyn.*, 16(5):755–759, 1981.

[55] O. S. Kerr and J. W. Dold. Periodic steady vortices in a stagnation-point flow. *J. Fluid Mech.*, 276:307–325, 1994.

[56] V. N. Kalashnikov and M. G. Tsiklauri. Ordered three-dimensional structures resulting from instability of two-dimensional flow in crossed channels. *Fluid Dynamics*, 26:161, 1991.

[57] Jun Zhang, Sheng Yan, Dan Yuan, Gursel Alici, Nam-Trung Nguyen, Majid Ebrahimi Warkiani, and Weihua Li. Fundamentals and applications of inertial microfluidics: a review. *Lab on a Chip*, 16(1):10–34, 2016.

[58] Aram J Chung. A minireview on inertial microfluidics fundamentals: Inertial particle focusing and secondary flow. *BioChip Journal*, 13(1):53–63, 2019.

[59] Abdolrahman Dadvand, Soheil Hosseini, Saharnaz Aghebatandish, and Boo Cheong Khoo. Enhancement of heat and mass transfer in a microchannel via passive oscillation of a flexible vortex generator. *Chemical Engineering Science*, 2019.

[60] Daniel Stoecklein and Dino Di Carlo. Nonlinear microfluidics. *Analytical chemistry*, 91(1):296–314, 2018.

[61] Hamed Amini, Elodie Sollier, Mahdokht Masaeli, Yu Xie, Baskar Ganapathysubramanian, Howard A Stone, and Dino Di Carlo. Engineering fluid flow using sequenced microstructures. *Nature communications*, 4:1826, 2013.

[62] Dino Di Carlo, Daniel Irimia, Ronald G Tompkins, and Mehmet Toner. Continuous inertial focusing, ordering, and separation of particles in microchannels. *Proceedings of the National Academy of Sciences*, 104(48):18892–18897, 2007.

[63] N. Ait Mouheb, A. Montillet, C. Solliec, J. Havlica, P. Legentilhomme, J. Comiti, and J. Tihon. Flow characterization in T-shaped and cross-shaped micromixers. *Microfluid. Nanofluid.*, 10:1185–1197, 2011.

[64] N. Ait Mouheb, D. Malsch, A. Montillet, C. Solliec, and T. Henkel. Numerical and experimental investigations of mixing in T-shaped and cross-shaped micromixers. *Chem. Eng. Sci.*, 68:278–289, 2012.

[65] Abraham D Stroock, Stephan KW Dertinger, Armand Ajdari, Igor Mezić, Howard A Stone, and George M Whitesides. Chaotic mixer for microchannels. *Science*, 295(5555):647–651, 2002.

[66] Anna Haller, Andreas Spittler, Lukas Brandhoff, Helene Zirath, Dietmar Puchberger-Enengl, Franz Keplinger, and Michael Vellekoop. Microfluidic vortex enhancement for on-chip sample preparation. *Micromachines*, 6(2):239–251, 2015.

[67] Chia-Yen Lee, Chin-Lung Chang, Yao-Nan Wang, and Lung-Ming Fu. Microfluidic mixing: a review. *International journal of molecular sciences*, 12(5):3263–3287, 2011.

[68] Mubashshir A Ansari, Kwang-Yong Kim, Khalid Anwar, and Sun Min Kim. Vortex micro t-mixer with non-aligned inputs. *Chemical Engineering Journal*, 181:846–850, 2012.

[69] Mingzhao Guo, Xingjian Hu, Fan Yang, Song Jiao, Yujun Wang, Haiyan Zhao, Guangsheng Luo, and Huimin Yu. Mixing performance and application of a three-dimensional serpentine microchannel reactor with a periodic vortex-inducing structure. *Industrial & Engineering Chemistry Research*, 58(29):13357–13365, 2019.

[70] Robyn H Pritchard, Alexander A Zhukov, James N Fullerton, Andrew J Want, Fred Hussain, Mette F la Cour, Mikhail E Bashtanov, Richard D Gold, Anthony Hailes, Edward Banham-Hall, et al. Cell sorting actuated by a microfluidic inertial vortex. *Lab on a Chip*, 2019.

[71] Shiang-Chi Lin, Pei-Wen Yen, Chien-Chung Peng, and Yi-Chung Tung. Single channel layer, single sheath-flow inlet microfluidic flow cytometer with three-dimensional hydrodynamic focusing. *Lab on a Chip*, 12(17):3135–3141, 2012.

[72] C. Fang, D. Lee, B. Stober, G. G. Fuller, and A. Q. Shen. Integrated microfluidic platform for instantaneous flow and localized temperature control. *RSC Adv.*, 5:85620–85629, 2015.

[73] Corinne Renier, Edward Pao, James Che, Haiyan E Liu, Clementine A Lemaire, Melissa Matsumoto, Melanie Triboulet, Sandy Srivinas, Stefanie S Jeffrey, Matthew Rettig, et al. Label-free isolation of prostate circulating tumor cells using vortex microfluidic technology. *NPJ precision oncology*, 1(1):15, 2017.

[74] Junsheng Wang, Myint Myint Maw, Xiaomei Yu, Bowen Dai, Ge Wang, and Zong Jiang. Applications and perspectives on microfluidic technologies in ships and marine engineering: A review. *Microfluidics and Nanofluidics*, 21(3):39, 2017.

[75] Marc Karle, Sandeep Kumar Vashist, Roland Zengerle, and Felix von Stetten. Microfluidic solutions enabling continuous processing and monitoring of biological samples: A review. *Analytica chimica acta*, 929:1–22, 2016.

[76] J. Soulages, M. S. N. Oliveira, P. C. Sousa, M. A. Alves, and G. H. McKinley. Investigating the stability of viscoelastic stagnation flows in T-shaped microchannels. *J. Non-Newtonian Fluid Mech.*, 163:9–24, 2009.

[77] P. C. Sousa, F. T. Pinho, M. S. N. Oliveira, and M. A. Alves. Purely elastic flow instabilities in microscale cross-slot devices. *Soft Matter*, 11:8856–8862, 2015.

[78] Arthur Kalb, Larry A Villasmil-Urdaneta, and Michael Cromer. Elastic instability and secondary flow in cross-slot flow of wormlike micellar solutions. *Journal of Non-Newtonian Fluid Mechanics*, 262:79–91, 2018.

[79] Kai-Wen Hsiao, Chandi Sasmal, J Ravi Prakash, and Charles M Schroeder. Direct observation of dna dynamics in semidilute solutions in extensional flow. *Journal of Rheology*, 61(1):151–167, 2017.

[80] P. G. De Gennes. Coil-stretch transition of dilute flexible polymers under ultrahigh velocity gradients. *J. Chem. Phys.*, 60:5030–5042, 1974.

[81] R. G. Larson and J. J. Magda. Coil-stretch transitions in mixed shear and extensional flows of dilute polymer solutions. *Macromolecules*, 22:3004–3010, 1989.

[82] T. T. Perkins, D. E. Smith, and S. Chu. Single polymer dynamics in an elongational flow. *Science*, 276:2016–2021, 1997.

[83] D. E. Smith and S. Chu. Response of flexible polymers to a sudden elongation flow. *Science*, 281:1335–1340, 1998.

[84] C. M. Schroeder, H. P. Babcock, E. S. G. Shaqfeh, and S. Chu. Observation of polymer conformation hysteresis in extensional flow. *Science*, 301:1515–1519, 2003.

[85] F Pimenta and MA Alves. Electro-elastic instabilities in cross-shaped microchannels. *Journal of Non-Newtonian Fluid Mechanics*, 259:61–77, 2018.

[86] PC Sousa, FT Pinho, and MA Alves. Purely-elastic flow instabilities and elastic turbulence in microfluidic cross-slot devices. *Soft Matter*, 14(8):1344–1354, 2018.

[87] PG Correa, JR Mac Intyre, JM Gomba, MA Cachile, JP Hulin, and H Auradou. Three-dimensional flow structures in x-shaped junctions: Effect of the reynolds number and crossing angle. *Physics of Fluids*, 31(4):043606, 2019.

[88] R. Dylla-Spears, J. E. Townsend, L. Jen-Jacobson, L. L. Sohn, and S. J. Muller. Single-molecule sequence detection via microfluidic planar extensional flow at a stagnation point. *Lab Chip*, 10:1543–1549, 2010.

[89] J. A. Pathak and S. D. Hudson. Rheo-optics of equilibrium polymer solutions: Wormlike micelles in elongational flow in a microfluidic cross-slot. *Macromolecules*, 39:8782–8792, 2006.

[90] SJ Haward. Microfluidic extensional rheometry using stagnation point flow. *Biomicrofluidics*, 10(4):043401, 2016.

[91] Laura K Brandt and Keiko K Nomura. The physics of vortex merger and the effects of ambient stable stratification. *Journal of Fluid Mechanics*, 592:413–446, 2007.

[92] Ciro Cerretelli and CHK Williamson. The physical mechanism for vortex merging. *Journal of Fluid Mechanics*, 475:41–77, 2003.

[93] Patrice Meunier, Stéphane Le Dizes, and Thomas Leweke. Physics of vortex merging. *Comptes Rendus Physique*, 6(4-5):431–450, 2005.

[94] Ch Josserand and M Rossi. The merging of two co-rotating vortices: a numerical study. *European Journal of Mechanics-B/Fluids*, 26(6):779–794, 2007.

[95] MV Melander, NJ Zabusky, and JC McWilliams. Symmetric vortex merger in two dimensions: causes and conditions. *Journal of Fluid Mechanics*, 195:303–340, 1988.

[96] IM Lansky, TM O'Neil, and DA Schecter. A theory of vortex merger. *Physical Review Letters*, 79(8):1479, 1997.

[97] David G Dritschel. A general theory for two-dimensional vortex interactions. *Journal of Fluid Mechanics*, 293:269–303, 1995.

[98] PG Saffman and R Szeto. Equilibrium shapes of a pair of equal uniform vortices. *The Physics of Fluids*, 23(12):2339–2342, 1980.

[99] Edward A Overman and Norman J Zabusky. Evolution and merger of isolated vortex structures. *The Physics of Fluids*, 25(8):1297–1305, 1982.

[100] Jinhee Jeong and Fazle Hussain. On the identification of a vortex. *Journal of Fluid Mechanics*, 285:69–94, 1995.

[101] Tobias Guenther and Holger Theisel. Hyper-objective vortices. *IEEE transactions on visualization and computer graphics*, 2018.

[102] Thomas Leweke, Stéphane Le Dizès, and Charles HK Williamson. Dynamics and instabilities of vortex pairs. *Annual Review of Fluid Mechanics*, 48:507–541, 2016.

[103] EJ Hopfinger and GJFV Heijst. Vortices in rotating fluids. *Annual Review of Fluid Mechanics*, 25(1):241–289, 1993.

[104] P Freymuth, W Bank, and M Palmer. First experimental evidence of vortex splitting. *The Physics of Fluids*, 27(5):1045–1046, 1984.

[105] P Freymuth, W Bank, and M Palmer. Further experimental evidence of vortex splitting. *Journal of Fluid Mechanics*, 152:289–299, 1985.

[106] Y Guo and WH Finlay. Splitting, merging and wavelength selection of vortices in curved and/or rotating channel flow due to eckhaus instability. *Journal of Fluid Mechanics*, 228:661–691, 1991.

[107] PM Ligrani, JE Longest, MR Kendall, and WA Fields. Splitting, merging and spanwise wavenumber selection of dean vortex pairs. *Experiments in Fluids*, 18(1-2):41–58, 1994.

[108] DW Moore and P Gr Saffman. Structure of a line vortex in an imposed strain. In *Aircraft wake turbulence and its detection*, pages 339–354. Springer, 1971.

[109] PG Saffman and GR Baker. Vortex interactions. *Annual Review of Fluid Mechanics*, 11(1):95–121, 1979.

[110] JP Christiansen and Norman J Zabusky. Instability, coalescence and fission of finite-area vortex structures. *Journal of Fluid Mechanics*, 61(2):219–243, 1973.

[111] Salvador Rodriguez, Flor Espinoza, Stan Steinberg, and Mohamed El-Genk. Towards a unified swirl vortex model. In *42nd AIAA Fluid Dynamics Conference and Exhibit*, page 3354, 2012.

[112] Christophe Eloy and Stéphane Le Dizès. Three-dimensional instability of burgers and lamb–oseen vortices in a strain field. *Journal of Fluid Mechanics*, 378:145–166, 1999.

[113] Jan-Bert Flór and GJF Van Heijst. Stable and unstable monopolar vortices in a stratified fluid. *Journal of fluid mechanics*, 311:257–287, 1996.

[114] MG Hall. The structure of concentrated vortex cores. *Progress in Aerospace Sciences*, 7:53–110, 1966.

[115] Saman Rashidi, Masoud Hayatdavoodi, and Javad Abolfazli Esfahani. Vortex shedding suppression and wake control: A review. *Ocean Engineering*, 126:57–80, 2016.

[116] Uwe Fey, Michael König, and Helmut Eckelmann. A new strouhal–reynolds-number relationship for the circular cylinder in the range 47< re< 2× 10 5. *Physics of Fluids*, 10(7):1547–1549, 1998.

[117] T Leweke and M Provansal. The flow behind rings: bluff body wakes without end effects. *Journal of Fluid Mechanics*, 288:265–310, 1995.

[118] Tommaso Andreussi, Chiara Galletti, Roberto Mauri, Simone Camarri, and Maria Vittoria Salvetti. Flow regimes in t-shaped micro-mixers. *Computers & Chemical Engineering*, 76:150–159, 2015.

[119] Jing-wei Zhang, Shao-fan Liu, Chen Cheng, Wei-feng Li, Xin-lei Xu, Hai-feng Liu, and Fu-chen Wang. Investigation of three-dimensional flow regime and mixing characteristic in t-jet reactor. *Chemical Engineering Journal*, 358:1561–1573, 2019.

[120] Susan Thomas and Timothy A Ameel. An experimental investigation of moderate reynolds number flow in a t-channel. *Experiments in fluids*, 49(6):1231–1245, 2010.

[121] Simon Dreher, Norbert Kockmann, and Peter Woias. Characterization of laminar transient flow regimes and mixing in t-shaped micromixers. *heat transfer engineering*, 30(1-2):91–100, 2009.

[122] AV Minakov, V Ya Rudyak, AA Gavrilov, and AA Dekterev. Mixing in a t-shaped micromixer at moderate reynolds numbers. *Thermophysics and Aeromechanics*, 19(3):385–395, 2012.

[123] Tobias Schikarski, Wolfgang Peukert, and Marc Avila. Direct numerical simulation of water–ethanol flows in a t-mixer. *Chemical Engineering Journal*, 324:168–181, 2017.

[124] Jing-Wei Zhang, Wei-Feng Li, Xin-Lei Xu, Hai-Feng Liu, and Fu-Chen Wang. Experimental investigation of three-dimensional flow regimes in a cross-shaped reactor. *Physics of Fluids*, 31(3):034105, 2019.

[125] Jason R Stokes, Lachlan JW Graham, Nick J Lawson, and David V Boger. Swirling flow of viscoelastic fluids. part 2. elastic effects. *Journal of Fluid Mechanics*, 429:117–153, 2001.

[126] Lucie Ducloué, Laura Casanellas, Simon J Haward, Robert J Poole, Manuel A Alves, Sandra Lerouge, Amy Q Shen, and Anke Lindner. Secondary flows of viscoelastic fluids in serpentine microchannels. *Microfluidics and Nanofluidics*, 23(3):33, 2019.

[127] Li Xi. Turbulent drag reduction by polymer additives: Fundamentals and recent advances. *Physics of Fluids*, 31(12):121302, 2019.

[128] Allysson F Domingues, Robert J Poole, and David JC Dennis. Inertial instabilities in a microfluidic mixing-separating device. *Physics of Fluids*, 31(7):074101, 2019.

[129] V. Kantsler, E. Segre, and V. Steinberg. Critical dynamics of vesicle stretching transition in elongational flow. *Phys. Rev. Lett.*, 101:048101, 2008.

[130] D. R. Gossett, H. T. K. Tse, S. A. Lee, Y. Ying, A. G. Lindgren, O. O. Yang, J. Rao, A. T. Clark, and D. Di Carlo. Hydrodynamic stretching of single cells for large population mechanical phenotyping. *P. Natl. Acad. Sci. USA*, 109:7630–7635, 2012.

[131] W. Xu and S. J. Muller. Polymer-monovalent salt-induced DNA compaction studied via single-molecule microfluidic trapping. *Lab Chip*, 12:647–651, 2012.

[132] S. J. Haward, M. S. N. Oliveira, M. A. Alves, and G. H. McKinley. Optimized cross-slot geometry for microfluidic extensional rheometry. *Phys. Rev. Lett.*, 109:128301, 2012.

[133] M. Tanyeri and C. M. Schroeder. Manipulation and confinement of single particles using fluid flow. *Nano Lett.*, 13:2357–2364, 2013.

[134] C. de Loubens, J. Deschamps, G. Boedec, and M. Leonetti. Stretching of capsules in an elongational flow, a route to a constitutive law. *J. Fluid Mech.*, 767:R3–1 – R3–11, 2015.

[135] Gipsy Tabilo-Munizaga and Gustavo V Barbosa-Cánovas. Rheology for the food industry. *Journal of food engineering*, 67(1-2):147–156, 2005.

[136] Patrícia C Sousa, Fernando T Pinho, Manuel A Alves, and Mónica SN Oliveira. A review of hemorheology: Measuring techniques and recent advances. *Korea-Australia Rheology Journal*, 28(1):1–22, 2016.

[137] S. J. Haward, J. A. Odell, M. Berry, and T. Hall. Extensional rheology of human saliva. *Rheol. Acta.*, 50:869–879, 2011.

[138] MS Quraishi, NS Jones, and J Mason. The rheology of nasal mucus: a review. *Clinical Otolaryngology & Allied Sciences*, 23(5):403–413, 1998.

[139] Morton M Denn. *Process fluid mechanics*, volume 9. Prentice-Hall Englewood Cliffs, NJ:, 1980.

[140] R. G. Larson, E. S. G. Shaqfeh, and S. J. Muller. A purely elastic instability in Taylor-Couette flow. *J. Fluid Mech.*, 218:573–600, 1990.

[141] P. Pakdel and G. H. McKinley. Elastic instability and curved streamlines. *Phys. Rev. Lett.*, 77:2459–2462, 1996.

[142] G. H. McKinley, P. Pakdel, and A. Öztekin. Rheological and geometric scaling of purely elastic flow instabilities. *J. Non-Newtonian Fluid Mech.*, 67:19–47, 1996.

[143] O. J. Harris and J. M. Rallison. Instabilities of a stagnation point flow of a dilute polymer solution. *J. Non-Newtonian Fluid Mech.*, 55:59–90, 1994.

[144] P. E. Arratia, C. C. Thomas, J. Diorio, and J. P. Gollub. Elastic instabilities of polymer solutions in cross-channel flow. *Phys. Rev. Lett.*, 96:144502, 2006.

[145] R. J. Poole, M. A. Alves, and P. J. Oliveira. Purely elastic flow asymmetries. *Phys. Rev. Lett.*, 99:164503, 2007.

[146] L. Xi and M. D. Graham. A mechanism for oscillatory instability in viscoelastic cross-slot flow. *J. Fluid Mech.*, 622:145–165, 2009.

[147] S. J. Haward and G. H. McKinley. Stagnation point flow of wormlike micellar solutions in a microfluidic cross-slot device: Effects of surfactant concentration and ionic environment. *Phys. Rev. E*, 85:031502–14, 2012.

[148] F. A. Cruz, R. J. Poole, A. M. Afonso, F. T. Pinho, P. J. Oliveira, and M. A. Alves. A new viscoelastic benchmark flow: Stationary bifurcation in a cross-slot. *J. Non-Newtonian Fluid Mech.*, 214:57–68, 2014.

[149] A. Groisman and V. Steinberg. Efficient mixing at low Reynolds number using polymer additives. *Nature*, 410:905–908, 2001.

[150] A. N. Morozov and W. van Saarloos. An introductory essay on subcritical instabilities and the transition to turbulence in visco-elastic parallel shear flows. *Phys. Rep.*, 447:112–143, 2007.

[151] L. Pan and P. E. Arratia. A high-shear, low Reynolds number microfluidic rheometer. *Microfluid. Nanofluid.*, 14:885–894, 2013.

[152] B. Qin and P. E. Arratia. Characterizing elastic turbulence in channel flows at low Reynolds number. *Phys. Rev. Fluids*, 2:083302, 2017.

[153] P. S. Virk, H. S. Mickley, and K. A. Smith. Ultimate asymptote and mean flow structure in Toms phenomenon. *J. Appl. Mech.*, 37:488–493, 1970.

[154] C. M. White and M. G. Mungal. Mechanics and prediction of turbulent drag reduction with polymer additives. *Annu. Rev. Fluid Mech.*, 40:235–256, 2008.

[155] D. Samanta, Y. Dubief, M. Holzner, C. Scäfer, A. N. Morozov, C. Wagner, and B. Hof. Elasto-inertial turbulence. *Proc. Natl. Acad. Sci. USA*, 110:10557–10562, 2013.

[156] Y. Dubief, V. E. Terrapon, and J. Soria. On the mechanism of elasto-inertial turbulence. *Phys. Fluids*, 25:110817, 2013.

[157] Michael D. Graham. Drag reduction and the dynamics of turbulence in simple and complex fluids. *Phys. Fluids*, 26(10):101301, 2014.

[158] D. F. James and J. H. Saringer. Extensional fow of dilute polymer solutions. *J. Fluid Mech.*, 97:655–671, 1980.

[159] M-N. Wei, B. Li, R. L. A. David, S. C. Jones, V. Sarohia, J. A. Schmitigal, and J. A. Kornfield. Megasupramolecules for safer, cleaner fuel by end association of long telechelic polymers. *Science*, 350:72–75, 2015.

[160] B. Keshavarz, E. C. Houze, J. R. Moore, M. R. Koerner, and G. H. McKinley. Ligament mediated fragmentation of viscoelastic liquids. *Phys. Rev. Lett.*, 117:154502, 2016.

[161] V. N. Kalashnikov and M. G. Tsiklauri. Effect of polymer additives on ordered three-dimensional structures arising in cross-slot flow. *J. Non-Newtonian Fluid Mech.*, 48:215, 1993.

[162] S. J. Haward and J. A. Odell. Molecular orientation in non-newtonian flow of dilute polymer solutions around spheres. *Rheol. Acta*, 43(4):350–363, 2004.

[163] F. J. Galindo-Rosales, L. Campo-Deaño, F. T. Pinho, E. van Bokhorst, P. J. Hamersma, M. S. N. Oliveira, and M. A. Alves. Microfluidic systems for the analysis of viscoelastic fluid flow phenomena in porous media. *Microfluid. Nanofluid.*, 12:485–498, 2012.

[164] Y. Zhao, A. Q. Shen, and S. J. Haward. Flow of wormlike micellar solutions around confined microfluidic cylinders. *Soft Matter*, 12:8666, 2016.

[165] A. Varshney and V. Steinberg. Elastic wake instabilities in a creeping flow between two obstacles. *Phys. Rev. Fluids*, 2(7):05130, 2017.

[166] J. Eggers. Nonlinear dynamics and breakup of free-surface flows. *Rev. Mod. Phys.*, 69:865–930, 1997.

[167] S. L. Anna and G. H. McKinley. Elasto-capillary thinning and breakup of model elastic liquids. *J. Rheol.*, 45(1):115–138, 2001.

[168] L. B. Smolka and A. Belmonte. Drop pinch-off and filament dynamics of wormlike micellar fluids. *J. Non-Newtonian Fluid Mech.*, 115:1–25, 2003.

[169] F. Ingremeau and H. Kellay. Stretching polymers in droplet-pinch-off experiments. *Phys. Rev. X*, 3:041002, 2013.

[170] Jens Gottmann, Martin Hermans, and Jürgen Ortmann. Digital photonic production of micro structures in glass by in-volume selective laser-induced etching using a high speed micro scanner. *Physics Procedia*, 39:534–541, 2012.

[171] Brandon L Thompson, Yiwen Ouyang, Gabriela RM Duarte, Emanuel Carrilho, Shannon T Krauss, and James P Landers. Inexpensive, rapid prototyping of microfluidic devices using overhead transparencies and a laser print, cut and laminate fabrication method. *Nature protocols*, 10(6):875, 2015.

[172] Simon J Haward, Vivek Sharma, and Jeffrey A Odell. Extensional opto-rheometry with biofluids and ultra-dilute polymer solutions. *Soft Matter*, 7(21):9908–9921, 2011.

[173] David J Guckenberger, Theodorus E de Groot, Alwin MD Wan, David J Beebe, and Edmond WK Young. Micromilling: a method for ultra-rapid prototyping of plastic microfluidic devices. *Lab on a Chip*, 15(11):2364–2378, 2015.

[174] Ciprian Iliescu, Hayden Taylor, Marioara Avram, Jianmin Miao, and Sami Franssila. A practical guide for the fabrication of microfluidic devices using glass and silicon. *Biomicrofluidics*, 6(1):016505, 2012.

[175] G. Meineke, M. Hermans, J. Klos, A. Lenenbach, and R. Noll. A microfluidic opto-caloric switch for sorting of particles by using 3D-hydrodynamic focusing based on SLE fabrication capabilities. *Lab Chip*, 16(5):820–828, 2016.

[176] C. D. Meinhart, S. T.. Wereley, and M. H. B. Gray. Volume illumination for two-dimensional particle image velocimetry. *Meas. Sci. Technol.*, 11:809–814, 2000.

[177] S. T. Wereley and C. D. Meinhart. Recent advances in micro-particle image velocimetry. *Annu. Rev. Fluid Mech.*, 42:557–576, 2010.

[178] S. T. Wereley and C. D. Meinhart. Micron-resolution particle image velocimetry. In K. S. Breuer, editor, *Microscale Diagnostic Techniques*, pages 51–112. Springer-Verlag, Heidelberg, 2005.

[179] P. Dontula, C. W. Macosko, and L.E. Scriven. Model elastic liquids with water-soluble polymers. *AIChE J.*, 44(6):1247–1255, 1998.

[180] R. B. Bird, R. C. Armstrong, and O. Hassager. *Dynamics of Polymeric Liquids*. John Wiley and Sons, New York, 1987.

[181] V. M. Entov and E. J. Hinch. Effect of a spectrum of relaxation times on the capillary thinning of a filament of elastic liquid. *J. Non-Newtonian Fluid Mech.*, 72:31–54, 1997.

[182] L. E. Rodd, T. P. Scott, J. J. Cooper-White, and G. H. McKinley. Capillary break-up rheometry of low-viscosity elastic fluids. *Appl. Rheol.*, 15:12–27, 2005.

[183] L. Campo-Deaño and C. Clasen. The slow retraction method (SRM) for the determination of ultra-short relaxation times in capillary breakup extensional rheometry experiments. *J. Non-Newtonian Fluid Mech.*, 165:1688–1699, 2010.

[184] L. E. Rodd, J. J. Cooper-White, D. V. Boger, and G. H. McKinley. Role of the elasticity number in the entry flow of dilute polymer solutions in micro-fabricated contraction geometries. *J. Non-Newtonian Fluid Mech*, 143:170–191, 2007.

[185] J. Brandrup, E. H. Immergut, E. A. Grulke, A. Abe, and D. R. Bloch. *Polymer Handbook*, volume 7. Wiley New York etc, 1989.

[186] W. W. Graessley. Polymer chain dimensions and the dependence of viscoelastic properties on concentration, molecular weight and solvent power. *Polymer*, 21:258–262, 1980.

[187] K. Devanand and J. C. Selser. Asymptotic behavior and long-range interactions in aqueous solutions of poly(ethylene oxide). *Macromolecules*, 24(22):5943–5947, 1991.

[188] H. Tadokoro. *Structure of Crystalline Polymers*. Krieger, Malabar, FL, 1990.

[189] Etienne Guyon, Jean-Pierre Hulin, Luc Petit, and Catalin D Mitescu. *Physical hydrodynamics*. Oxford University Press, 2015.

[190] Robert B Griffiths. Thermodynamics near the two-fluid critical mixing point in he 3-he 4. *Physical Review Letters*, 24(13):715, 1970.

[191] Lev Davidovich Landau. Reprinted in collected papers of l. d. landau edited by d. ter haar. *Phys. Z. Sowjetunion (Gordonand Breach, New York, 1965)*, 11, 26:19–32, 1937. reprinted in Collected Papers of L. D. Landau, edited by D. ter Haar (Gordonand Breach, New York, 1965), p. 193.

[192] Jan Thoen, H Marynissen, and W Van Dael. Nematic-smectic-a tricritical point in alkylcyanobiphenyl liquid crystals. *Physical Review Letters*, 52(3):204, 1984.

[193] YP Feng and MHW Chan. Tricritical-and critical-point melting transitions of commensurate CO on graphite. *Physical Review Letters*, 64(18):2148, 1990.

[194] A. Aitta. Iron melting curve with a tricritical point. *J. Stat. Mech.: Theory Exp.*, 2006(12):P12015, 2006.

[195] A. Aitta. Tricritical points and liquid-solid critical lines. In *European Women in Mathematics: Proceedings of the 13th General Meeting. World Scientific*, pages 93–102, 2010.

[196] A. Aitta. Dynamics near a tricritical point in Couette-Taylor flow. *Physical Review Letters*, 62(18):2116–2119, 1989.

[197] Sakuhei Fujiwhara. The natural tendency towards symmetry of motion and its application as a principle in meteorology. *Quarterly Journal of the Royal Meteorological Society*, 47(200):287–292, 1921.

[198] Tobias Günther and Holger Theisel. The state of the art in vortex extraction. In *Computer Graphics Forum*, volume 37, pages 149–173. Wiley Online Library, 2018.

[199] Shaojie Tang and Nadine Aubry. On the symmetry breaking instability leading to vortex shedding. *Physics of Fluids*, 9(9):2550–2561, 1997.

[200] Patrice Meunier and Thomas Leweke. Three-dimensional instability during vortex merging. *Physics of Fluids*, 13(10):2747–2750, 2001.

[201] Patrice Meunier, Uwe Ehrenstein, Thomas Leweke, and Maurice Rossi. A merging criterion for two-dimensional co-rotating vortices. *Physics of Fluids*, 14(8):2757–2766, 2002.

[202] Laura K Brandt and Keiko K Nomura. The physics of vortex merger: further insight. *Physics of Fluids*, 18(5):051701, 2006.

[203] Rohith V Swaminathan, S Ravichandran, Prasad Perlekar, and Rama Govindarajan. Dynamics of circular arrangements of vorticity in two dimensions. *Physical Review E*, 94(1):013105, 2016.

[204] JP Gollub and Michael H Freilich. Optical heterodyne test of perturbation expansions for the Taylor instability. *The Physics of Fluids*, 19(5):618–626, 1976.

[205] Stéphane Le Dizes and Alberto Verga. Viscous interactions of two co-rotating vortices before merging. *Journal of Fluid Mechanics*, 467:389–410, 2002.

[206] O Agullo and AD Verga. Exact two vortices solution of navier-stokes equations. *Physical review letters*, 78(12):2361, 1997.

[207] TH Havelock. Lii. the stability of motion of rectilinear vortices in ring formation. *The London, Edinburgh, and Dublin Philosophical Magazine and Journal of Science*, 11(70):617–633, 1931.

[208] TB Mitchell, CF Driscoll, and KS Fine. Experiments on stability of equilibria of two vortices in a cylindrical trap. *Physical review letters*, 71(9):1371, 1993.

[209] TB Mitchell and CF Driscoll. Electron vortex orbits and merger. *Physics of Fluids*, 8(7):1828–1841, 1996.

[210] Yong Bai and Qiang Bai. *Subsea pipelines and risers*. Elsevier, 2005.

[211] Peter Bearman and Maša Branković. Experimental studies of passive control of vortex-induced vibration. *European Journal of Mechanics-B/Fluids*, 23(1):9–15, 2004.

[212] Donald Wayne Allen and Dean Leroy Henning. Ultrashort fairings for suppressing vortex-induced-vibration, May 1 2001. US Patent 6,223,672.

[213] Tongming Zhou, SF Mohd Razali, Z Hao, and Liang Cheng. On the study of vortex-induced vibration of a cylinder with helical strakes. *Journal of Fluids and Structures*, 27(7):903–917, 2011.

[214] Mengfan Gu, Baowei Song, Baoshou Zhang, Zhaoyong Mao, and Wenlong Tian. The effects of submergence depth on vortex-induced vibration (viv) and energy harvesting of a circular cylinder. *Renewable Energy*, 2019.

[215] R. R. TRIELING, M. BECKERS, and G. J. F. VAN HEIJST. Dynamics of monopolar vortices in a strain flow. *Journal of Fluid Mechanics*, 345:165–201, 1997.

[216] R. C. Kloosterziel and G. J. F. van Heijst. An experimental study of unstable barotropic vortices in a rotating fluid. *Journal of Fluid Mechanics*, 223:1–24, 1991.

[217] L Oruba, PA Davidson, and E Dormy. Eye formation in rotating convection. *Journal of Fluid Mechanics*, 812:890–904, 2017.

[218] Ludivine Oruba, Peter Alan Davidson, and Emmanuel Dormy. Formation of eyes in large-scale cyclonic vortices. *Physical Review Fluids*, 3(1):013502, 2018.

[219] M Beckers, R Verzicco, HJH Clercx, and GJF Van Heijst. Dynamics of pancake-like vortices in a stratified fluid: experiments, model and numerical simulations. *Journal of Fluid Mechanics*, 433:1–27, 2001.

[220] DS Jarman, David Butler, Gavin Tabor, and Robert Andoh. Modelling of vortex flow controls at high drainage flow rates. 2015.

[221] Vincent T Wood and Luther W White. A new parametric model of vortex tangential-wind profiles: Development, testing, and verification. *Journal of the Atmospheric Sciences*, 68(5):990–1006, 2011.

[222] Christoffer Norberg. An experimental investigation of the flow around a circular cylinder: influence of aspect ratio. *Journal of Fluid Mechanics*, 258:287–316, 1994.

[223] Charles HK Williamson. Oblique and parallel modes of vortex shedding in the wake of a circular cylinder at low reynolds numbers. *Journal of Fluid Mechanics*, 206:579–627, 1989.

[224] M. Hoffmann, M. Schlüter, and N. Räbiger. Experimental investigation of liquid-liquid mixing in T-shaped micro-mixers using μ-LIF and μ-PIV. *Chem. Eng. Sci.*, 61:2968–2976, 2006.

[225] R. J. Poole. The Deborah and Weissenberg numbers. *Rheology Bulletin*, 53(2):32–39, 2012.

[226] J. Zilz, C. Schäfer, C. Wagner, R. J. Poole, M. A. Alves, and A. Lindner. Serpentine channels: Micro-rheometers for fluid relaxation times. *Lab Chip*, 14:351–358, 2014.

[227] R. J. Poole, S. J. Haward, and M. A. Alves. Symmetry-breaking bifurcations in T-channel flows: Effects of fluid viscoelasticity. *Proc. Eng.*, 79:28–34, 2014.

[228] A. Soleymani, E. Kolehmainen, and I. Turunen. Numerical and experimental investigations of liquid mixing in T-type micromixers. *Chem. Eng. J.*, 135S:S219–S228, 2008.

[229] J. Soulages and G. H. McKinley. Flow and stability of wormlike micellar and polymeric solutions in converging and T-shaped microchannels. *AIP Conf. Proc.*, 1027:973–975, 2008.

[230] R. J. Poole, M. Alfateh, and A. P. Gauntlett. Bifurcation in a T-channel junction: Effects of aspect ratio and shear-thinning. *Chem. Eng. Sci.*, 104:839–848, 2013.

[231] C. S. Dutcher and S. J. Muller. Effects of weak elasticity on the stability of high Reynolds number co-and counter-rotating Taylor-Couette flows. *J. Rheol.*, 55(6):1271–1295, 2011.

[232] S. J. Haward and G. H. McKinley. Instabilities in stagnation point flows of polymer solutions. *Phys. Fluids*, 25:083104, 2013.

[233] Y. L. Joo and E. S. G. Shaqfeh. The effects of inertia on the viscoelastic Dean and Taylor-Couette flow instabilities with application to coating flows. *Phys. Fluids*, 4:2415–2431, 1992.

[234] F. A. Cruz, R. J. Poole, A. M. Afonso, F. T. Pinho, P. J. Oliveira, and M. A. Alves. Influence of channel aspect ratio on the onset of purely-elastic flow instabilities in three-dimensional planar cross-slots. *J. Non-Newtonian Fluid Mech.*, 227:65–79, 2016.

[235] K. Kim, C-F. Li, R. Sureshkumar, S. Balachandar, and R. J. Adrian. Effects of polymer stresses on eddy structures in drag-reduced turbulent channel flow. *J. Fluid Mech.*, 584:281–299, 2007.

[236] K. Kim and R. Sureshkumar. Spatiotemporal evolution of hairpin eddies, Reynolds stress, and polymer torque in polymer drag-reduced turbulent channel flows. *Phys. Rev. E*, 87:063002, 2013.

[237] J. Page and T. A. Zaki. Streak evolution in viscoelastic Couette flow. *J. Fluid Mech.*, 742:520–551, 2014.

[238] J. Page and T. A. Zaki. The dynamics of spanwise vorticity perturbations in homogeneous viscoelastic shear flow. *J. Fluid Mech.*, 777:327–363, 2015.

[239] S. J. Lee and T. A. Zaki. Simulations of natural transition in viscoelastic channel flow. *J. Fluid Mech.*, 820:232–262, 2017.

[240] Joel H Ferziger and Milovan Perić. *Computational methods for fluid dynamics*, volume 3. Springer, 2002.

[241] M. D. Chilcott and J. M. Rallison. Creeping flow of dilute polymer solutions past cylinders and spheres. *J. Non-Newtonian Fluid Mech*, 29:381–432, 1988.

[242] P. J. Coates, R. C. Armstrong, and R. A. Brown. Calculation of steady state viscoelastic flow through axisymmetric contractions with the EEME formulation. *J. Non Newton. Fluid Mech.*, 42:141–188, 1992.

[243] P. J. Oliveira. Asymmetric flows of viscoelastic fluids in symmetric planar expansion geometries. *J. Non-Newton. Fluid Mech.*, 114:33–63, 2003.

[244] P. J. Oliveira, F. T. Pinho, and G. A. Pinto. Numerical simulation of non-linear elastic flows with a general collocated finite-volume method. *J. Non Newton. Fluid Mech.*, 79:1–43, 1998.

[245] P. J. Oliveira. Method for time-dependent simulations of viscoelastic flows: vortex shedding behind cylinder. *J. Non-Newton. Fluid Mech.*, 101:113–137, 2001.

[246] M. A. Alves, P. J. Oliveira, and F. T. Pinho. A convergent and universally bounded interpolation scheme for the treatment of advection. *Int. J. Numer. Meth. Fluids*, 41:47–75, 2003.